Prototyping of Silicon Strip Detectors for the Inner Tracker of the ALICE Experiment

Prototyping of Silicon Strip Detectors for the Inner Tracker of the ALICE Experiment

Studie aan Silicium Strip Detectoren voor de binnenste reconstructie detector van het ALICE experiment

(met een samenvatting in het Nederlands)

Proefschrift

ter verkrijging van de graad van doctor aan de Universiteit Utrecht op gezag van de Rector Magnificus, Prof. Dr. W. H. Gispen, in gevolge het besluit van het College voor Promoties in het openbaar te verdedigen op maandag 24 april 2006 des ochtends te 10.30 uur

door

Oleksiy Sokolov

geboren op 2 november 1979 te Kiev

Promotor: **Prof. Dr. R.Kamermans**

Co-promotor: **Dr.ir. G.J.L.Nooren**

Contents

Chapter 1

Introduction

1.1 Nuclear matter under extreme conditions

Heavy ion physics is focused on study of the properties of different phases of nuclear matter. Under normal conditions, nuclear matter exist in the form of quarks and gluons confined within protons and neutrons. Quantum Chromo Dynamics (QCD), the theory that describes the strong interaction between elementary particles, predicts a phase transition at high densities and temperatures to a new state called Quark-Gluon Plasma (QGP). In this state quarks and gluons are no longer confined within hadrons but can move freely in a much larger volume. In addition, *chiral symmetry* - the fundamental symmetry of QCD which is spontaneously broken at normal nuclear density, is restored in this state and quark masses are reduced from their large effective values in hadronic matter to their small bare ones. According to Big Bang cosmology such a phase transition from quarks and gluons to hadronic matter took place 10^{-5} s after the Big Bang. QCD lattice calculations predict that this transition takes place at a critical temperature approximately equal to $T_c \approx 175$ MeV, corresponding to an energy density of $\varepsilon_c \approx 0.7$ Gev/fm^3, Fig.1.1. Such energy density can be produced in the laboratory by colliding atomic nuclei at very high energies in particle accelerators. The Large Hadron Collider (LHC) which is currently under construction at CERN, will provide heavy ion beams with unprecedented energies, allowing to achieve the energy density far beyond the critical value ε_c. This high energy density will be contained in mainly gluonic matter with unorthodox properties, for instance, with respect to the energy loss of quarks moving through this hot and dense medium. Presently, little is known about the thermodynamical properties of nuclear matter under such extreme conditions and heavy ion collisions at LHC will provide a possibility to explore this energy density regime experimentally.

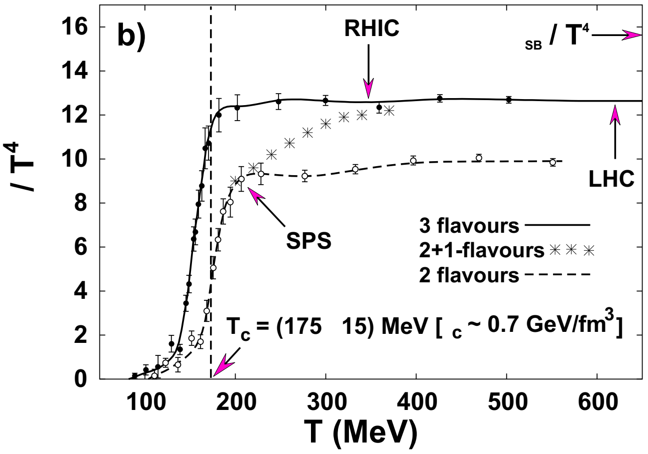

Figure 1.1: The energy-density ε scaled by T^4 calculated from lattice QCD with 2 and 3 degenerate quark flavours (dashed line and solid line) as well as with two light and one heavy (strange) quark (stars). The critical temperature T_c marks the region where ε/T^4 undergoes a rapid rise due to a phase transition. The critical temperature T_c and the temperatures reached at SPS, RHIC and LHC accelerators are marked with corresponding labels. The horizontal arrow on the right-side ordinate shows the value of the Stefan-Boltzmann limit for an ideal quark-gluon gas [1].

1.2 ALICE experiment

ALICE (A Large Ion Collider Experiment) [2] is an experiment at LHC designed for the study of heavy ion collisions, at a center-of-mass energy ~5.5 TeV per nucleon. The prime goal of the experiment is the detailed study of the behavior of nuclear matter in the QGP state.

In general, the ALICE detector is designed with an emphasis to identify midrapidity hadrons, leptons and photons produced in the interaction, in the broad range from very low (~ 100 MeV/c) to fairly high (~ 100 GeV/c) transverse momentum p_t, to reconstruct weakly decaying particles such as hyperons, B and D mesons, and to perform these tasks in a high-multiplicity environment, up to 8000 particles per unit of rapidity at midrapidity. The layout of the experimental setup with the various subdetectors is shown in Fig.1.2.

The L3 magnet provides a moderate magnetic field of 0.5 T in a large volume, the field is parallel to the beam axis z. In this volume several detectors that cover the rapidity range $|\eta| < 0.9$ and full azimuth are located: the Inner Tracking System (ITS) located around the interaction region, the cylindrical TPC (Time Projection Chamber) surrounding the ITS, the TDR (Transition Radiation Detector) and TOF (Time Of Flight) detector surrounding the TPC. These detectors provide particle tracking and identification in the specified rapidity region. In addition there is an array of ring-imaging Čerenkov detectors for the iden-

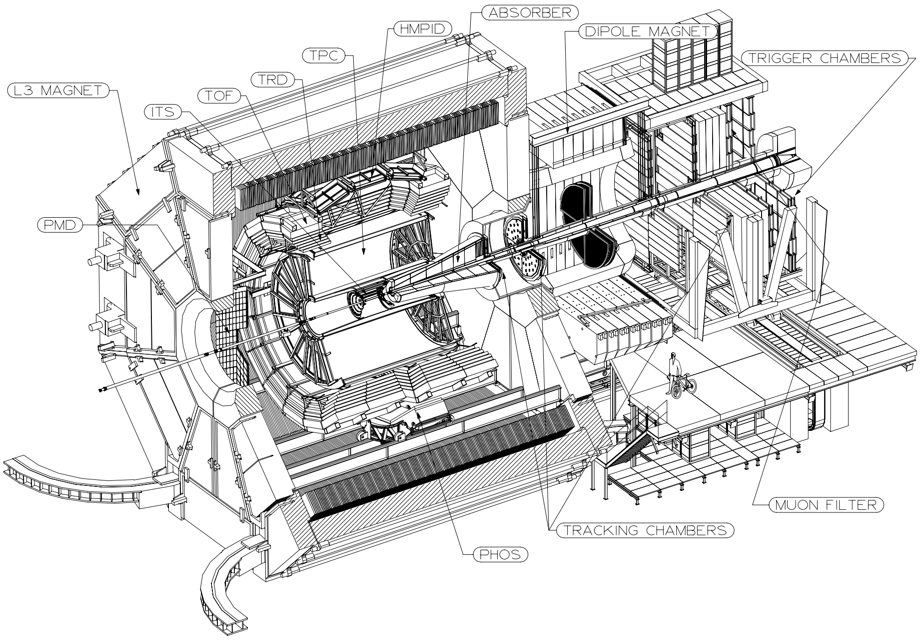

Figure 1.2: ALICE detector.

tification of high-momentum particles (High Momentum Particle Identification Detector — HMPID) covering the rapidity range $|\eta| < 0.6$ and 57.6° in azimuth, and an electromagnetic calorimeter ($|\eta| < 0.12$, 100° azimuthal coverage) consisting of arrays of high-density crystals (Photon Spectrometer — PHOS). The large rapidity systems include the muon spectrometer ($-4.0 \leq \eta \leq -2.4$) for the detection of muon pairs from heavy quarkonium decay, a photon counting detector (Photon Multiplicity Detector — PMD) for the detection of photons in the rapidity range $2.3 \leq \eta \leq 3.5$ and the Forward Multiplicity Detector (FMD) covering the large rapidity region up to $\eta = 5.1$. Two sets of neutron and hadron calorimeters, located at 0° and about 90 m away from the interaction vertex (Zero Degree Calorimeters — ZDC), will measure spectator nucleons at beam rapidity.

1.3 Inner Tracking System (ITS)

The Inner Tracking System (ITS) is designed to perform particle tracking and identification at radii smaller than the inner radius of the TPC. The tasks of the ITS are:

- to localize the primary vertex with a precision better than 100 μm;
- to reconstruct the secondary vertices from decays of hyperons and D and

B mesons which is essential for the measurement of heavy quark energy losses in QGP medium;

- to track and identify charged particles with momentum below 100 MeV/c (these particles are detected only with the ITS). This extends the momentum range for measurement of particle spectra towards low-p_t which is important for the study of the collective effects and the suppression of soft γ conversions as well as the Dalitz background in electron-pair spectra;

- to improve the momentum and angle resolution for the high-p_t particles which also traverse the TPC, this is beneficial practically for all physics topics addressed by ALICE;

- to reconstruct, albeit with a limited momentum resolution, particles traversing dead regions of the TPC.

The ITS consists of six cylindrical layers of coordinate-sensitive silicon detectors, covering the rapidity region $|\eta| < 0.9$ for vertices located within the length of the interaction diamond ($\pm 1\sigma$), i.e. 10.6 cm along the beam axis z. All the layers, except for the inner two, provide analogue information for dE/dx measurements for particle identification in the non-relativistic ($1/\beta^2$) region. This gives the ITS a stand-alone capability as a low-p_t particle spectrometer.

The two innermost layers having a radius 4 cm and 7 cm are made of Silicon Pixel Detectors. The rapidity coverage of these detectors is extended to $|\eta| < 1.98$. The pixel detectors have been chosen because of their high granularity and excellent precision and two-track resolution necessary in this region with the highest track density (about 80 particles per cm^2) . These detectors have truly two-dimensional readout and provide a spatial resolution of 12 μm in $r\phi$ coordinate (bending plane) and 100 μm in z coordinate (along the beam axis), which is crucial for the determination of the primary vertex position and secondary vertices originating from the weak decays of strange, charm and beauty particles.

The next two layers are located at 15 cm and 24 cm from the interaction region and are made of Silicon Drift Detectors. The drift detectors will also operate in a high track density environment (about 7 particles per cm^2) and the two-dimensional readout will provide a good point resolution (35 μm in $r\phi$ and 25 μm in z direction) together with good two-track resolution.

The outer two layers are essential for matching the tracks detected by the ITS to the tracks found by the TPC. At larger radii the granularity requirement are less stringent due to a lower track density (at most 1 particle per cm^2), and the use of Silicon Strip Detectors (SSD) becomes possible. The outer layers consist of double-sided SSD located at radii 39 cm and 44 cm. SSD is a cheaper and well-proven technique, which is essential in view of the large number of detectors needed (1698 detector modules covering a total area of about 5 m^2). Double-sided technology allows a 2-D coordinate measurements and gives a possibility to match signal pulse height from both sides in order to help to resolve ambiguities. The specifications require the detectors to have a spatial resolution better than 20 μm in the $r\phi$ direction and 830 μm in the z direction.

1.4 Layers 5 and 6 – the Silicon Strip Detectors

1.4.1 Principle of operation

A relativistic charged particle traversing a silicon wafer creates a number of electron-hole pairs which is proportional to the energy loss in the wafer. In the double-sided silicon strip detector the electrons and holes are swept by the electric field to the opposite sides of the wafer. On both sides there are implanted strips with high doping concentration (see Fig.1.3), p-type on one side (marked as p^+) and n-type (marked as n^+) on the other side. The strips are individually coupled to the analogue readout electronics. According to the Ramo theorem, if a single electron-hole pair is created anywhere in the detector and the electron arrives by any path at one of the n^+ strips and the hole arrives at one of the p^+ strips, then the induced charges are $-e$ at the former strip and $+e$ at the later strip and 0 anywhere else [3]. A typical charge deposition by a minimum ionizing particle in 300 μm thick wafer at normal incidence is about 25000 electron-hole pairs. The deposited charge is collected by one or more strips per side, this gives the device the position sensitivity. If the strips one side are not parallel to the strips on the other side, then the 2-D coordinate of the particle impact point can be reconstructed by combining the position information from both sides.

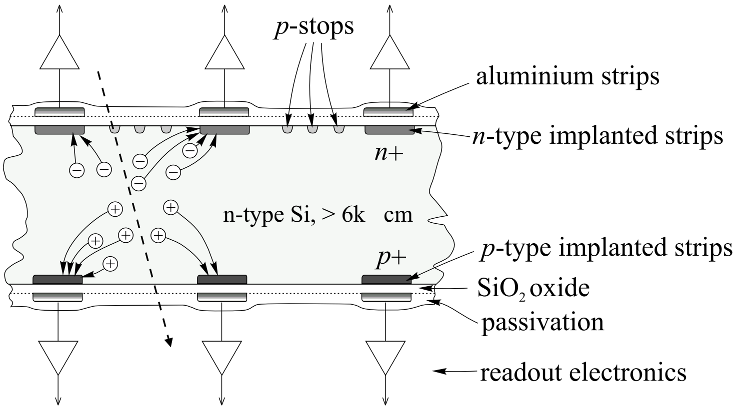

Figure 1.3: Cross-section of the SSD sensor.

1.4.2 SSD Sensor

The ALICE SSD are made using double-sided silicon sensors with AC-coupled readout strips. The bulk of the sensor is n-type silicon with p^+ type

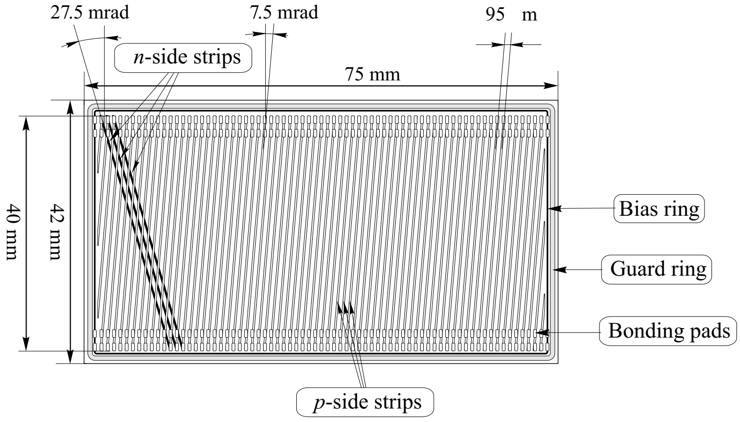

Figure 1.4: A schematic view of the SSD sensor from the *p*-side, the sensor is drawn not to scale. The number of strips is arbitrary. Three *n*-side strips are shown in transparency.

implanted strips on one side (called *p*-side) and n^+ type implants on the other side (*n*-side), the n^+ implants are insulated by p^+ doped regions called "p-stops" (see Fig.1.3).

Integrated capacitors are formed by the implanted strips and the aluminium strips deposited on top of them and are interleaved with a thin SiO_2 layer. The integrated capacitors enable AC coupling to the front end electronics, providing a separation of the leakage current in the strips from the inputs of readout electronics.

The sensors have a rectangular shape with a size 75 × 42 mm^2 and are 300 μm thick. On the *p*-side the strips are tilted by an angle of 7.5 mrad with respect to the short edge of the sensor and on the *n*-side by an angle of 27.5 mrad creating thus a stereo angle of 35 mrad with the strips of the opposite side, see Fig.1.4. The strip pitch is 95 μm on both sides (measured parallel to the long edge of the sensor), the number of strips terminating against each longer sensor edge is 768. The strips have a length of 40 mm (measured along the shorter sensor edge), this provides an occupancy up to 4% for a particle density of 1 cm^{-2}. Because of the strip tilt angle, a few strips will have a reduced length, terminating against the short edge of the sensor: 3 are close to each short edge on the *p*-side and 11 on the *n*-side. These strips have bonding pads only at one end. Each full-length strip crosses 15 strips of the opposite side. This allows to reconstruct multiple hits from the same sensor at the expense of the poorer spatial resolution in the direction along the sensor shorter edge (which is parallel to the z direction in ALICE frame) while keeping the fine resolution in the $r\phi$ direction (along the longer sensor edge) for better particle momentum determination. Mounting the sensors with *p*- or *n*-side facing the interaction region in layers 5 and 6, respectively, results in four different orientations of the strips with respect to the beam direction. This reduces the fake track probability significantly, resulting in a more robust tracking.

The sensor is biased by a punch-through structure [4]. The bias voltage is supplied to the rectangular bias ring which is located close to the sensor edge, on each sensor side and surrounds all the strips. The guard ring surrounds the bias ring and takes care of the edge-generated leakage current.

The sensors are produced by three different manufacturers, each implementing the sensor in a slightly different way. The differences relevant in this context are the strip widths: 40 μm (ITC[1]), 26 μm (SINTEF[2]) and 45 μm (Canberra[3]).

1.4.3 SSD Module

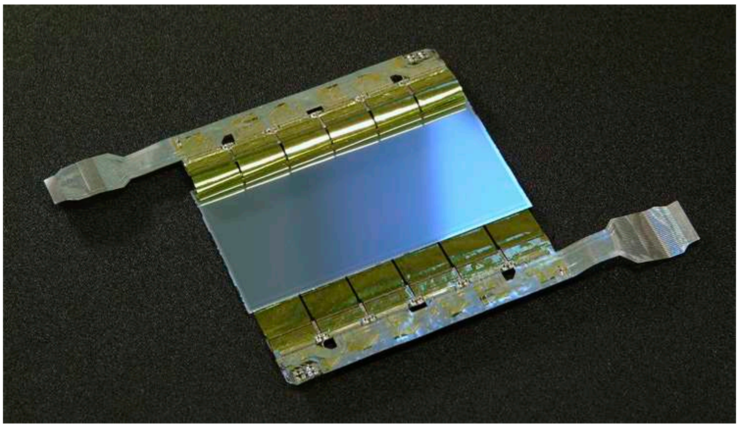

Figure 1.5: The SSD module.

The module assembly is shown in Fig.1.5. Each side of the sensor is connected to a hybrid circuit carrying 6 daisy-chained HAL25[4] read-out chips [5] each. The chips are mounted on a carbon fibre plate (stiffener) which serves as a heat bridge. All the 768 strips terminating against the sensor longer edge on each sensor side are connected to the input of a readout chip. The 128-channel front-end chips amplify and shape the signals from the sensor strips and contain a sample-hold circuit to store the analogue signal after a trigger. The analog samples can be read-out serially at speeds up to 10^7 samples per second. The peaking time of the shaping circuit is adjustable between 1.4 μs and 2.2 μs. All parameters of the front-end chips are controlled via a JTAG interface. Connections on the hybrid and the connections between the front-end chips and the sensor are made using low-mass micro-cables consisting of aluminium conductors on a polyimide carrier [6]. This technology allowed to decouple mechanically the sensor from the readout electronics and reduce multiple scattering by using

---

[1] ITC-irst, Via Sommarive 18, I-38050 Trento, Italy

[2] SINTEF Electronics and Cybernetics, Blindern, N-0314 Oslo, Norway

[3] Canberra Semiconductor NV, Lammerdries 25, B-2250 Olen, Belgium

[4] Designed by LEPSI/IReS, Strasbourg, manufactured by IBM, USA.

lower-Z aluminium instead of traditional copper. Since multiple scattering is one of the limiting factors of momentum determination for slow particles, a lot of attention has been payed to reduction of effective radiation thickness of the SSD layers. This resulted in radiation thickness of 0.82% X_0 per layer (compared to 0.39% X_0 for bare Si sensor only), this is so far the lightest design for double-sided detectors.

The hybrids are connected to the EndCap boards which decouple the analog and control signals from the sensor bias voltage and buffer all signals to and from the front-end chips and generate the control signals for read-out of the analog buffers using two ASICs[7].

1.4.4 The Ladder

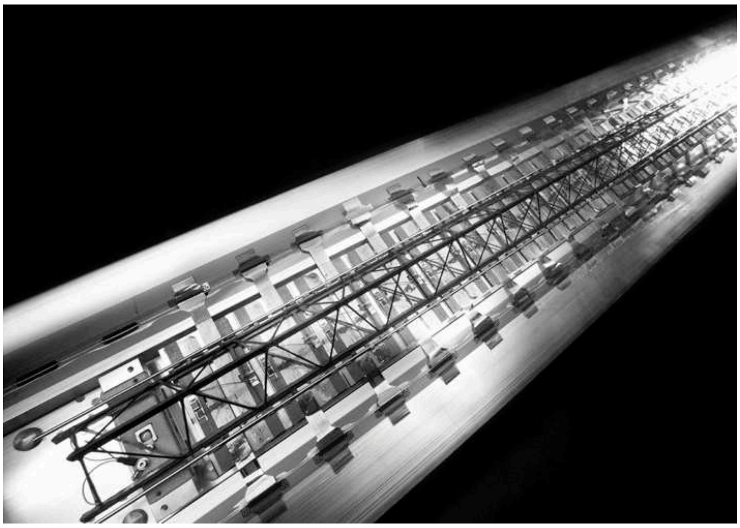

Figure 1.6: The first assembled SSD ladder. Photo by Peter Ginter.

The SSD modules are mounted on carbon fibre support structures called ladders. The ladders run parallel to the beam axis, the shorter edges of the sensors are oriented parallel to the ladder direction, see Fig.1.6. The modules are mounted with a pitch of 39.1 mm to ensure an overlap in the z direction, in order to achieve this overlap even and odd modules are mounted at slightly different distance from the beam axis. For the overlap in the ϕ direction even and odd ladders are also positioned at slightly different distance from the beam axis. This assures full angular coverage for tracks originating from the vertices located within the interaction diamond. Layer 5 contains 34 ladders each carrying 22 modules, and Layer 6 contains 38 ladders with 25 modules each.

Chapter 2

HAL25 Chip Quality Assurance

2.1 Introduction

The ALICE ITS [8] requires 1698 silicon strip detector modules. Each side of the module is read out by a hybrid which consists of 6 HAL25 front end chips. Therefore, a total number of 3396 hybrids and 20376 chips (excluding spares and production losses) are required for the construction of the SSD layers of the ITS. This chapter describes the test system for the mass production acceptance test of the front-end chips and hybrids. Test results of the first significant portion of the chips and hybrids are summarized.

2.2 Front-End Electronics

The HAL25 chip has dimensions of 11 mm×3.8 mm ×150 μm and is based on 0.25 μm CMOS process. The chip is designed with a special radiation-tolerant technique to meet the radiation-hardness and SEU[1]-tolerance demands of ALICE experiment. HAL25 is the first front-end chip with geometric layout optimized for microcable connection. The chip contains 128 analogue channels, each consisting of a charge sensitive preamplifier, a shaper and a capacitor C_{HOLD} to store the voltage proportional to charge collected from the detector strip (see Fig.2.1). A large input dynamic range (0-14 MIPs) of each channel is necessary for the efficient collection of charge induced by particles, including highly-ionizing ones. A current pulse generator, added at the input of every channel, allows to test the analogue chain by injecting a short current pulse with a programmable amplitude in the range of ±15 MIPs.

---

[1] SEU — Single Event Upset, the change of the state of memory cells or transistors caused by ionizing radiation.

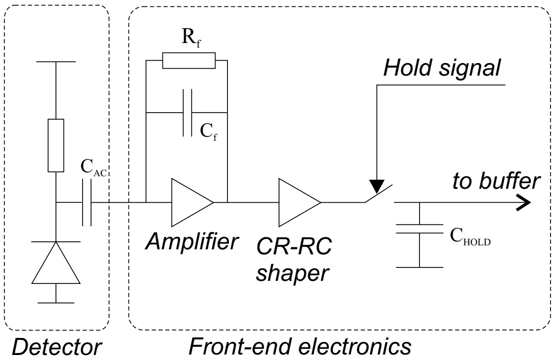

Figure 2.1: Circuit diagram of a single front-end amplifier channel connected to a sensor strip.

The storage of analogue data is triggered by an external logic (Hold signal) which disconnects the C_{HOLD} capacitors from the shaper output. The voltage stored by the capacitors is then serially read out at 10 MHz rate through an analogue multiplexer and differential current output buffer. The shaping time is adjustable from 1.4 μs to 2.2 μs, and should match the time delay between a high-multiplicity heavy-ion collision and an arrival of L_0 trigger pulse that sets the Hold signal.

The chip is programmable via a JTAG [10] controller which allows:

- to choose the chip operation mode between the sequential readout at 10 MHz (normal operation mode), and so-called “Transparent” mode when only one particular channel is permanently connected to the output buffer so that one can see the pulse shape after the shaper. The channel selection is done by programming a special JTAG register;

- to program the bias settings of different analogue stages in the chip in order to tune the pulse shape. Different sets of settings are used for positive and negative signals;

- to select channels for testing them with the internal pulse generator and to set the amplitude of the injected current pulse. The polarity is determined by the polarity of the external driving pulse;

- to perform a boundary scan test in order to check the integrity of bonds of aluminum traces that interconnect chips in a daisy-chain (Token_In, Token_Out lines) and traces that are used to supply chips with main control signals (Readout_Clock, Hold, Pulse, Fast Reset).

- to read the unique 24-bit chip serial number which is burned in before wafer dicing. This number is used to trace the chip history from it’s production till installation in the experiment.

The HAL25 chips are mounted on a carbon stiffener. Connections between silicon sensor strips and chip input pads as well as hybrid interconnections and connection of modules to endcaps are made using low mass flexible aluminum/polyimide TAB microcables [6].

Three types of cables are used: chip cables, flex and ladder cables. Chip cables are bonded directly to the front end chips and connect chips to the sensor and to the flex. Chip cables contain a fanout structure which can be used in combination with a commercially available connector and frame [9]. This makes accessible all chip inputs and outputs and allows a full functionality test of single chips after bonding (called "framed chip" at this stage). After these tests the fanout structure is cut from the cable, leaving the pattern needed to connect chips to the flex and the sensor. There are three types of chip cables used: F(irst), M(iddle) and L(ast). Each hybrid contains one F, four M and one L chip. The main difference between the cables is that the F-cable connects to LVDS (Low Voltage Differential Signalling) input pads of the chip for Token_In signal and to 2.5V pad for Token_Out signal; the M-cable connects only to 2.5V input pads for both Token_In and Token_Out signals; and the L-cable connects to 2.5V pad for Token_In and to LVDS pads for Token_Out signals. This is done in order to optimize power consumption: the Token_In and Token_Out signals can be reliably transmitted over short distances (from one chip to the next one in the daisy-chain) using low-power single-ended 2.5V lines, but over a long distance (from the EndCap to the hybrid through the ladder cable and back) one needs differential and more power-consuming LVDS lines. The chip has input and output for both LVDS and 2.5V lines, and the different types of chip cables just select the appropriate lines.

The flex cable, glued to the carbon plate, is a multi-layer interconnecting bus. It connects chips to SMD-type decoupling capacitors and 100Ω LVDS termination resistors mounted on the stiffener and is used for control signals input and output, power supply, analogue output and detector bias supply. The output tail of the flex has a fanout structure which fits into a ZIF (Zero Insert Force) connector and allows to test the full functionality of the hybrid after assembly. The fanout structure is removed after testing.

The ladder cable is bonded to the output of the flex and connects the whole hybrid to the endcap electronics [7].

The test station described in this chapter is designed for mass production acceptance tests of both the framed chips and complete hybrids. Since the chips in the hybrid are connected serially, the programming and operation of the framed chips is very similar to the hybrids. This allowed to use the same hardware and software for tests of both items, using only different adaptors. For the framed chips, the Yamaichi connector with associated electronics was used and for the hybrids only a simple connection board.

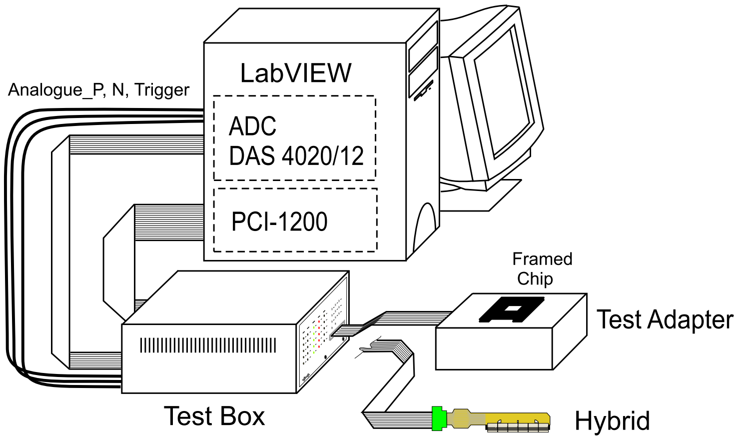

Figure 2.2: Test station.

2.3 Test Station

2.3.1 Overview

A test station consists of a computer, Test Box, a hybrid adapter and a chip adapter (see Fig. 2.2). The chip adapter unit is used to connect framed chips, i.e. chips which have already been bonded to a chip-cable, to the Test Box. The hybrid adapter is used to connect hybrids to the Test Box. Both adapters are connected to the Test Box via a 50-way flat cable. The Test Box contains the electronics to generate all the signals necessary for testing the functionality of both chips and hybrids. It interfaces to the two adapter units and to a PC via an ADC card and a parallel I/O card. The test software on the PC has been implemented in LabVIEW.

2.3.2 Hybrid Adapter

The hybrid adapter is simply a small printed circuit board, which translates from the 50-pin connector to a 24-way ZIF connector to which the hybrid is connected. It also includes a 1 MΩ series protection resistor in the bias circuit in case the unit is used for testing a module with a sensor. It was found to be essential to enclose the hybrid in a metal box connected to the testbox ground, so as to avoid any ground loops and electric pickup from the outside world.

2.3.3 Chip Adapter

The chip adapter is a more complex unit. It interfaces between the 50-pin connector and the Yamaichi test connector in which the framed chips are placed. A chip cable (see Fig.2.3), which is put into a frame, actually consists of two parts. The inner part (the shaded region in Fig.2.3) is the final cable, which is used to connect the chip to hybrid and sensor. On the chip output side, the chip cable connects the chip bonding pads to bonding pads on the hybrid. These connections are for power, digital control and analog output. On the chip input side, 128 traces connect the inputs of the readout channels to the sensor, also by bonding. All these traces are extended on an outer, removable template to a larger-pitch contact pad pattern which can be accessed by the Yamaichi test connector. In this way, all functionality of the bonded chip can be tested. But there are also several other features included in the chip adapter. The first is that it contains electronics to verify the alignment of the frame in the Yamaichi connector by checking four 8-bit test patterns that are designed in the chip cable. These test patterns are located in the four corners of the chip cable layout and consist of eight pads which are either grounded or left open. This pattern of "ones" and "zeroes" is compared with a fixed pattern. A number of LED's give the status of the result.

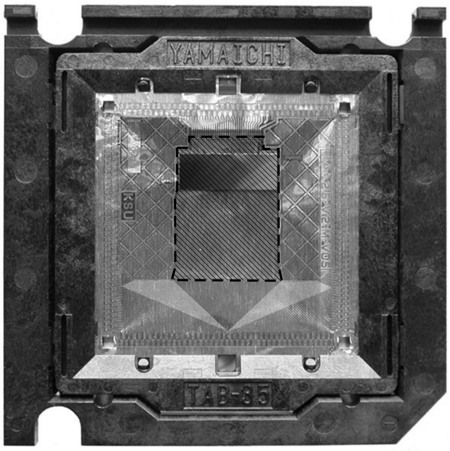

Figure 2.3: A "framed" chip – HAL25 bonded on a microcable. The shaded region marks the final part of the cable, which is left after cutting the auxiliary cable structures.

A second feature is that the type of chip cable is detected by checking the type pattern in the cable. Three LED's on the chip adapter indicate what type of cable is inside at the moment. Three lines in the 50-way cable are reserved to read out the status of the LED's (i.e. the type of the cable) with a PC. If the hybrid adapter is connected instead of the chip adapter, then these three lines are grounded, making another unique pattern. This pattern is different from the case of a loose cable when all three lines are pulled up.

A third feature is that the bias trace in the F and L cables is checked for continuity. This trace is critical in the sense that if it is interrupted, the hybrid may function faultlessly, but the sensor will not be biased and a module will not work. For this reason this trace is included in two cables, so there are two connections in parallel.

The last feature has to do with checking the 128 input traces and their bonding connection to the chip. As described, each channel of the chip has an internal programmable test pulse generator. This generator injects a charge pulse into the input of the charge sensitive amplifier (CSA) of the channel. If the inputs are individually grounded externally, then this charge is shorted to the ground and no charge flows to the input of the CSA. The output signal of this channel is just a pedestal value. But if the connection to the ground is interrupted due to a broken cable trace or a bad bonding, than the injected charge flows to CSA and one observes a clear signal in that particular channel. In this way a clear identification of faulty channels is possible. The individual shorting of inputs is realized by utilizing CMOS open drain inverters, which were selected for very low leakage current (typically 2 pA), so as not to interfere with normal operation of the chip when grounding is disabled. A drawback of this scheme is that some additional capacitance, which depends on the length of the routing traces connecting chip inputs to the drain inverters, is added to the input of every channel, leading to noise increase.

Figure 2.4: Test Box with Chip Adapter.

2.3.4 Test Box

The Test Box (see Fig. 2.4) has been designed so as to give maximum information on the status of all signals coming to and from the chip and also to give access to a number of critical signals via buffered monitor outputs so they can be viewed on an oscilloscope for more detailed analysis if necessary. The Test Box generates all the signals necessary for read out of HAL25 chips and hybrids. After receiving a trigger signal it activates the “Hold” signal which freezes the analog signal in the HAL25 chip and then it generates the complete read out sequence for n chips, where n can be any number from one to six. The trigger signal can come from an external source or it can be generated by the software. The Test Box contains a Field Programmable Gate Array (FPGA), which generates the read out cycle, some discrete logic, digital level converters (the HAL25 operates at both 2,5V and LVDS logic levels) and two analog buffers, one for the ADC card and one for the monitor output on the Test Box front panel.

The Test Box also contains a dedicated low noise 2,5V supply for the HAL25 chips. This supply is identical to the one used in the final SSD endcap design, it has an overcurrent trip circuit to protect chips and hybrids. The front panel contains a large number of LED’s to give direct status information. All status signals are also sent to the computer.

2.3.5 PC-based Data Acquisition System

The communication between the PC and the Test Box control as well as the analogue data acquisition is done by using two commercially available PCI ADC-cards. The first card, ADC DAS 4020/12 by Measurementcomputing [11] has four 12-bit analogue acquisition channels and 24 digital I/O channels. Digital channels are used for JTAG interface and Test Box control, two ADC channels are used for analogue data acquisition at 10 MHz rate. The second card, PCI-1200 by National Instruments, has 24 digital I/O channels which are also used for Test Box control, and 5 slow ADC inputs two of which are used for HAL25 current consumption measurement.

2.3.6 Test Sequences and the Software

The user-friendly graphical interface written in LabVIEW allows to run a series of tests, displays the status of the tests and creates a log-file where test results are stored. All is done just by pressing one button. The tests performed with the chips and hybrids can be divided into two groups: “Chip functionality tests” and “Channel functionality tests”. The test procedure consists of the following steps:

- The operator is requested to type in a chip cable or a hybrid cable number, written on the cable. This number is used to identify the component later in the production database. It was decided to use this number rather than the chip serial number, because the latter can be read out only if the JTAG chain is intact and the chip is functional.
- The type of the cable (F/M/L or hybrid) is detected by reading out 3 LED status lines from the chip or hybrid adapter.

- The number of chips in the JTAG chain is detected. This is done by counting the number of 1-bit “Bypass” registers in the JTAG chain. The detected number should be 1 if a framed chip is being tested or 6 in case of a hybrid. Any other number indicates a JTAG communication problem or another serious defect.

- The test of all the chip JTAG registers is performed by writing and reading back an extensive set of test patterns.The pattern read back should coincide with the loaded one. This allows to detect any stuck-to or bridged bits or any other problem in the JTAG chain.

- The JTAG boundary scan test (ExTest) checks the integrity of bonds of aluminum traces that supply main digital control signals (TkIn, TkOut, RClk, Hold, Pulse, FastReset) to the chips. Each of these lines has a boundary scan cell that normally drives the signal from the chip contact pin to the core logic but can also be preloaded with a desired value or capture the status of the line, so that it can be read back with JTAG. The Boundary Scan Register, made up of these 6 scan cells connected in series is addressed in this test.

- A simple chip functionality test (InTest) counts the number of readout clock cycles needed for Token signal to pass through the chip to appear at Token_Out output line. It should take exactly 127 clock cycles.

- The current consumption in Idle, Normal readout and Transparent modes is measured and compared with window threshold. An excessive current consumption may indicate the presence of latent defects that do not affect the chip functionality at the moment of the test but may do so later during long-term chip operation.

The above mentioned tests make up the chip functionality tests and address the basic chip or hybrid features and therefore failure of any of them will lead to the chip or hybrid rejection. In this case the rest of the tests is skipped in order to save testing time. The current consumption in Idle mode is, however, measured in all the cases.

The tests listed below belong to the second group of tests and address the individual chip channels. These tests affect only the overall chip or hybrid rating.

- The pedestal of each channel is measured by taking the average value over 200 chip readouts, the noise is determined as a square root of the dispersion around the average value (around the pedestal). Channels with pedestals falling outside the threshold window are considered as “bad pedestal” channels, and those where noise exceeds the noise threshold – as “noisy” channels. For the framed chips noise thresholds were individually selected for each channel to account for the noise added by the chip adapter.

- The gain of each channel is measured with the internal pulser. Four different pulse amplitudes (equivalent to approx. 3, 6, 9 and 12 MIPs) are used.

Window thresholds are imposed on the 6-MIP pulse since it is well above the noise but still quite far away from the onset of saturation. In order to save the testing time, 16 channels of the same chip are pulsed simultaneously. Channels with gain outside the window threshold are considered as “bad gain” channels.

- For framed chips, all the channels are scanned with the internal pulser, while all the inputs are connected to the ground inside the chip adapter. This allows to find out the “open” input channels - channels that have either a bonding failure or a cable trace interrupt.
- A chip is rated according to the following scheme:
  - the number of bad channels is calculated. A channel is considered bad if it is either “noisy”, “open”, “bad gain” or “bad pedestal”.
  - a chip rating is given as $Q = 100-$the number of bad channels.
- For a framed chip the pulse shape in the Transparent Mode is measured at four different bias settings: shaping time 1.4 μs and 2.2 μs, positive and negative polarities. The test is performed on the first good channel, the tabulated pulse shapes are stored for possible future reference, no thresholds are applied.
- A log file with all the test results is generated. A separate application is used to parse the file and to upload the test results into the production database.

The full test takes about 30 seconds for a chip and about a minute for a hybrid.

2.4 Results

A total number of 12 Test Boxes, chip and hybrid adapters have been built and distributed among the labs participating in the mass production in Helsinki, Strasbourg and Trieste. About 1000 chips have been bonded and tested and about 80 hybrids have been made by summer 2004. In the summer bonding session (Helsinki June-July 2004, wafer GA0SRWX) the yield of functional chips approached 97%. The most common failures among the non-functional framed chips of this session were JTAG port failures (8 chips), JTAG register read-out errors (4 chips) and bonding failures detected by ExTest (3 chips). Part of the JTAG port failures were attributed to contact problems in the Yamaichi connector due to the stretching of the microcable when it is inserted into the connector. Other 90% were acceptable (number of defected channels ≤ 1 i.e. chip rating $Q \geq 99$) and 7% were rejected because of the higher number of defected channels.

The distribution of the number of defected channels per chip is shown in Fig.2.5. Most of the defected channels had either low gain or high noise. Fig.2.6

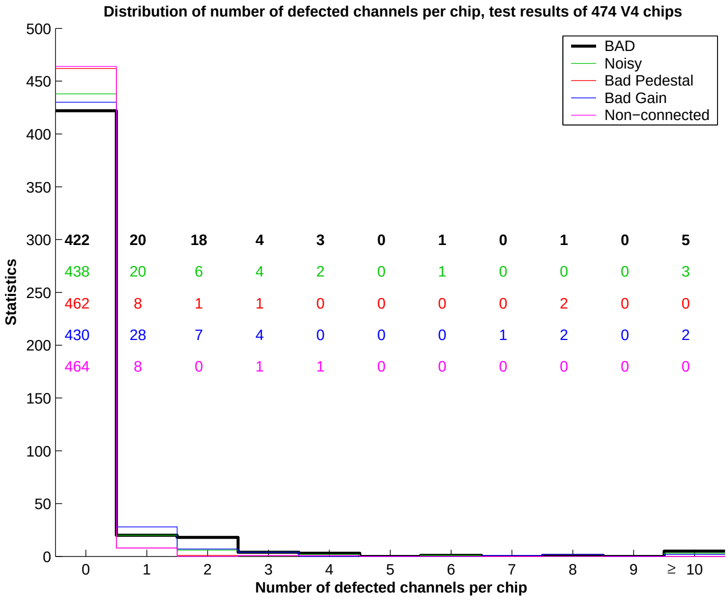

Figure 2.5: Number of defected channels per chip, wafer GA0SRWX.

shows the noise distribution, one can see that the mean noise level varies from channel to channel because of the noise added by the capacitance of the chip adapter. The gain distribution is shown in Fig.2.7.

The distribution of the number of defected channels per hybrid is shown in Fig.2.8. Most of the defects were due to high noise; Fig.2.9 shows noise distribution of the chips assembled on hybrids.

2.5 Conclusion

The test station and the control software has been built and distributed among the labs participating in the mass production of HAL25 front end chips and hybrids. The most important chip and hybrid parameters are checked during the test. For the first statistically significant portion of the chips the yield of the accepted chips approached 90%, other 7% of the chips were functional but had a large number (> 1) of defected channels. Other 3% were not functional and could not be read out. The experience showed that the time used for testing of chips and hybrids is not a limiting factor of the speed of the mass production.

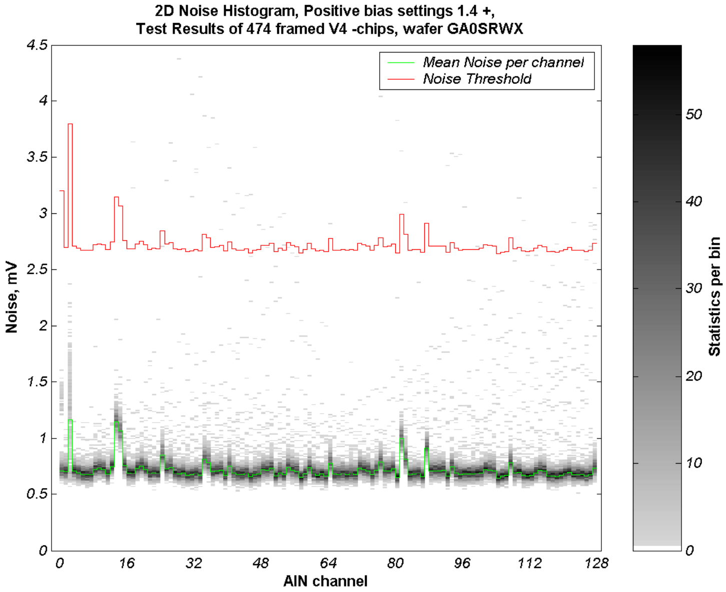

Figure 2.6: Noise distribution of the framed HAL25 v4 chips. Noise of certain channels is higher due to the capacitance added by the chip adapter.

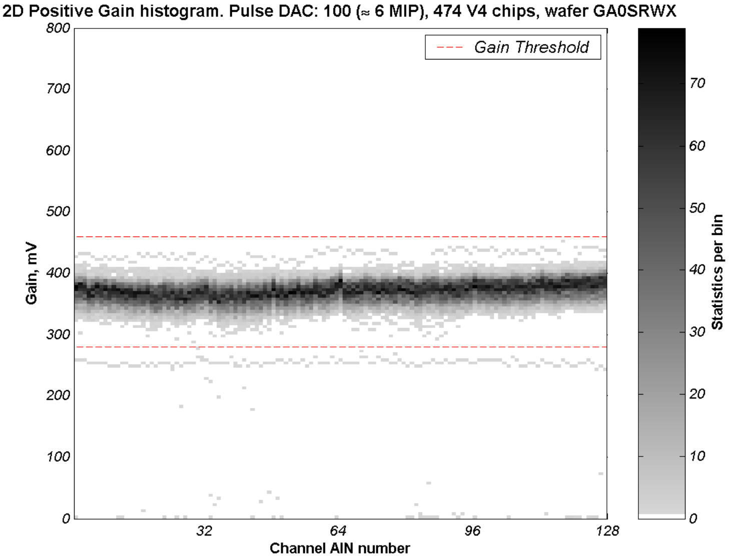

Figure 2.7: Gain distribution of 474 chips measured with internal pulser.

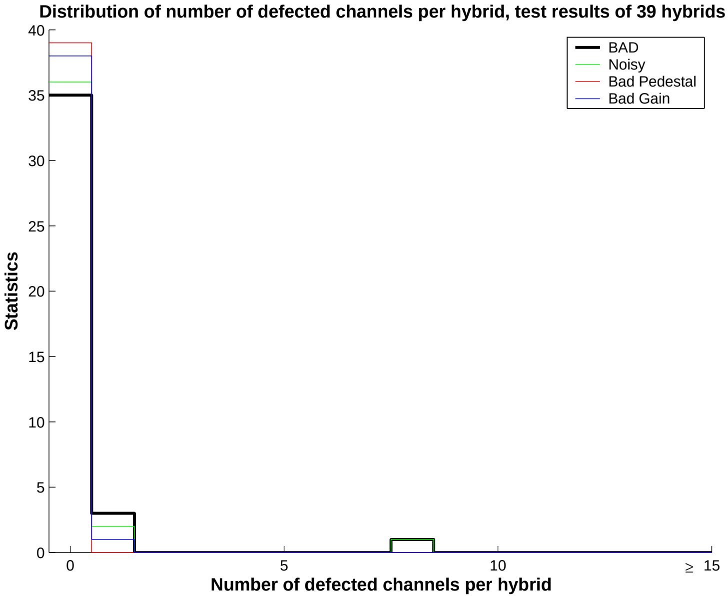

Figure 2.8: Number of defected channels per hybrid.

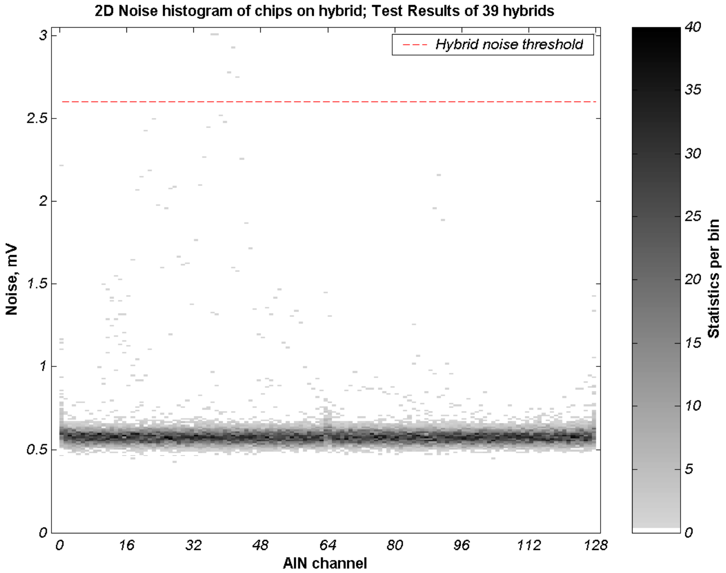

Figure 2.9: Noise of 39 hybrids.

Chapter 3

Characterization of the Silicon Strip Detectors with the Infrared Laser

3.1 Introduction

In the past decade silicon strip detectors have become an indispensable component of the particle trackers of large collider experiments. Traditionally, every experiment requires silicon detectors of its own design matching the specific needs of this experiment. The fundamental properties of the detectors have to be evaluated prior to the detector large scale production and installation in the experiment. Complementary to the particle beam tests, described in the Chapter 4, a table-top test station for measurement of the detector properties would be of a great help. Infrared laser scanners have been found to be a convenient tool for this task [12, 14]. The laser scanning station for performance studies of the ALICE silicon strip detector prototypes has been built at Utrecht University. This chapter describes the principle of the testing method, the test setup and the results of the performed tests.

3.2 The Principle of the Silicon Detector Testing with the Laser Beam

Consider a photon travelling inside a semiconductor material. If the energy E_ν of the photon is larger than the width of the bandgap E_g, the photon is absorbed primarily due to a photoelectric effect. In this process the energy of the photon is transferred to the electron which is lifted from the valence band to the conduction band, producing an electron-hole pair. The intensity of the light penetrating through silicon drops exponentially as $I = I_0 \exp(-\alpha z)$ where

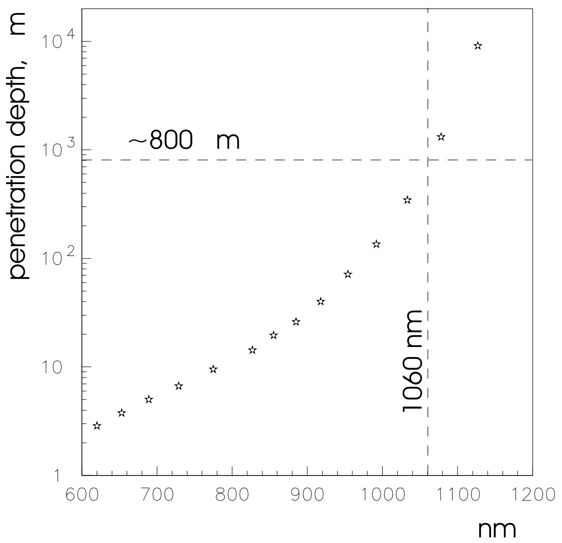

Figure 3.1: Dependence of the light penetration depth a_0 is silicon on the wavelength of a photon. The picture is taken from [14]

α is the photon absorption probability per unit length and z is the depth. For the photon energy close to the bandgap energy, α depends on the energy as:

$$\alpha \sim (E_\nu - E_g)^\gamma \tag{3.1}$$

where γ is a numerical factor that depends on the type of transition and ranges from $\gamma = \frac{1}{2}$ to $\gamma = 2$ [13]. The Fig.3.1 shows the experimental dependence of the penetration depth $a_0 = \alpha^{-1}$ in silicon on the photon wavelength in the photon energy range near E_g. The width of the bandgap for Si is $E_g = 1.12$ eV [17], which corresponds to the photon wavelength of 1130 nm. For the light wavelength of 1060 nm used in the present setup, the penetration depth in Si is about 800 μm. A pulse of the collimated laser light of this wavelength traversing a 300 μm thick silicon sensor, produces a column of electron and hole pairs which are already nearly uniformly distributed along the beam path inside the detector bulk.

A relativistic charged particle traverses the 300 μm thick sensor within 1 ps time and deposits charge in a narrow tube of ≈1 μm radius around the particle trajectory [15]. The charge diffusion time is determined by the carrier mobility and the electric field in the sensor, for 300 μm sensors it is typically $t_e = 25$ ns for electrons and $t_h = 70$ ns for holes for the applied bias voltage of 30 V, see equations (3.52) and (3.51) on page 47. The pulse shaping time constant τ of the front-end electronics is usually chosen to be not smaller than t_h. If the lateral size of the laser beam is much smaller than the detector strip pitch, and the laser pulse duration is much smaller than τ, then the detector response on the laser light will mimic that of a charged particle. Since the shaping time of the HAL25 chip lies in the range between 1.4 μs and 2.2 μs, it is sufficient to keep the laser pulse shorter than 100 ns. By moving the laser beam across the sensor it is possible to study the charge collection by individual strips, measure the charge sharing between the adjacent strips and detect the defected strips that collect no charge or have an abnormal gain.

3.3 Experimental Setup

The setup for scanning the detector modules with an infrared laser beam built at Utrecht University is schematically shown on the Fig. 3.2. The detector module is fixed in a frame holder in such a way that both the sensor p- and n-sides are not obscured and are accessible to the laser light. The laser diode[1] delivers a 20 ns long light pulse with a wavelength of 1060 nm. A 10% fraction of the laser light is selected with a beam splitter and guided through a single-mode optical fiber to the focuser lens[2] which focuses the light on the sensor surface to the spot much smaller than the strip pitch. The remaining 90% of the laser light is supplied to the p-i-n diode which is used for monitoring the laser beam intensity. The end of the optical fiber with the focuser lens is mounted on the xy-table which moves it in the plane parallel to the sensor plane. The distance from the focusing lens to the sensor plane can be adjusted with a screw and is measured with a coupled dial gauge. The xy-table and the module are mounted on the same support and kept in a light-tight box. The translation stages[3] of the xy-table are steered by the motion controller[4] which is programmed from the PC through a standard GPIB interface. The specification positioning accuracy of the translation stages is 3 μm. The part of the setup contained in the light-tight box is depicted in Fig. 3.3. Both hybrids reading p- and n-sides of the SSD module were connected to the EndCap prototype board [7] – the readout board that buffers the analogue and digital output signals from the HAL25 front-end readout chips to the DAQ system and decouples them from the sensor bias voltage. A dedicated unit was used to supply JTAG commands from the PC to the EndCap and HAL25 chips. The DAQ system consisted of a 12-bit ADC card[5] with a sampling frequency set to 10 MHz. The DAQ system could accept a trigger rate up to 100 Hz. The stream of digitized analogue data coming from the ADC and the laser position information were stored on disk in a binary format for off-line analysis. The software that controls the data acquisition and the laser motion was implemented in LabVIEW 7.1.

---

[1] LD-1060 Strained QW Laser Diode by Fermionics Lasertech Inc.

[2] Manufactured by OZ optics, part number LPF-04-1060-9/125-s-1-12-6.2AS-40-3-3-1.5-SP, focal distance 12 mm, the core diameter 9 μm.

[3] CC.5HA translation stages manufactured by NEWPORT, uses DC motor.

[4] MM4005 motion controller manufactured by NEWPORT

[5] ADC DAS 4020/12 card, for full specifications see www.measurementcomputing.com

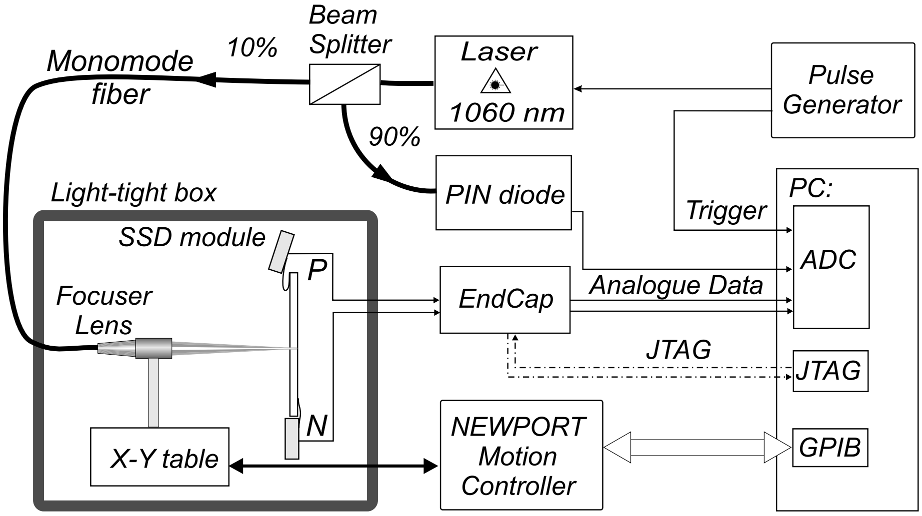

Figure 3.2: The scheme of the laser scanning setup.

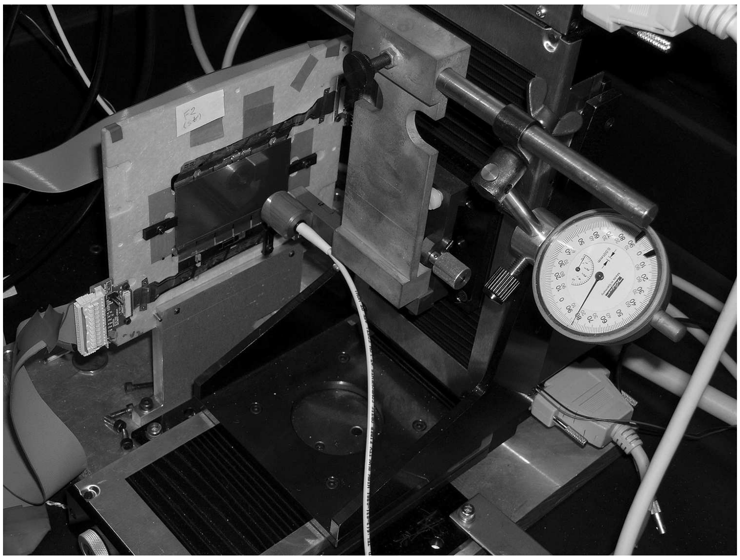

Figure 3.3: The photo shows the SSD module fixed in a frame with a laser beam focuser directed at it. The focuser at the end of the optical fiber is fixed on xy-table which moves it vertically and horizontally. The dial gauge is used to measure the position of the focuser in the direction perpendicular to the sensor plane.

3.4 Setup Calibration and Performance

3.4.1 Laser Beam Spot Size

In order to interpret the scan results correctly, one has to know the width and the shape of the laser beam inside the sensor. The width of the beam at

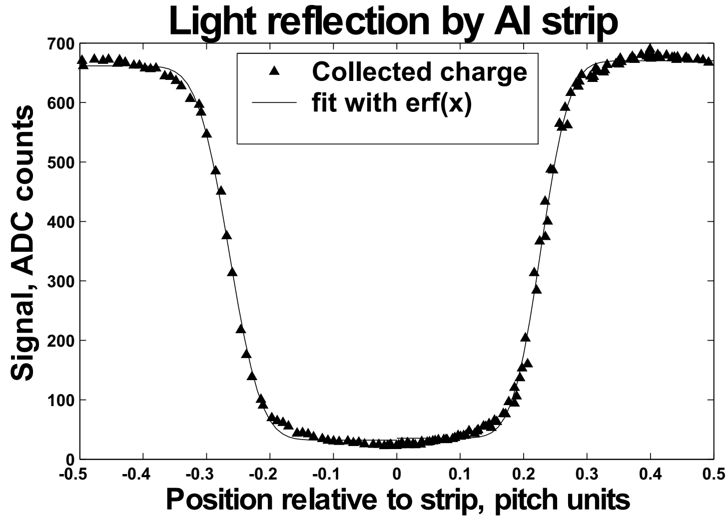

Figure 3.4: The charge collected by the detector, when the laser spot moves over the aluminum strip deposited on the sensor front side.

the sensor surface can be estimated by looking at the variation of the charge collected by the module as the laser spot moves over the aluminum strip deposited on the front surface of the sensor. An example of such a scan is shown in Fig.3.4 which shows the charge collected by the strips around the beam spot, plotted versus the beam position relative to the strips. The diffuseness of the strip shadow, or the transition from the maximum collected charge to zero or minimum charge is determined by the light intensity profile across the beam at the sensor plane. Consider the Gaussian intensity distribution $I(x, y)$ at the beam waist:

$$I(x, y) = I_0 \exp\left(-\frac{2(x^2 + y^2)}{w_0^2}\right) \tag{3.2}$$

where I_0 is the beam intensity on the axis and w_0 is the waist size. The waist size is determined as the distance from the beam axis at which the light intensity drops by a factor $1/e^2$ compared to its value on the axis. If the waist size is much smaller than the width of the aluminum strip, then we can consider the strip as a half-infinite screen, which blocks all the light falling beyond $x = x_0$, where x_0 is the position of the strip edge, parallel to y axis. The amount of light entering the sensor is given by the beam irradiance, integrated over the area not obscured by the strip:

$$\begin{aligned} A &= \int_{-\infty}^{\infty}\int_{-\infty}^{x_0} I(x, y)\mathrm{d}x\mathrm{d}y = I_0\sqrt{\frac{\pi}{2}}w_0 \int_{-\infty}^{x_0} \exp\left(-\frac{2x^2}{w_0^2}\right)\mathrm{d}x \\ &= I_0\frac{\pi w_0^2}{2}\left(\frac{1}{2} + \frac{1}{2}\phi\left(\frac{x\sqrt{2}}{w_0}\right)\right) \end{aligned} \tag{3.3}$$

where $\phi(z)$ is the error function:

$$\phi(z) = \frac{2}{\sqrt{\pi}} \int_0^z \exp(-t^2)\mathrm{d}t \tag{3.4}$$

Therefore in order to determine the beam waist size w_0, the transition function is fitted with an error function with a standard deviation parameter $\sigma = w_0/2$.

Several measurements have been done at different distance between the focusing lens and the sensor surface in order to determine the smallest achievable waist size. The scan that results in the sharpest intensity drop is shown in Fig. 3.4. The waist size obtained from this fit is 6.5 ± 0.4 μm. It can be noticed from this plot that even though the laser spot size is much smaller than the strip width (which is equal to 45 μm for this sensor), the collected charge does not completely drop to zero even when the laser spot is positioned exactly in the middle of the strip. This indicates that there is a significantly large-size halo present around the small concentrated beam spot. However this halo contains not more than 4% of the total beam intensity.

It is essential to keep the beam size small enough though the entire depth of the sensor in order to stay as close as possible to the charge deposition profile of a charged particle. The variation of the size of a Gaussian beam propagating in the medium is given by the equation:

$$w(z) = w_0 \sqrt{1 + \left(\frac{z}{z_R}\right)^2} \tag{3.5}$$

where z is a coordinate along the beam axis and z_R is a Raleigh length given by:

$$z_R = \frac{\pi w_0^2}{\lambda} \tag{3.6}$$

where λ is the wavelength in the medium. The Raleigh length determines the depth of focus of the beam: at $z = \pm z_R$ the beam diameter increases by a factor of $\sqrt{2}$ compared to it's diameter at the waist.

The angular divergence of an ideal Gaussian beam is determined only by it's waist size and the light wavelength. From equation (3.5) one can see that at large distances ($z \gg z_R$, i.e., in far-field region) the beam size scales with z as:

$$w(z) = z\frac{\lambda}{\pi w_0} \tag{3.7}$$

so that the $1/e^2$ irradiance contours asymptotically approach the cone of angular radius θ_0:

$$\theta_0 = \frac{\lambda}{\pi w_0}. \tag{3.8}$$

For a waist size of 6.5 μm this would give an angle of divergence $\theta_0 = 52$ mrad. However the measurements showed [18] that the real full-width-at-half-maximum of the angular intensity distribution of the beam in the present setup is $\theta_R^{\mathrm{FWHM}} =$

5.6°, or given in terms of $1/e^2$ irradiance contour radius, $\theta_R = 83$ mrad. This result can be reconciled with the result given by equation (3.8) by introduction of the beam quality factor M^2. The beam quality factor is defined as:

$$M^2 = \frac{w_{0R}\theta_R}{w_0\theta_0} = \frac{\pi w_R \theta_R}{\lambda} \tag{3.9}$$

where w_{0R} and θ_R are the waist size and the angular divergence of a real beam. The quality factor shows how closely the real beam resembles the ideal Gaussian beam in terms of the relation between the waist size and the far-field divergence. The introduction of the quality factor is based on the fact that for any given laser beam (even those not operating in the TEM_{00} mode) the product of the beam waist radius w_{0R} and the far-field divergence θ_R is constant as the beam propagates through an optical system. For a true Gaussian beam $M^2 = 1$. Most of the lasers have a beam quality factor ranging from 1.1 to 1.7 due to the presence of higher-order modes in the output beam. The equation (3.9) gives $M^2 = 1.6$ for the present laser setup.

The introduction of the quality factor modifies the propagation equation (3.5) in the following way:

$$w_R(z) = w_{0R}\sqrt{1 + \left(\frac{zM^2}{z_R}\right)^2} \tag{3.10}$$

The definition of the Raleigh length stays the same for the real laser beam and becomes:

$$z_R = \frac{\pi w_{0R}^2}{\lambda} \tag{3.11}$$

The $1/e^2$ contour of the beam propagating in the air calculated using equation (3.10) is shown on the Fig.3.5, superimposed are the measurements of the beam size at various distances, described above. The Raleigh length for this beam is $z_R = 128$ μm, indicating that there is a tight tolerance on the alignment between the sensor plane and the xy-table motion plane.

When the laser light passes through the silicon, the beam parameters change due to a change of the light wavelength. For light of 1060 nm wavelength (in vacuum) the refraction index in silicon is 3.6 [12]. Correspondingly, the Raleigh length increases to $z_R^{Si} = 458$ μm, so that for a sensor of the thickness $d = 300$ μm, the beam size at $z = \pm d/2$ increases by 13% to 7.4 μm compare to its waist size. The shape of the beam envelope passing through the sensor is shown on Fig.3.6. One can see that the beam stays small enough through the entire thickness of the sensor and practically all the deposited charge is contained inside the cylinder with a radius of 7.4 μm. The fact that the beam size stays small can be demonstrated by looking at the ability of the laser beam to "resolve" the implanted structures on the front and back side of the sensor. The figures 3.7a and 3.7b show the result of the scan of a rectangular sensor area of the size 0.3×12 mm. The scan steps were 2.5 μm in x-direction (along the longer sensor edge) and 100 μm in y-direction (along the shorter edge). The

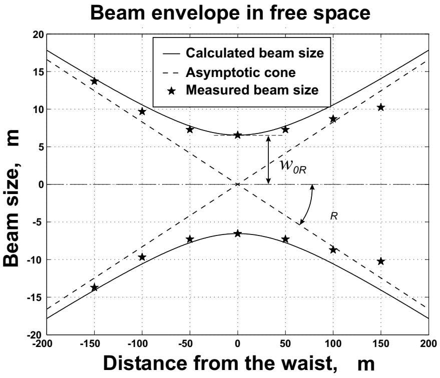

Figure 3.5: The change of the beam size at it propagates in the free space. The solid line shows the $1/e^2$ intensity contour calculated using eq.(3.10), the data points are the measurements. The beam is propagating from left to right.

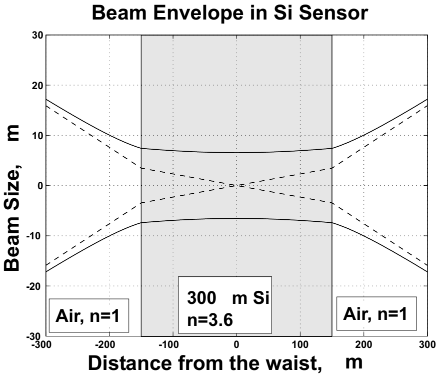

Figure 3.6: Propagation of the laser beam through 300 μm Si sensor. High refraction index in Si changes the beam divergence, not affecting the waist size.

figures show the charge collected from the p-side strips adjacent to the laser beam spot. The intensity of the gray color on the figure represents the amount of the collected charge. When the beam spot moves over the aluminum strip on the front side of the sensor, the light is reflected backwards and no charge is created in the sensor. These regions appear as wide dark strips on these figures. When the light enters the sensor in between the front side strips, but falls on the aluminum strip on the back-side, then the reflected light creates the additional charge inside the sensor. These regions appear highlighted on the figures. If the laser beam passes in between the front and back strips, then the light creates a “nominal” charge in the sensor, and these regions appear gray (more on multiple beam reflection is given in the next subsection). The size of the beam when it enters and leaves the sensor can be estimated from the diffuseness of the contour of the strips on the front and back sides. For the figure 3.7a, the beam was entering the sensor from the p-side and was focused on the depth of 150 μm, in the middle of the sensor bulk. The contours of the front and back strips appear equally diffused. For the figure 3.7b exactly the same area was scanned from the n-side, and the beam was focused of the front surface. The front strips appear sharp, and the back strips are more diffused. One can also see the p-stop implantations on the front side, arranged in three thin lines going along the n-side readout strips.

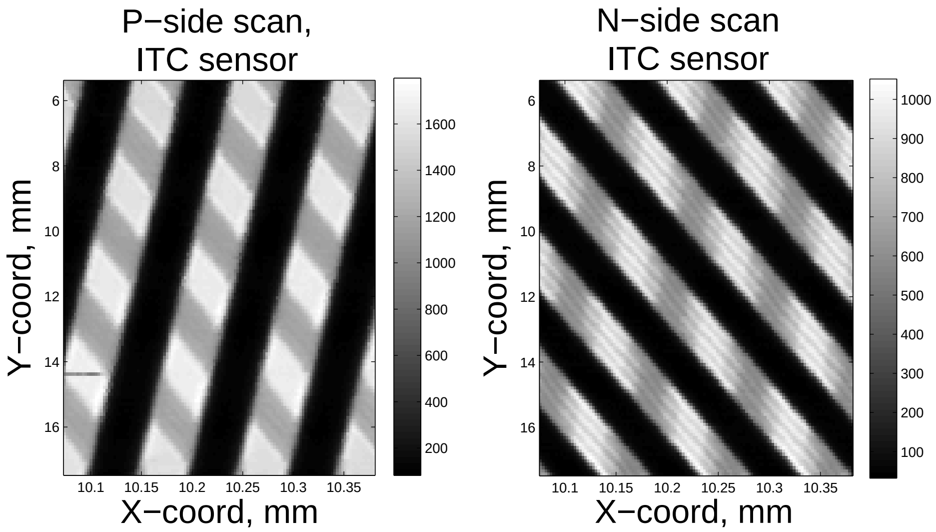

(a) Scan from the p-side (b) Scan from the n-side

Figure 3.7: Scan of the rectangular area 0.3 × 12 mm of a module with ITC sensor. The step size is 2.5 μm in x-direction (along the longer sensor edge) and 100 μm in y-direction (along the shorter sensor edge). The grey color intensity represents the charge (in ADC counts) collected by the front-end electronics from the p-side strips adjacent to the laser beam spot.

3.4.2 Multiple Reflections and Interference in the Si Sensor

The laser light passing through the silicon sensor crosses several boundaries on its way: the boundary between air and the SiO_2 passivation layer and the boundary between the passivation layer and silicon on both front and back sides of the sensor. The refraction index for SiO_2 and Si for light wavelength of 1060 nm is 1.5 and 3.6 respectively [12]. At each of the boundaries there is a partial light reflection which gives rise to multiple internal reflections and interference effects in the passivation and in the silicon bulk itself. The internal reflections in the bulk increase the effective path of the light in the sensor and notably change the charge deposition profile and the total charge deposited in the bulk compared to the single-pass case. The effect is more pronounced if the light is reflected back from the aluminum strips on the back-side. The interference of multiply reflected beams modulates the total amount of light absorbed in the sensor, and hence it modulates the induced charge. In this subsection an estimate is given on how strongly these effects interfere with the measurements of the charge collected by individual strips, and experimental observations of the interference are given.

Light reflectance coefficient of the passivation layer

The reflectance of the SiO_2 passivation layer strongly depends on the layer thickness due to the interference between the beams reflected from the air–SiO_2 boundary and SiO_2–Si boundary. Let's denote the refractive indices of air, silicon oxide and bulk silicon as n_1, n_2 and n_3 respectively. The Fresnel reflection coefficient for normal incidence at the air–SiO_2 boundary equals: $r_1 = (n_1 - n_2)/(n_1 + n_2)$ and at the SiO_2–Si boundary equals: $r_2 = (n_2 - n_3)/(n_2 + n_3)$. Assuming that there is no light absorption in SiO_2 layer, the light intensity reflectance of the passivation layer can be described by the expression:

$$R = 1 - \frac{(1 - r_1^2)(1 - r_2^2)}{(1 - r_1 r_2)^2 + 4 r_1 r_2 \sin^2(\phi/2)} \tag{3.12}$$

where ϕ is the round-trip phase given by:

$$\phi = \pi + \frac{4\pi d_{\mathrm{ox}} n_2}{\lambda} \tag{3.13}$$

where d_{ox} is the oxide thickness and λ is the light wavelength in vacuum. The round-trip phase shows the phase difference between the beam transmitted through the first boundary and the beam reflected back and forth from both boundaries. The reflectance R has a minimum R_{min} when the phase $\phi = 2\pi m$, where m is an integer number. In terms of the oxide thickness, this can be expressed as $d_{\mathrm{ox}} = \frac{\lambda}{n_2}(\frac{1}{4} + \frac{m}{2})$. The first minimum in the reflectance occurs when the thickness of the oxide passivation layer equals the quarter wavelength of light in the oxide. The maxima R_{max} occur when $\phi = \pi(1 + 2m)$ or $d_{\mathrm{ox}} = \frac{\lambda}{n_2}\frac{m}{2}$. From equation (3.12) the minimum and maximum obtainable reflectance is:

$$\begin{aligned} R_{max} &= \frac{(n_1 - n_3)^2}{(n_1 + n_3)^2} = 0.32 && (3.14) \\ R_{min} &= \frac{(n_2^2 - n_1 n_3)^2}{(n_2^2 + n_1 n_3)^2} = 0.053 && (3.15) \end{aligned}$$

The direct measurements [18] resulted in the reflection coefficients $R = 0.341 \pm 0.009$ for ITC sensors and $R = 0.374 \pm 0.002$ for Canberra sensors. A certain discrepancy of the measurements with the estimates might be explained by a presence of a silicon nitride layer in the passivation.

Charge deposition profile and interference in the bulk

In order to estimate the modulation of the created charge due to the light interference in the bulk, we restrict ourselves to a flat wave approximation.The approach taken here is very similar to the one used in calculation of multiple-beam interference in a Fabry-Perot cavity (see for example, Chapter 7.6 of ref.[19]), with the only difference that we are interested in the amount of absorbed light rather then in the transmitted or reflected. Suppose the incoming

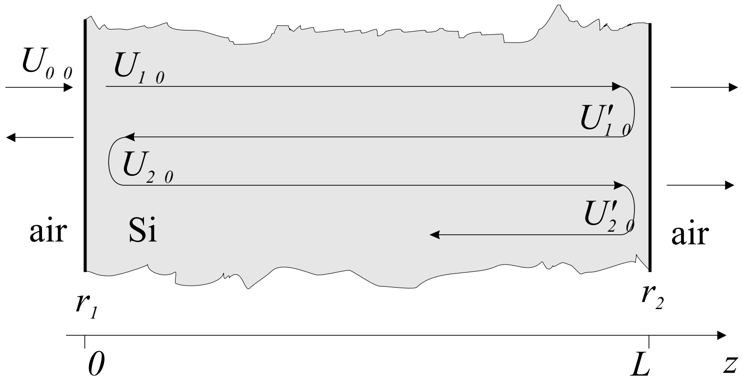

Figure 3.8: Multiple reflections of the laser light in the silicon sensor

light has intensity I_0. Then the monochromatic flat wave travelling along the z-axis and falling normally on the silicon sensor is described as:

$$U(x,t) = U_{00}\, e^{-i(wt-kz)}, \tag{3.16}$$

where $U_{00} = I_0^{1/2}$ is the modulus of the wave amplitude, $k = 2\pi/\lambda_{\mathrm{Si}}$ is a wave vector and λ_{Si} is the light wavelength in silicon. The sensor front-side and back-side boundaries are located at $z = 0$ and $z = L$ (see Fig.3.8), the boundaries are perpendicular to the z-axis. Let the amplitude reflection factors of the boundaries be r_1 and r_2 accordingly (the intensity reflection factors are therefore $R_1 = r_1^2$ and $R_2 = r_2^2$). The modulus of the amplitude of the wave transmitted through the first boundary (at $z = 0$) is:

$$U_{10} = \sqrt{(1 - r_1^2)}U_{00}. \tag{3.17}$$

The wave propagating through the silicon from left to right (see Fig.3.8) is described by:

$$U_1(z,t) = U_{10} \cdot \exp\left[-i(wt - kz) - \frac{z}{2a_0}\right] \tag{3.18}$$

Since the time dependence of the wave $U_1(z,t)$ and all the reflected waves is described by the factor $\exp(-iwt)$, this factor can be dropped for the moment and re-inserted later when the wave intensity is calculated. The complex amplitude of the wave U_1 is then:

$$U_1(z) = U_{10} \cdot \exp\left[ikz - \frac{z}{2a_0}\right] \tag{3.19}$$

The wave reflected from the back-side and travelling backwards towards the smaller z is given by:

$$U_1'(z) = U_{10}' \cdot \exp\left[-ik(z - L) + \frac{(z - L)}{2a_0}\right] \tag{3.20}$$

Using the eq.(3.19), the complex amplitude U'_{10} of this wave at $z = L$ just after reflection is:

$$U'_{10} = U_{10} \cdot r_2 \exp\left[ikL - \frac{L}{2a_0} + i\delta_2\right] \tag{3.21}$$

Here the factor δ_2 describes any phase change after the reflection at the boundary and r_2 shows the drop of the amplitude of the reflected wave. The wave reflected once more from the first boundary and travelling again in the direction of larger x is described by:

$$U_2(z) = U_{20} \cdot \exp\left[ikz - \frac{z}{2a_0}\right] \tag{3.22}$$

where the complex amplitude U_{20} of this wave is:

$$U_{20} = U_{10} \cdot r_1 r_2 \cdot \exp\left[-\frac{L}{a_0} + i(2kL + \delta_1 + \delta_2)\right] \tag{3.23}$$

Here δ_1 and δ_2 are the phase changes after the reflections at the left and right boundaries. The ratio of the amplitudes U_{20} and U_{10} is the round-trip amplitude change:

$$h = \frac{U_{20}}{U_{10}} = re^{i\varphi} \tag{3.24}$$

where

$$r = r_1 r_2 \exp(-L/a_0) \tag{3.25}$$

is the round-trip modulus change and

$$\varphi = (2kL + \delta_1 + \delta_2) \tag{3.26}$$

is the round-trip phase change. In this manner all the multiply reflected waves travelling from left to right can be described as:

$$U_l(z) = U_{10} \cdot h^{l-1} \cdot \exp\left[ikz - \frac{z}{2a_0}\right] \tag{3.27}$$

Adding them all up gives:

$$\begin{aligned} U(z) &= \sum_{l=1}^{\infty} U_l(z) = \sum_{l=1}^{\infty} U_{10} \cdot h^{l-1} \cdot \exp\left[ikz - \frac{z}{2a_0}\right] \\ &= \frac{U_{10}}{1-h} \exp\left[ikz - \frac{z}{2a_0}\right] \end{aligned} \tag{3.28}$$

In a similar manner all the waves travelling backwards add up to:

$$U'(z) = \frac{U_{10}}{1-h} \cdot r_2 \exp\left[-ik(z-2L) + \frac{z-2L}{2a_0} + i\delta_2\right] \tag{3.29}$$

The resulting wave is a superposition of the waves travelling in the positive and negative directions:

$$U_{\text{tot}}(z) = U(z) + U'(z) \tag{3.30}$$

The light intensity, that defines the density of the deposited charge, is obtained by multiplying the wave amplitude with its complex conjugate. Reinserting the factors $\exp(-iwt)$ at this point we obtain:

$$\begin{aligned} I_{\text{tot}}(z) &= U_{\text{tot}}(z)\exp(-iwt)\cdot U^*_{\text{tot}}(z)\exp(iwt) = \frac{I_0(1-r_1^2)}{1+r^2-2r\cos\varphi} \times \\ &\times\left[\exp\left(\frac{-z}{a_0}\right) + r_2^2\exp\left(\frac{z-2L}{a_0}\right) + \right. \\ &\left. +2r_2\cdot\exp\left(\frac{-L}{a_0}\right)\cdot\cos(2kz-\varphi+\delta_1+2\delta_2)\right] \end{aligned} \tag{3.31}$$

One can see from the expression in square brackets in the right part of the equation (3.31) that the light intensity profile decomposes into a sum of three components. The first term: $\exp(-z/a_0)$ is the “usual” intensity attenuation of the direct wave like in the case of a single pass; the second term: $r_2^2\cdot\exp[(z-2L)/a_0]$ describes the intensity attenuation of the light reflected from the back side; and the third term is a standing wave emerging due to the interference of the first two. This last term is a quickly oscillating function with a spatial period of $\lambda_{\text{Si}}/2$, amplitude $2r_2\cdot\exp(-L/a_0)$ and a mean value of zero. However this “fine structure” of the intensity, and hence, of the density of the created charge introduced by the third term has little effect on the measurements because the drift of the carriers in the electric field present in the sensor immediately smears it out. Therefore the depth profile of the charge deposition density can be well approximated by the first two terms:

$$I_{\text{tot}}(z) = \frac{I_0(1-r_1^2)}{1+r^2-2r\cos\varphi}\left[\exp\left(\frac{-z}{a_0}\right)+r_2^2\exp\left(\frac{z-2L}{a_0}\right)\right] \tag{3.32}$$

The Fig.3.9 demonstrates how this profile changes depending on the intensity reflection coefficient $R_2 = r_2^2$ of the back-side. One can see that a larger reflectance makes the density profile more uniform compared to the single-pass deposition profile. The non-uniformity can be described as the relative intensity change over the entire depth of the detector:

$$\frac{I_{\text{tot}}(0)-I_{\text{tot}}(L)}{I_{\text{tot}}(0)} = \frac{e^{L/a_0}-r_2^2e^{-L/a_0}-(1+r_2^2)}{e^{L/a_0}-r_2^2e^{-L/a_0}} \tag{3.33}$$

This gives a value of 31% for a single-pass case with no reflections, 21% for multiple reflections from silicon oxide film and only 7.3% for the case when light is reflected from Al strip on the back-side. The higher beam reflection from the back-side therefore helps to make the charge deposition profile more uniform.

The total charge created in the sensor is obtained by integration of eq.(3.32):

$$\begin{aligned} Q(L) \sim \int_0^L I_{\text{tot}}(z)\mathrm{d}z &= \frac{I_0a_0(1-r_1^2)(1+r_2^2e^{-L/a_0})(1-e^{-L/a_0})}{1+r^2-2r\cos\varphi} \\ &= \frac{I_0a_0(1-R_1)(1+R_2e^{-L/a_0})(1-e^{-L/a_0})}{(1-r)^2+4r\sin^2(\frac{\pi L}{\lambda_{\text{Si}}}+\frac{\delta_1+\delta_2}{2})} \end{aligned} \tag{3.34}$$

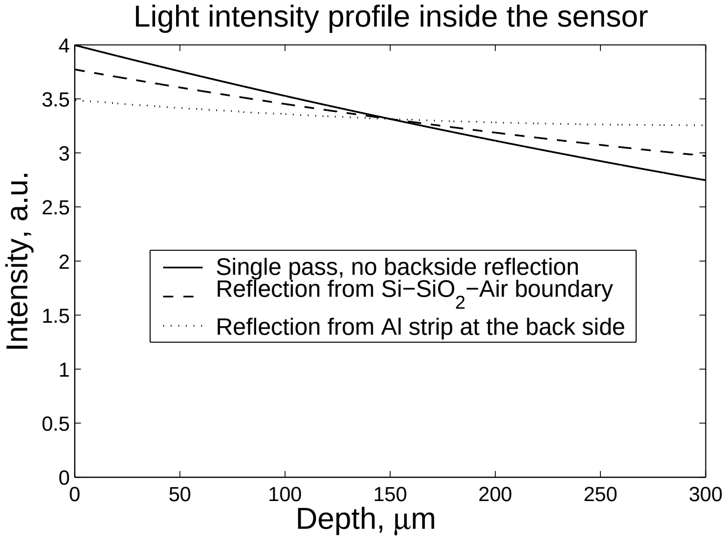

Figure 3.9: Depth profile of the density of charge generated by the laser light. The profile of the deposition is modified by the light reflection from the back-side. Solid curve: no reflection, $r_2 = 0$; dashed curve: $r_2^2 = 0.32$; dotted curve: mirror reflection from Al strip on the back-side, $r_2^2 = 0.96$[14]. The curves are normalized to the same area.

The behaviour of Q as a function of L is shown in Fig.3.10 for two different reflection coefficients R_2. Neglecting the variation of e^{-L/a_0} over a distance of several λ_{Si}, the equation (3.34) can be simplified to

$$Q = \frac{Q_{\max}}{1 + F\sin^2(\frac{\varphi}{2})} = \frac{Q_{\max}}{1 + F\sin^2(\frac{\pi L}{\lambda_{\mathrm{Si}}} + \frac{\delta_1+\delta_2}{2})} \tag{3.35}$$

where the parameter F is defined by the formula

$$F = \frac{4r}{(1-r)^2} \tag{3.36}$$

We can see that the created charge strongly depends on the thickness of the part of the sensor which is probed by the laser beam. The maxima of the created charge occur when the round-trip phase φ, given by eq.(3.26), is a multiple of 2π, i.e. $\varphi = 2m\pi$, and the minima occur when $\varphi = (2m+1)\pi$, where m is an integer number called the order of interference. The spacing between maxima or minima in terms of the sensor thickness traversed by the laser light is half the laser wavelength in silicon, which equals $\lambda_{\mathrm{Si}}/2 = 147$ nm.

The thickness of the silicon bulk varies across the sensor due to the mechanical tolerance of the wafer production. This variation should not exceed 10 μm for the sensors accepted for installation in the ALICE experiment. Therefore if the

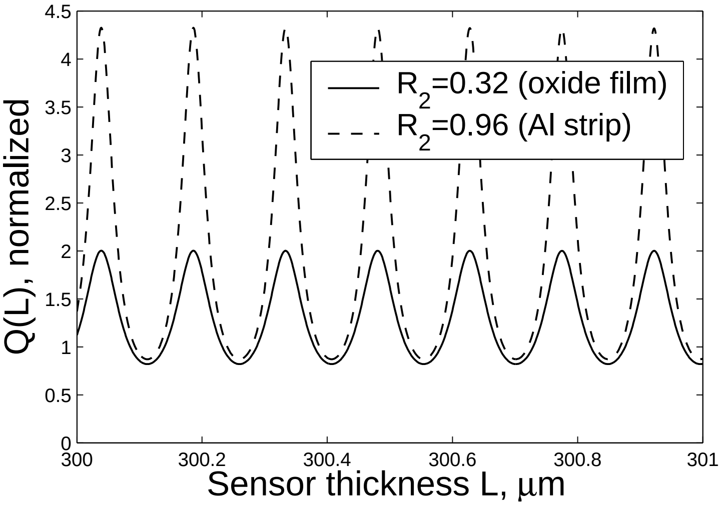

Figure 3.10: The dependence of the created charge Q on the sensor thickness L for monochromatic laser light. Two cases are plotted: a) solid line – back-side reflection is from Si0$_2$ film; b) dashed line – back-side reflection is from aluminum strip. The plotted charge is normalized to the charge that would be created in single-pass case with no multiple reflection, i.e. when $R_2 = 0$.

scan path stretches over a distance where the thickness change is larger then $\lambda_{\mathrm{Si}}/2$, then one should see the modulation of the collected charge in the form of interference fringes. This may complicate the measurement of the gain of individual readout channels if the charge modulation by interference is too high. The degree of the modulation can be characterized by the contrast factor $\mathcal{C}$, which is defined as $Q_{\max}/Q_{\min}$. Using the equations (3.35) and (3.36), the contrast factor for the monochromatic light is expressed as:

$$\mathcal{C} = \frac{Q_{\max}}{Q_{\min}} = 1 + F. \tag{3.37}$$

However the real laser light has a certain spectral width, which results in blurring of the interference fringes, hence in a lower contrast. The fringes should totally disappear when the relative spectral width $\Delta\lambda/\lambda$ is larger than the order of interference m, which can also be written as:

$$m = \lceil 2L/\lambda_{\mathrm{Si}} \rceil \approx 2000. \tag{3.38}$$

For the wavelength of 1060 nm this estimate gives $\Delta\lambda \approx 0.5$ nm. The spectral width of the diode lasers may vary from several nanometers to a fraction of nanometer. According to the specifications of the laser diode used in the present setup, the spectral width of this laser is about 0.1 nm, and therefore the modulation of the created charge due to the interference should be detectable. The dependence of the contrast factor on the spectral width of the incoming light

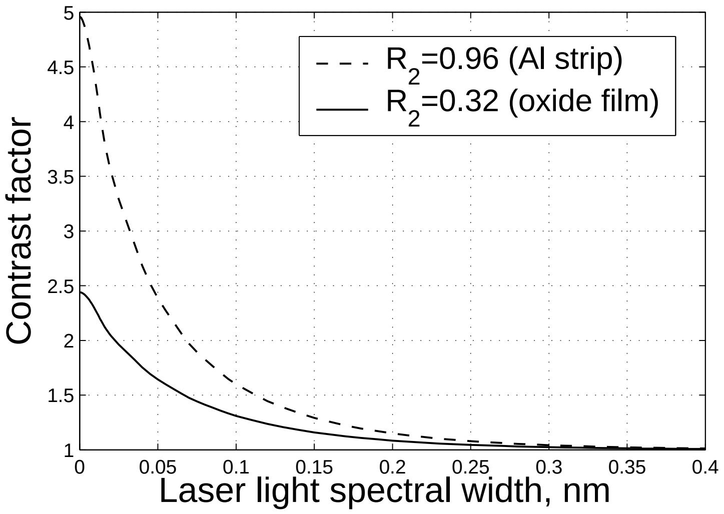

Figure 3.11: The dependence of the contrast factor $\mathcal{C}$ of the interference fringes on the spectral width $\Delta\lambda$ of the laser light. The parameter R_2 stands for the intensity reflection factor of the back-side boundary.

is depicted in the Fig.3.11. This plot is obtained by numerical convolution of the created charge $Q(k, L)$ given by eq.(3.35) with a spectral density of the incoming light $\Phi(k - k_0)$, and then taking the ratio of the maximum to the minimum charge. The spectral density is approximated with a Lorentz distribution:

$$\Phi(k - k_0) = \frac{1}{\pi} \frac{\alpha_{(k)}}{(k - k_0)^2 + \alpha_{(k)}^2} \tag{3.39}$$

where $\alpha_{(k)}$ is the spectral width in the space of the wave vector k, and k_0 is the wave vector corresponding to the middle of the spectral line, $k_0 = 2\pi/\lambda_{\text{Si}}$. It is seen from the Fig.3.11 that contrast factors up to 1.5 can be observed for the spectral width given in the specifications. For the laser with spectral width more than 0.5 nm the interference fringes would completely vanish and cause no modulation of the deposited charge.

Observations of the interference fringes

In order to observe the interference fringes directly and to estimate the degree of the charge modulation, a two-dimensional scan covering almost the entire sensor was performed. A detailed scan of the full sensor area by small steps was not possible due to a large time such a scan would require. Instead of that, a scan trajectory that sparsely covers the sensor was used. This trajectory is schematically shown in Fig.3.12. The trajectory consists of the parallel lines that are running along the full length of front-side strips (approximately

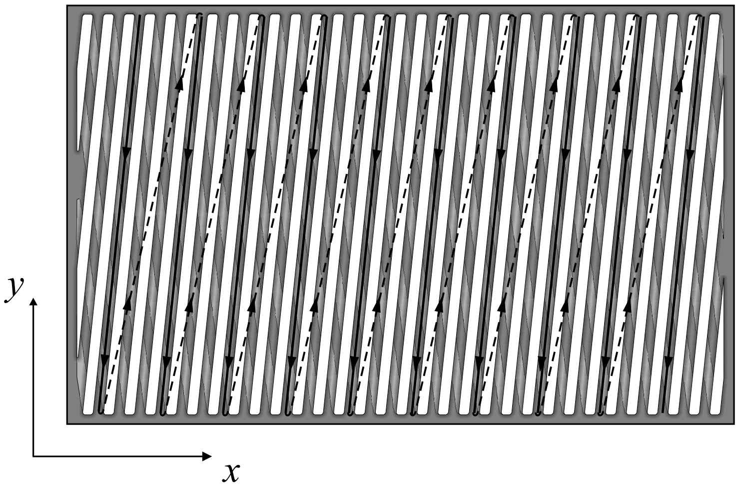

Figure 3.12: The picture schematically shows the scan path that sparsely covers the entire sensor area. The scan trajectory (shown by the solid line) passes in the middle between the front-side strips. The sweeps are spaced by 3 pitch distance. The dashed line connects the consecutive sweep trajectories. The scale and the number of strips are arbitrary.

38 mm). The scan lines are located in the middle between the strips, what distributes the created charge equally between the two adjacent strips. The scan lines were spaced by 3 pitch distance, so that 768/3=256 lines were required to cover the entire sensor area. Each line consisted of 300 equally spaced sampling points. In order to keep the scan trajectory parallel to the strips, the alignment of the sensor with respect to the frame of reference of the xy-table has been measured (this issue is discussed in the section 3.4.4). The charge (in ADC counts) collected by the strips adjacent to the laser beam spot was recorded during the scan. This charge is displayed on Fig.3.13 and Fig.3.14 for Canberra and ITC sensors respectively. A vertical row of pixels on these figures represents the charge collected along one scan line, which contains 300 sampling points. Each scan line crosses 14 back-side strips, so that there are 14 regions where the collected charge is almost doubled due to the reflection from the back-side strips. The position of these regions is periodic and does not change from one scan line to the other, for this reason these regions appear on the figures 3.13 and 3.14 as wide horizontal light-colored bands.

The interference fringes are clearly seen on these two figures. Fringes of the same order of interference follow the lines of equal optical thickness of the sensor. Assuming that the refraction index of the silicon stays constant over the entire sensor (except for the thin implantations), the fringes pattern actually shows the thickness profile of the sensor. One can count about 50 half-ring fringes in Canberra sensor (Fig.3.13) and 7 fringes in ITC sensor (Fig.3.14). Recalling that the spacing between the neighbouring fringes equals 147 nm in

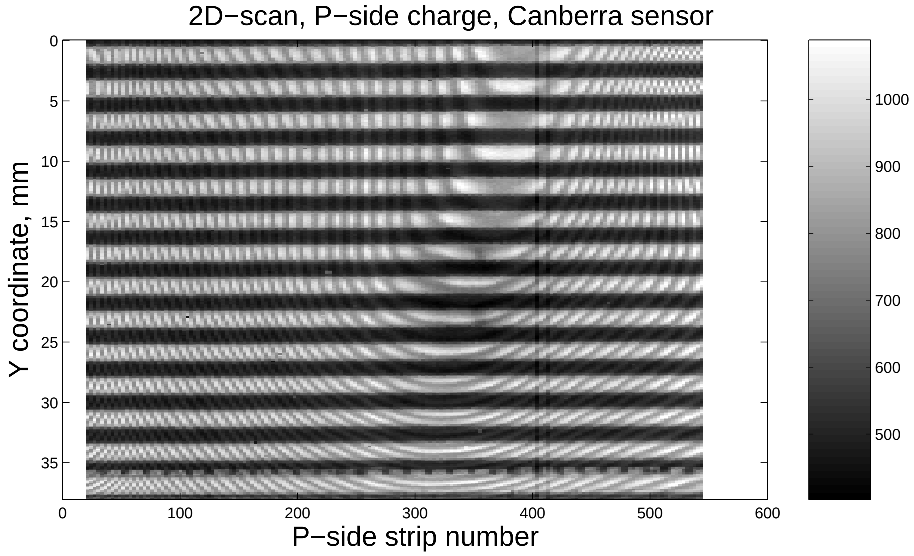

Figure 3.13: 2D-scan of Canberra sensor. The scan trajectory is shown in the Fig 3.12, the sensor was scanned from the p-side. The intensity of the grey color shows the collected charge measured in ADC counts.

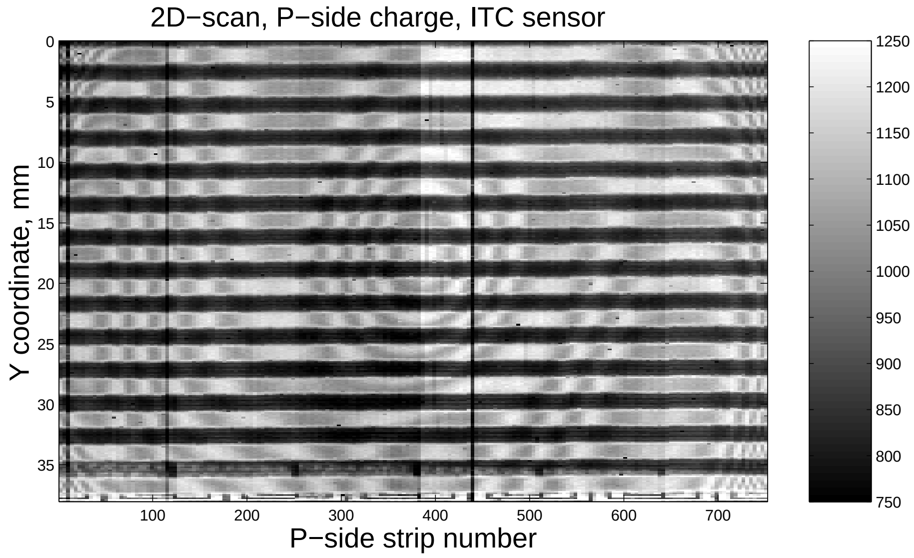

Figure 3.14: 2D-scan of ITC sensor. The scan trajectory is shown in the Fig 3.12, the sensor was scanned from the p-side. The intensity of the grey color shows the collected charge measured in ADC counts.

terms of the sensor thickness change, one obtains the total thickness variation $\Delta L = 7.3\ \mu$m for Canberra sensor and $\Delta L = 1\ \mu$m for ITC sensor. Both values are within the specifications which limit the acceptable thickness variation to 10 μm.

The contrast factor $\mathcal{C}$ observed with Canberra sensor equals $\mathcal{C}_{\rm Al} \approx 1.20$ over the regions where the light is reflected from the back-side aluminium strips, and $\mathcal{C}_{\rm ox} \approx 1.09$ in between the strips. For the ITC sensor (Fig.3.14) these numbers are $\mathcal{C}_{\rm Al} \approx 1.16$ and $\mathcal{C}_{\rm ox} \approx 1.06$ correspondingly. This is consistent with a laser spectral width of about 0.15-0.2 nm, as can be deduced from the Fig.3.11. The lower contrast observed with the ITC sensor indicates that the actual reflection coefficient of the oxide layer is smaller than the one reported in [18].

The contrast factor also gives the limit on the precision of the strip gain measurement. The systematic error of the strip gain measurement G due to the interference effect can be estimated as:

$$\frac{\Delta G}{G} = \mathcal{C}_{\rm ox} - 1 \tag{3.40}$$

if the sensor is probed by the laser beam such that the back-strip reflections are avoided. Applying the eq.(3.40), one obtains $\Delta G/G = 9\%$ for Canberra sensors and $\Delta G/G = 6\%$ for ITC sensors.

3.4.3 Laser Positioning Accuracy

The scan lines that compose the trajectory shown in Fig.3.12 should follow the direction of the front side strips and stay in the middle between the two strips adjacent to the laser beam spot on the front side. In this case the created charge is equally shared between these two strips. In practice the trajectory is slightly different from the desired one because of a limited positioning accuracy of the xy-table and the tolerance of the sensor alignment measurement. The deviation of the actual trajectory can be estimated by measuring the charge division between these two front-side strips. The charge division is characterized by a charge sharing function η, defined as a fraction of the total created charge collected by left or right strip (see Sect.3.5.1 for more details). Assuming it for the left strip we write:

$$\eta_{\rm L} = \frac{Q_{\rm L}}{Q_{\rm L} + Q_{\rm R}} \tag{3.41}$$

where $Q_{\rm L}$ and $Q_{\rm R}$ is the charge collected by left and right front-side strips respectively. In the ideal case, $\eta_{\rm L} = 0.5$ everywhere along the scan line, deviation from this number means that the beam spot came closer to one or the other strip. The example of the dependence of $\eta_{\rm L}$ on the position of the beam spot along the strip (or equivalently, along the sensor shorter edge) is shown on fig.3.15 for one of the scan lines. It is seen from the Fig.3.15 that as the beam spot moves from one end of the strip to the other, the η-function exhibits step-to-step oscillations, superimposed on top of the slowly changing systematic offset. Knowing the explicit dependence of the η-function on the distance u from the center of the beam spot to the center line of the neighboring strips (measured in

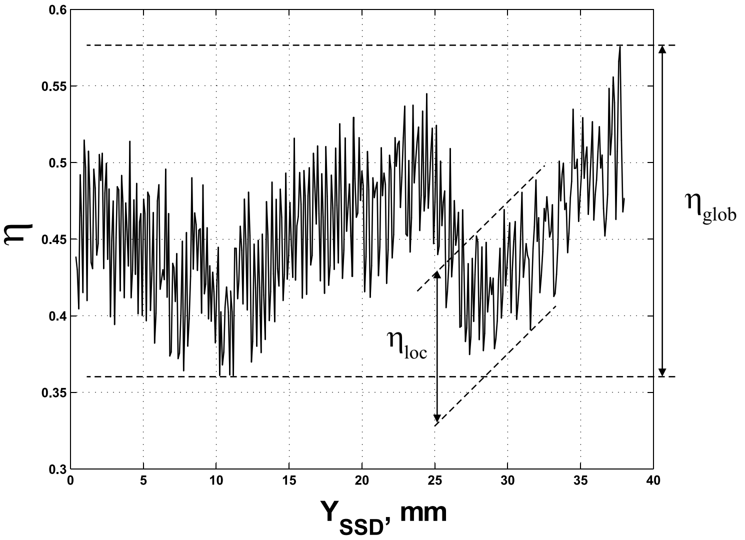

Figure 3.15: Charge sharing function η for the front-side strips obtained during the scan along the front-side strips. The abscissa shows the coordinate along the strip, or equivalently, along the sensor shorter edge.

strip pitch units) in the direction perpendicular to the strip direction, $\eta = \eta(u)$ (see section 3.5.1), one can recalculate the deviation of the scan path from the design trajectory and estimate the positioning accuracy in this way. The step-to-step oscillations of the η-function can be characterized by the amplitude $\Delta\eta_{\mathrm{loc}} = 0.10$, as can be seen from the plot. The global variation of η over the entire travel of 38 mm is limited by $\Delta\eta_{\mathrm{glob}} = 0.22$. Using the fact that the function $\eta = \eta(u)$ is linear near $u = 0.5$ (in pitch units, see fig.3.21a) and the slope $d\eta/du|_{u=0.5} \approx -2.7$, the values $\Delta\eta_{\mathrm{loc}}$ and $\Delta\eta_{\mathrm{glob}}$ result in a local positioning accuracy over a small distance $\Delta u_{\mathrm{loc}} = 3.5$ μm and a positioning accuracy over the entire travel $\Delta u_{\mathrm{glob}} = 8$ μm.

3.4.4 Sensor Alignment

When scanning a particular region of the sensor it is convenient to define the scan trajectory relative to the sensor strips, i.e, define it in the sensor frame of reference. However the NEWPORT motion controller commands should specify the trajectory in the xy-table frame. To make a transition from one frame to the other it is necessary to know the orientation of the sensor in the xy-table frame. The approximate sensor position is known from the design of the detector holders. It is defined with accuracy of about 1 mm in the sensor plane, while the deviation of the sensor plane from the xy-table motion plane does not exceed 10 μm over the entire sensor. The accuracy of 1 mm is not enough to pinpoint, for example, a particular detector strip, for this reason a special routine has been

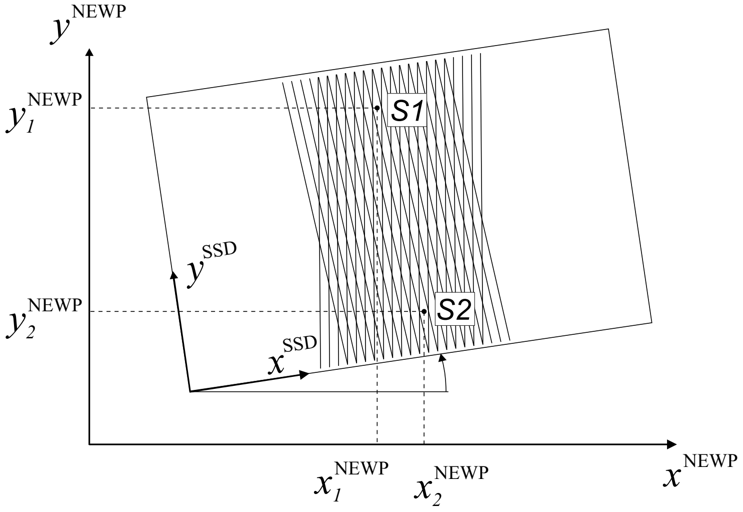

Figure 3.16: Orientation of the sensor in the frame of reference of NEWPORT xy-table.

written to measure the actual orientation of the sensor in the frame holder.

The idea of the alignment method is to correlate the position of the laser beam spot reconstructed from the detector data with the position read back from the motion controller. The sensor displacement can be parameterized by the coordinates of the origin of the sensor frame (x_0, y_0) in the xy-table frame of reference and the rotation angle θ in this plane, here we assume that the xy-table plane of motion and the sensor planes are parallel. The linear transformation from the sensor frame (SSD) to the xy-table frame (NEWP) is given by:

$$\begin{pmatrix} x \\ y \end{pmatrix}_{\mathrm{NEWP}} = \begin{pmatrix} \cos\theta & -\sin\theta \\ \sin\theta & \cos\theta \end{pmatrix} \begin{pmatrix} x \\ y \end{pmatrix}_{\mathrm{SSD}} + \begin{pmatrix} x_0 \\ y_0 \end{pmatrix} \qquad (3.42)$$

It is sufficient to find only two points on the sensor if the position of these points is well defined from the sensor data. For the best accuracy of the measurement of the angle θ, the points should be located as far as possible from one another to ensure a good lever arm. The fact that the position reconstruction error in the direction along the longer sensor edge is much better then along the shorter edge (about 30 times) led the choice of the location of these points on the sensor to the one shown in Fig.3.16 (points S1 and S2). The location with respect to the sensor strips should be chosen such that the position reconstruction error of the beam spot is the smallest and the point is easy to locate. The handy choice is the center O of the diamond formed by intersection of two front and two back strips, shown in Fig.3.17. The center is easy to find because it is not obscured neither by front nor by back-side strips and the charge created in this point is equally shared by the adjacent strips, both on front and back sides. Moreover, since the η function has the steepest slope in the middle between the

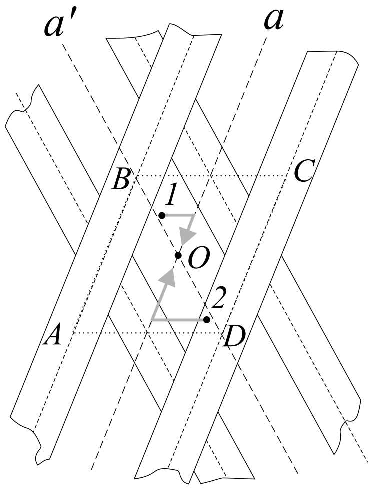

Figure 3.17: Search of the center of the diamond. If the starting point is located anywhere inside the parallelogram $ABCD$, like the points 1 and 2, then following the algorithm described in the text, the laser beam spot will end up in the center O of the diamond. The picture is drawn not to scale.

strips, it is very sensitive to the offset of the beam spot from the middle between the strips.

The center of the diamond is searched as follows: first the laser spot is moved to the starting point which is approximately given by the points S1 or S2 in the Fig.3.16. From that point the closest diamond center should be located. The laser is then moved in small steps along the x-axis of the xy-table (which is roughly parallel to the sensor longer edge) and the module is read out after each step. This is repeated until two conditions are met:

- the signal collected by the strips is sizable;
- the signal is equally shared between the two adjacent strips.

The first condition is needed to make sure that the beam spot is not obscured by the front-side strips and the collected charge is not a noise charge or not the charge created by the laser beam halo. After both conditions are met, the laser spot should be located somewhere on the line a shown on the Fig.3.17. Then the laser beam is moved along this line until the charge collected by the back-strips is also equally shared between the two strips. The center O is assumed to be found if the η-function on the front and back-sides is in the range:

$$0.45 < \eta < 0.55 \tag{3.43}$$

When the diamond center is found, a pair of vectors is obtained: $(x_1, y_1)_{\mathrm{NEWP}}$ – the center coordinates in the xy-table frame, and $(x_1, y_1)_{\mathrm{SSD}}$ – the center coordinates in the sensor frame. The same search procedure is done for the second diamond, resulting in diamond center coordinates $(x_2, y_2)_{\rm NEWP}$ in the xy-table frame and $(x_2, y_2)_{\rm SSD}$ in the sensor frame. Using eq.(3.42) we may write:

$$\begin{pmatrix} \Delta x \\ \Delta y \end{pmatrix}_{\rm NEWP} = \begin{pmatrix} \cos\theta & -\sin\theta \\ \sin\theta & \cos\theta \end{pmatrix} \begin{pmatrix} \Delta x \\ \Delta y \end{pmatrix}_{\rm SSD} \tag{3.44}$$

where $\Delta x = (x_1 - x_2)$ and $\Delta y = (y_1 - y_2)$ are the coordinate differences in both sensor and xy-table frames. The rotation angle θ is found from the eq.(3.44) as:

$$\theta = \tan^{-1}\left(\frac{\Delta x_{\rm N}\Delta y_{\rm S} - \Delta x_{\rm S}\Delta y_{\rm N}}{\Delta x_{\rm N}\Delta x_{\rm S} + \Delta y_{\rm N}\Delta y_{\rm S}}\right) \tag{3.45}$$

where the indices S and N are the shorthand notations for SSD and NEWPORT. The origin coordinates of the sensor frame is obtained from eq.(3.42) as:

$$\begin{pmatrix} x_0 \\ y_0 \end{pmatrix} = \begin{pmatrix} x_1 \\ y_1 \end{pmatrix}_{\rm NEWP} - \begin{pmatrix} \cos\theta & -\sin\theta \\ \sin\theta & \cos\theta \end{pmatrix} \begin{pmatrix} x_1 \\ y_1 \end{pmatrix}_{\rm SSD} \tag{3.46}$$

The alignment parameters were measured each time the sensor was installed or moved in the holder, the parameters were added to the header of the scan data files used for off-line analysis. Using the alignment corrections, any point on the sensor can be pinpointed with accuracy better then 10 μm.

3.5 Module Performance Studies

3.5.1 Charge Sharing Measurement

The division of the charge between the sensor strips is an important property of the silicon strip detector, the laser scanning station offers a convenient way to measure it. At normal incidence of the charged particle or the laser beam, the charge on each sensor side is collected by not more than two adjacent strips located around the particle trajectory impact point or the laser spot. The charge sharing in this case can be characterized by the η-function, defined as a fraction of the total charge collected by one of the two strips closest to the beam axis:

$$\eta_{\rm L}(x_0) = \frac{Q_{\rm L}(x_0)}{Q_{\rm L}(x_0) + Q_{\rm R}(x_0)} \tag{3.47}$$

where x_0 is the laser beam coordinate measured with respect to the left strip center, $Q_{\rm L}(x_0)$ is the charge collected by the left strip and $Q_{\rm R}(x_0)$ - by the right strip. It is convenient to normalize the laser beam coordinate to the strip pitch. The normalized coordinate u is then:

$$u = \frac{x_0}{s} \tag{3.48}$$

where $s = 95$ μm is a strip pitch. The position $u = 0$ corresponds to the centerline of the left strip and $u = 1$ to the right strip.

Measurements of η-function

The charge sharing functions for the p- and n-sides of the module were measured by moving the laser spot from one strip to the other in small steps and recording the signal induced on the strips. To avoid the beam reflections by the strips on the front side, the scanning path was parallel to the front-side strips and stretched from the center of one back-side strip to the center of the next one, this allowed to explore the full range of u-coordinates from 0 to 1. In this way the η-function of the p-side was measured by scanning the module from the n-side and vice versa for the other side. For these measurements the laser beam was focused in the middle of the sensor thickness, as shown in the Fig.3.6, in order to minimize the beam divergence. The example of the η-function measured in this way is shown in Fig.3.18 One can see that the if the laser beam is located in the middle between the strips (at $u = 0.5$) then the charge is equally shared by the adjacent strips, while if it is located at the centerline of the strip (at $u = 0$ for the left strip or at $u = 1$ for the right strip) then practically all the charge is collected by that strip. The capacitive coupling between the strips makes a certain fraction of the charge visible on the adjacent strips, for this reason the η function does not reach 1 or 0.

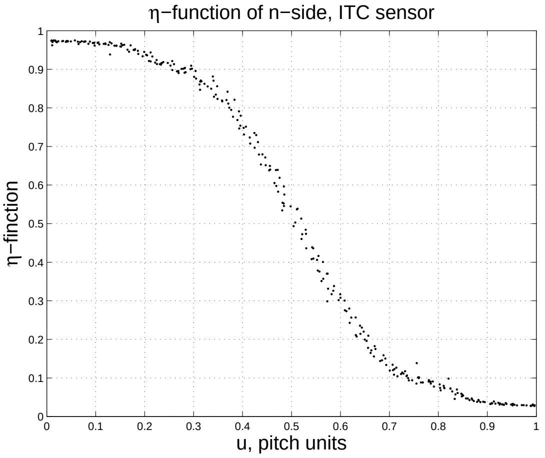

Figure 3.18: n-side η-function obtained by scanning the ITC sensor from the p-side.

Model Calculations

The shape of the η-function can be explained by a model calculations described in refs.[15, 14]. The model predicts the shape of the charge cloud when it arrives at the sensor strips and from this shape the signal induced on the strips is calculated. The coordinates used in the model are shown in Fig. 3.19. The x axis is perpendicular to the strips and lies in the plane of the sensor surface.

The center of the laser beam is positioned at $x = x_0$, the beam is parallel to the the z-axis which is normal to the sensor surface, the coordinate $\xi = x - x_0$ is parallel to x and is measured with respect to the beam center.

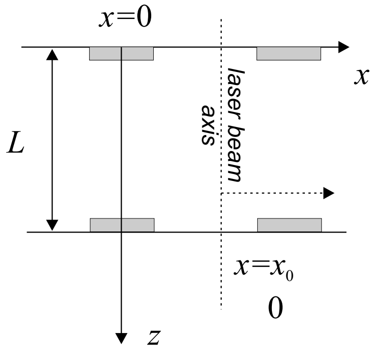

Figure 3.19: Coordinates system used for model calculation. The laser is positioned at $x = x_0$, the coordinate ξ is measured with respect to the laser beam axis.

In this model the electric field inside a fully depleted sensor is parallel to z axis and is given by:

$$E_z = \frac{U_B - U_D}{L} + \frac{2U_D z}{L^2} \tag{3.49}$$

where U_D is the depletion voltage and U_B is the bias voltage, L is a sensor thickness. The drift of the charge carriers in the electric field is described by:

$$\frac{dz}{dt} = \mu_h E_z(z) \qquad\qquad \frac{dz}{dt} = -\mu_e E_z(z) \tag{3.50}$$

where μ_h and μ_e are the hole and electron mobilities, equal to $\mu_h = 450$ cm^2/Vs and $\mu_e = 1350$ cm^2/Vs [16]. The time it takes for a hole or electron created at the depth z to reach the readout strip located at $z = L$ or $z = 0$, respectively, is obtained by integrating these equations:

$$t_h(z) = \frac{L^2}{2\mu_h U_D} \cdot \ln\left(\frac{(U_B + U_D)L}{(U_B - U_D)L + 2U_D z}\right) \tag{3.51}$$

$$t_e(z) = \frac{L^2}{2\mu_e U_D} \cdot \ln\left(1 + \frac{2U_D z}{(U_B - U_D)L}\right) \tag{3.52}$$

For the bias voltage U_B=30 V and the depletion voltage U_D=12 V the maximum drift time for holes is $t_h = 75$ ns and for electrons $t_e = 25$ ns. The depletion voltage U_D was determined as the voltage level at which the strips on the n-side become electrically isolated, this is observed as a sharp noise level drop on the n-side strips. The values U_B and U_D used in the calculations were obtained after the correction for the punch-trough voltage drop between the bias ring and the implanted strips, which was known from the bare sensor measurements.

The shape of the electron (hole) charge cloud created at depth z and arriving at the sensor n-side (p-side) is given by:

$$f_{e(h)}(x) = \frac{1}{\sqrt{2D_{e(h)}t_{e(h)}(z) + \delta^2}} \cdot \exp\left(\frac{-(x-x_0)^2}{4D_{e(h)}t_{e(h)}(z) + 2\delta^2}\right) \tag{3.53}$$

where δ is the primary r.m.s. width of the charge cloud before diffusion, $D_e(h)$ is the electron (hole) diffusion coefficient. In order to obtain the shape of the cloud created by the laser beam, eq.(3.53) has to be convoluted with the charge deposition density $\frac{dQ}{dz}$. This density is obtained from eq.(3.32)[6]:

$$\frac{dQ(z)}{dz} = \frac{\exp\left(-\frac{z}{a_0}\right) + R_2 \exp\left(\frac{z-2L}{a_0}\right)}{a_0\left(1-\exp\left(-\frac{L}{a_0}\right)\right)\left(1+R_2\exp\left(-\frac{L}{a_0}\right)\right)} \tag{3.54}$$

The shape of the cloud of holes and electrons created by the laser beam when they arrive at the sensor strips is:

$$f_{e(h)}(x) = \frac{1}{L\sqrt{2\pi}} \cdot \int_0^L \left[\frac{dQ(z)/dz}{\sqrt{2D_{e(h)}t_{e(h)}(z) + \delta^2}} \cdot \exp\left(\frac{-(x-x_0)^2}{4D_{e(h)}t_{e(h)}(z) + 2\delta^2}\right)\right] dz \tag{3.55}$$

These cloud shapes are shown in Fig.3.20a and Fig.3.20b for electrons and holes respectively. For comparison, the cloud shapes created by a minimum ionizing particle with a uniform charge deposition profile are also plotted in the same figures. The primary r.m.s. width of the deposited charge cloud is $\delta = 1.4\ \mu$m for a MIP particle [15] and $\delta = 3.7\ \mu$m for the laser beam (see Fig.3.6). One can see that the width of the distributions for MIP and laser-induced charges are very close to one another and that this width is not determined by the primary width δ but rather by the diffusion process.

The signals induced on the strips adjacent to the laser beam spot are given by the expressions:

$$Q_{\mathrm{L}}(x_0) = (1-\beta)\int_{-\infty}^{s/2} f_{e(h)}(x)dx + \beta/2\int_{s/2}^{+\infty} f_{e(h)}(x)dx \tag{3.56}$$

$$Q_{\mathrm{R}}(x_0) = \beta/2\int_{-\infty}^{s/2} f_{e(h)}(x)dx + (1-\beta)\int_{s/2}^{+\infty} f_{e(h)}(x)dx \tag{3.57}$$

where $1-\beta$ is the coefficient that represents the charge transfer efficiency from the strip to the amplifier, the remaining fraction β goes to the adjacent strips. This efficiency given by the ratio of the AC coupling capacitance of the sensor strip C_{ac} and the sum of this capacitance with the total capacitance C_{tot} of this strip to the outside world:

$$1-\beta = C_{\mathrm{ac}}/(C_{\mathrm{ac}} + C_{\mathrm{tot}}) \tag{3.58}$$

---

[6] The normalization of $\frac{dQ}{dz}$ in eq.(3.54) is chosen such that $\int_0^L(\frac{dQ}{dz})dz = 1$

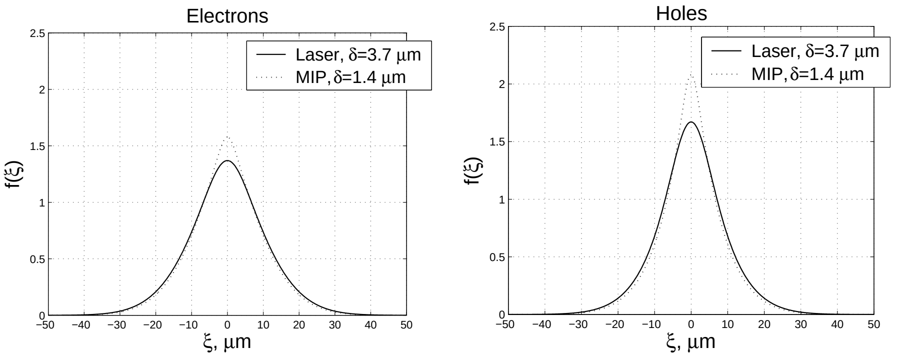

(a) Distribution of electrons

(b) Distribution of holes

Figure 3.20: The distribution of the density of the charge carriers when they arrive at the readout strips, calculated according to eq.(3.55). The dotted line describes this distribution for a MIP particle, when the charge deposition profile dQ/dz is uniform in depth and the primary r.m.s. width of the deposited charge cloud is $\delta = 1.4$ micron. The solid line describes the distribution for the laser induced charge, with dQ/dz given by eq.(3.54) and the primary width $\delta = 3.7$ micron. The laser light was coming from the n-side in case the hole drift is considered and from the p-side in case the electrons are considered.

The total capacitance C_{tot} is approximately given by the sum of the interstrip capacitance to the nearest (I) and next to nearest (II) neighboring strips and the capacitance to the back-side of the sensor:

$$C_{\text{tot}} \approx 2C_{\text{is}}^{(\text{I})} + 2C_{\text{is}}^{(\text{II})} + C_{\text{strip-back}} \tag{3.59}$$

The signals Q_{L} and Q_{R} were used to calculate the charge sharing function $\eta = \eta(x_0)$ and fit this function to the data, using β as a fit parameter. The fits of the η-function to the measurements done for ITC and Canberra sensors are shown in Fig.3.21a and Fig.3.21b. The figures show n-side η-functions obtained by scanning the sensors from the p-side. For these measurements the bias voltage applied to the sensors was only several volts higher than the depletion voltage. In this voltage region the model agrees with the measurements reasonably well. However at higher depletion voltage the model predicts more steep η-functions than actually obtained from the measurements. The Fig.3.22 shows the model predictions and the measured η-functions for p- and n-sides of the ITC sensor, obtained at U_B=88 V. At higher bias voltage the the diffusion plays a smaller role in the charge motion, and the charge drift is governed mostly by the field configuration inside the sensor. However the model uses an oversimplified description of the electric field: the field near the sensor surface is not described by eq.(3.49) because the field lines should end at the implanted strips, and the field in that region is not parallel to z-axis. This results in a less accurate prediction of the η-curves. A 3-D model of the electric field has

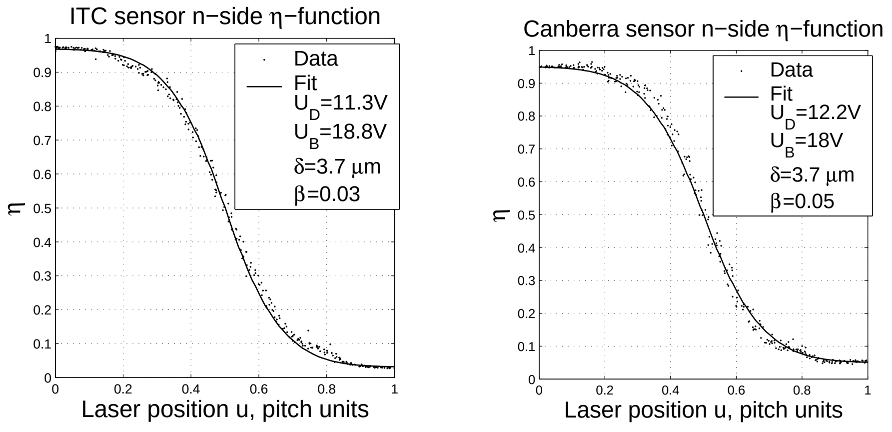

(a) ITC sensor

(b) Canberra sensor

Figure 3.21: The η-functions measured for the ITC and Canberra sensors, with the bias voltage only a few volts higher than the depletion voltage. The fitted curves are the model calculations, the fit parameter is the capacitive coupling β.

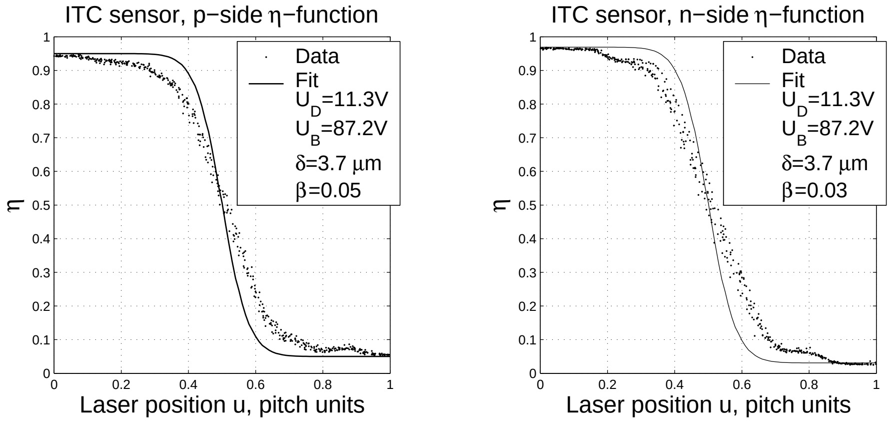

(a) p-side

(b) n-side

Figure 3.22: Scan at higher depletion voltage. The measured η-functions are less steep than the model predictions.

to be considered to describe the charge sharing more accurately, however this is outside the scope of this thesis.

3.5.2 Detection of the Module Defects

The major parameters that characterize the performance of each individual readout channel are the channel gain and noise. The channel gain is defined as a proportionality factor between the charge created in the sensor and collected by the strip of that channel and the output signal produced by the front-end electronics. Various production defects can affect these parameters, it is therefore essential to control the functionality of the readout channels at various production stages and before the installation of the module in the experiment. Laser scanning of all the module strips has been done with all the prototype modules and first production modules. In this subsection the scan results are given and the signatures of the most frequent defects are discussed.

Scan Path

The scan path is a straight line running parallel to the sensor longer edges and passing through the middle of the sensor (see Fig.3.23). The scan steps are equal to the strip pitch, the measurement points are located in the centers of the diamonds created by intersection of the front- and back-side strips, so that the created charge is equally shared between the two adjacent strips on both p- and n-sides at the same time. Each sensor strip gives the signal twice during the scan – once when the laser spot is positioned in between this strip and it's left neighbour and at the next step when the spot moved to the middle between the strip and its right neighbour. The strip gain is estimated as an average over these two signals, measured at a certain laser intensity. The example of the results of such a scan are shown in Fig.3.24. The laser intensity was tuned such that

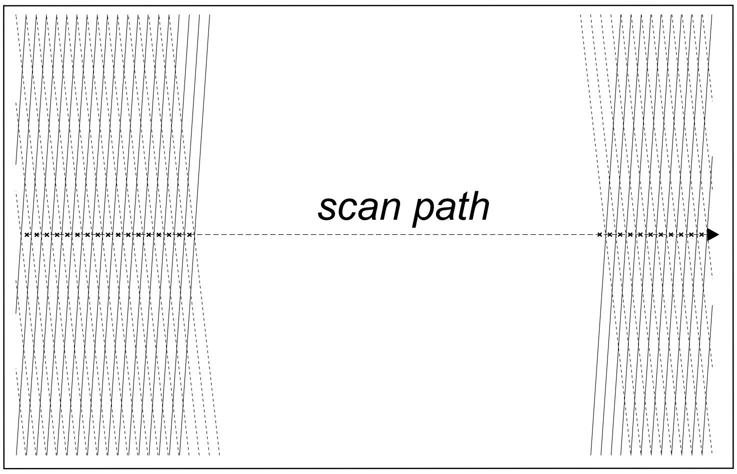

Figure 3.23: Scan path used to measure the gain of all the sensor strips (except for the short ones). The measurement points are marked with crosses. Strips in the middle are not shown, the strips are plotted not to scale.

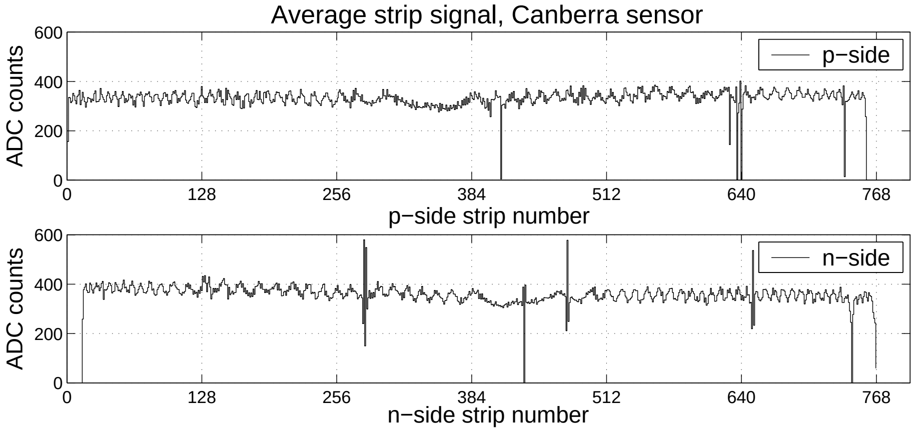

Figure 3.24: Average module strip signal obtained during the scan across the sensor strips.

the deposited charge was approximately equal to 50000 e^- what corresponds to about twice the charge deposited by a MIP particle. One can see from the figure that there is a ripple-like variation of the collected charge with some strips producing anomaly low or high signal. The ripple obviously comes from the light interference in the sensor (see Fig.3.13 for a 2D scan of this sensor and Fig.4.11 “Module 1” on page 71 for gain measurements with particles) and the abnormal gain is a result of the strip defects.

Signature of the disconnected strips

The aluminum sensor strips are connected to the input channels of the HAL25 chips by use of aluminum microcables. A failure of the bonding process on either side of the cable trace (at the chip side or at the sensor side) results in the sensor aluminum strip having a floating potential. For the properly bonded strip the major fraction of the charge collected by this strip flows directly to the input of the charge-sensitive amplifier of the HAL25 chip, and a little fraction β (see eq.3.56) flows to the neighboring channels. When the strip is disconnected from the chip, the entire charge flows to the neighboring channels thanks to the capacitive coupling between the implanted sensor strips. The signal distribution in this case is illustrated in the Fig.3.25. This figure shows the signal read out from the strips around (and including) the disconnected strip number 434, with the laser beam spot located in the middle of this strip and illuminating it from the back-side. One can see that the disconnected channel produces no signal, the largest fraction ($\approx 73\%$) of the created charge is collected by the two strips adjacent to the disconnected strip, and 11% by the strips next to them, the rest is distributed over more distant strips. It should be mentioned in this context that although the disconnected strips collect no charge by themselves, the reconstruction of the particle hits is still possible using the charge flowing

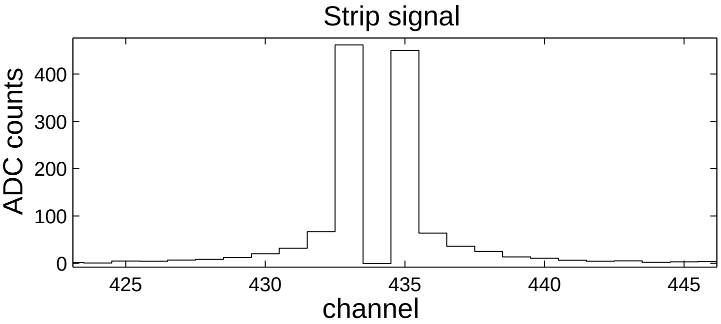

Figure 3.25: Strip signals recorded with laser beam spot located at the center of the strip 434, which is disconnected from the chip input. The charge flows to the neighboring strips which are capacitively coupled to the disconnected strip

to the neighboring strips. The reconstructed cluster charge is smaller in this case because the fraction of charge that flows to the more distant strips (next to nearest neighbors and further) may be lost in the noise and not included in the cluster (see Sect.4.3.2 for mode details on the cluster reconstruction).

The disconnected strips are easily detectable with the laser scan. The upper plot in the Fig.3.26 shows a fragment of the results of the gain measurements in the region around the disconnected strip on the n-side. The strip number 276 is disconnected and the corresponding channel of HAL25 chip produces no signal when the laser creates a charge around this strip. The nearest neighbor strip

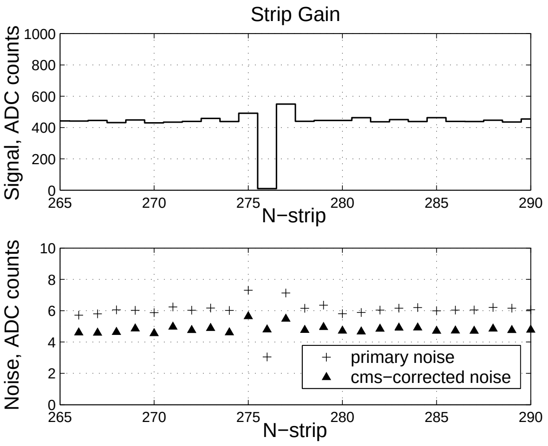

Figure 3.26: Fragment of the gain scan

(for example, the strip number 275) collects more charge than it would normally do because the charge it collects in this case is the sum of the two components:

1). a half of the total created charge, which it would collect no matter whether the strip next to it is disconnected or not.

2). ≈ 36 % of the charge collected by the disconnected strip, which flows to the strip 275 due to the capacitive coupling (see Fig.3.25).

The lower plot in the Fig.3.26 shows the the noise figures for the same strips as the upper plot. Two kinds of noise estimates are shown: the primary noise and the common mode corrected noise. The primary noise is an r.m.s. of the signal read out from the strip when no charge is externally induced in the sensor around this strip. The common mode corrected noise is an r.m.s. of the strip signal from which the mean signal of the strips of the same chip in the event is subtracted (see Sect.4.3.1 for more details on the noise determination). The primary noise of the disconnected channel is significantly smaller compared to the other channels because of the smaller input capacitance loaded to the input of the charge-sensitive amplifier of this channel. In addition, the thermal noise charge generated in the sensor is not seen by the disconnected channel, but is collected by the neighboring channels. The level of the common mode corrected noise of the disconnected channel is typically larger than the level of its primary noise, as opposed to the case with the channels connected to the sensor strips. The common mode component which mainly comes from the noise of the sensor bias voltage, is not present in the signal of the disconnected channel, and subtracting it from the signal effectively adds it to the signal and results in a higher noise level. The noise pattern shown in the Fig.3.26 is observed for all the disconnected strips and this pattern can be used to detect the disconnected strips using the noise data only.

Signature of the defected AC capacitors

At normal operation, the integrated AC-coupling capacitors C_{AC} filter out the DC component of the current flowing to the input of the charge-sensitive amplifier. The potential across the capacitor (between the points A and B on the *p*-side and between the points D and C on the *n*-side, see Fig.3.27) is determined by the difference between the potential of the input of the amplifier with respect to the HAL25 chip ground line (point D versus F and point A versus E) and the potential of the implanted sensor strip with respect to the sensor bias ring (point C versus F and point B versus E). The bias ring and the ground line of the chip on the same sensor side are connected together. The bias voltage V_{B} is applied between the points E and F which mark the bias rings of *p*- and *n*-sides respectively, while the potential U_B across the implanted strips (see eq.3.49) is measured between the points B and C. This potential is smaller than V_{B} by the voltage drop on punch-through channels, represented in the Fig.3.27 by resistors $\mathrm{R}^{p}_{\texttt{p-th}}$ and $\mathrm{R}^{n}_{\texttt{p-th}}$.

If the insulation between the plates of the integrated capacitor C_{AC} is not perfect due to, for example, production defects, damaging of the oxide during the microcable bonding process, then a certain current will flow across the capacitor into the amplifier of the channel to which it connects. This changes the voltage

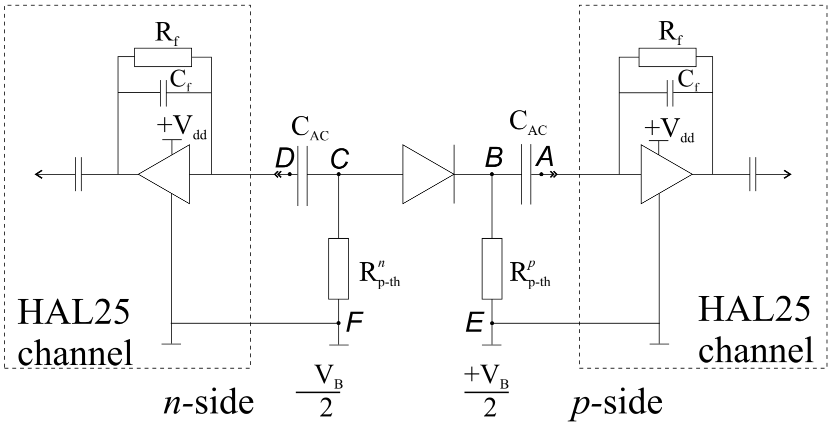

Figure 3.27: Module bias circuit and front-end electronics.

drop across the capacitor and the potential of the implanted strip with respect to its neighbors, leading to a local distortion of the electric field in the bulk around the strip. A number of such defects were found on the n-side of the modules with both ITC and Canberra sensors. These defects are easily identified by the characteristic gain pattern, which is shown in the Fig.3.28. The strips 410, 429, 436 and 450 have abnormally high gain, while their nearest neighbors have a notably smaller gain than the other strips. This gain pattern is explained by the distortion of the η-function around the defected strips. The upper plot of the Fig.3.29 shows the measurement of the charge sharing function around the strip 475 which has a gain pattern similar to the one of the above mentioned strips. The plot was obtained by scanning the sensor from the p-side parallel to the p-side strips, across several n-side strips. The strips from 472 to 478 were explored, one can see from the figure that the charge sharing function η_{L} determined by eq.3.47 is different around the strip 475 compared to the other strips. For this strip the point where the charge is equally shared among the neighboring strips (where $\eta_{\mathrm{L}} = 0.5$) is shifted towards the neighboring strips by approximately 0.15 pitch units or 14 μm. This means that the strip 475 collects the charge from a larger volume at the expense of the adjacent left and right strips. Since for the gain scan the laser is positioned in the middle between the strips, a larger fraction of the charge goes to strip 475 than to its neighbors. The lower plot in the Fig.3.29 shows the total charge collected by left and right strips together, both for p-side and n-side, plotted versus the laser spot coordinates measured with respect to the n-side strips. The meander-like shape of the plot is due to the light reflection from the Al strips on the n-side. It is seen from the figure that while the p-side charge collected at the strips 474, 475 and 476 is roughly equal, the n-side charge collected from the strip 475 is about 20% smaller than at the neighboring strips, indicating the lower gain of the strip 475. Nevertheless the strips with the above described defect can be used to reconstruct the charge clusters, although the center of gravity of the

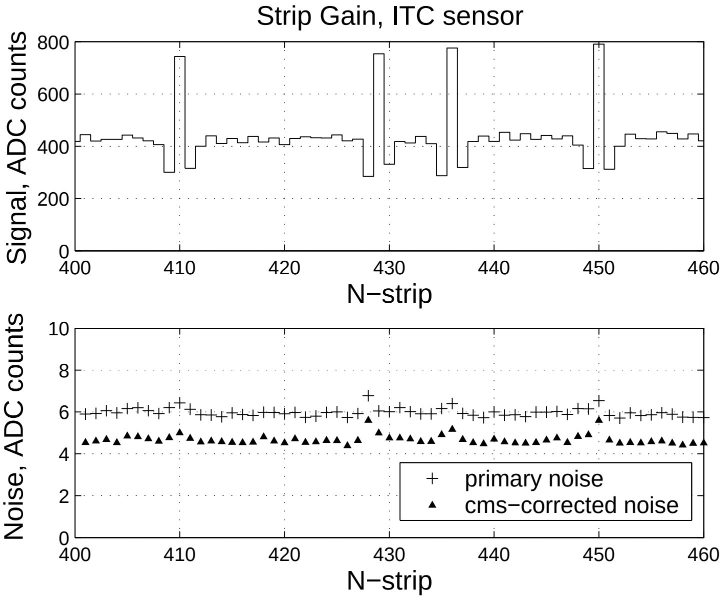

Figure 3.28: A fragment of the gain scan, showing the characteristic pattern produced by defected AC capacitors.

reconstructed cluster has a systematic offset due to the distorted electric field in the region around the strip.

3.6 Conclusions

The laser scanning station has been constructed and used for the performance studies and quality control of the silicon strip detector prototype modules. The beam of the collimated laser light with the wavelength 1060 nm gives the detector response comparable with the response to the minimum ionizing particle. The convenience of the laser scanning station compared to the tests with beam particles is the compactness of the setup and the ease of control of the amount and location of the deposited charge.

The interference of the laser light in the sensor bulk modulates the amount of the deposited charge and decreases the accuracy of the strip gain measurement, but on the other hand allows to measure the thickness variation of the sensor. The interference effect can be eliminated by using a laser with a spectral width larger than 0.5 nm.

At the stage of prototyping and early stage of the mass production the laser station showed to be a convenient tool which allowed to measure the basic performance parameters of the modules and detect the defected strips. The information obtained by the laser scans of the defected areas was complementary

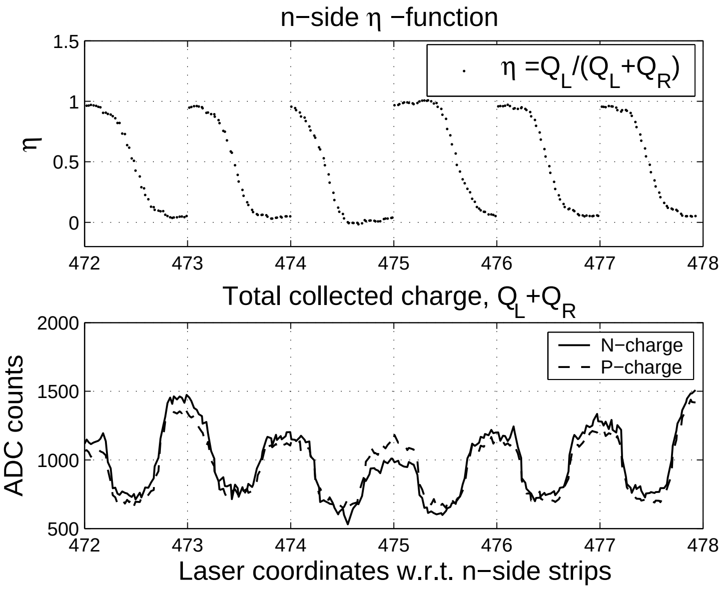

Figure 3.29: Scan along the p-side strips of the region around the defected strip 475 of the n-side.

to the information obtained from the noise measurements and measurements with the internal pulser of the front-end amplifiers. The laser scan information was essential for a proper interpretation of the results given by the last two methods and eventually made possible to detect the defects only using the noise information and the internal pulser.

Chapter 4

Beam Test of the Prototype Silicon Strip Detectors

4.1 Introduction

The major parameters that characterize the performance of silicon strip detectors used for the reconstruction of charged particle tracks are the hit position resolution, the particle detection efficiency and the signal to noise ratio. In order to measure these parameters under the real experimental conditions and to validate the SSD module design, a series of beam tests has been carried out at CERN Proton Synchrotron. The beam tests had to provide a definite answer whether the module performance meets the requirements of the ALICE experiment and hence whether the mass production of the modules could be started. Two beam tests took place in June and September 2003 at CERN in the PS East target hall. In the June 2003 test a single module without a possibility of particle tracking was studied, and in September 2003 a telescope of four modules was used. The results of the September 2003 beam test will be discussed in this chapter.

4.2 Experimental Setup

The PS accelerator delivered a pion beam with a momentum of 7 GeV/c, in 0.6 s long spills repeating every 16 s. Each spill contained about 5000 particles. The scheme of the beam test setup is shown in the figure 4.1. Four module prototypes were arranged in a telescope with 3 cm spacing between the modules. The modules were shielded from the ambient light by a thin aluminium box. The beam spot had an elliptic shape with the width of 7 cm and height of 4 cm, and was aligned with the sensor's center, covering the entire sensor area. The modules used in the beam test were produced using silicon sensors from two different manufacturers (modules 1 and 2 with Canberra sensors and 3 and 4

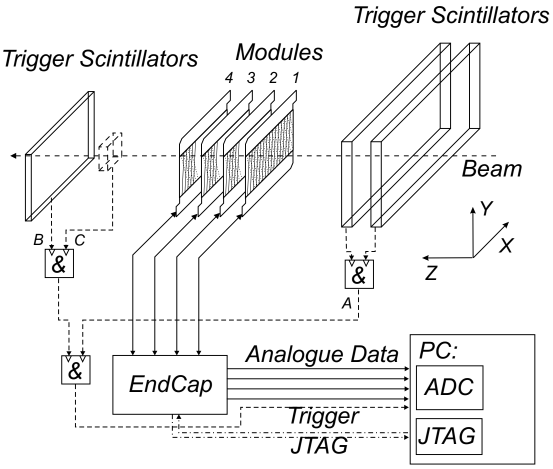

Figure 4.1: The schematic setup layout. A,B and C are the trigger scintillators.

with ITC sensors) and were the first modules corresponding to the final design.

Each hybrid of four SSD modules was connected to the EndCap prototype board [7] – the readout board that buffers the analogue and digital output signals from the HAL25 front-end readout chips to the DAQ system and decouples them from the sensor bias voltage. The EndCap prototype boards used the same dedicated ASICs (ALABUF and ALCAPONE) as the final design EndCap boards, but the boards themselves were made using traditional PCB technology, thus had a much bigger size. A CAEN power supply unit was used to power the front-end electronics, EndCap and to bias the sensors.

The EndCap boards were connected with a 30 m long cables to a DAQ system consisting of a control board and a PC containing an ADC[1] card. The ADC card had four 12-bit analogue acquisition channels with a sampling frequency set to 10 MHz, the maximum trigger rate the system could accept was about 100 Hz. Due to this limitation only 60 events per single spill could be acquired. The stream of digitized analogue data coming from the ADC was stored on disk in a binary format. Every event contained 1536×4 samples saved as 16-bit numbers, taking thus 12 kbytes of the disk space. The preliminary hit reconstruction was performed in between the spills and the information on the hit locations and deposited charge was displayed online for monitoring purposes. A dedicated unit was used to supply JTAG commands from PC to the EndCap and HAL25 chips.

The trigger signals were produced using four plastic scintillators (see Fig.4.1). Two large scintillators of a size 20×25 cm^2 were located upstream in the beam next to each other and were put in the coincidence to produce the trigger “A”. Another scintillator of a size 8×5 cm^2 (slightly bigger than the sensor size) was

---

[1] ADC DAS 4020/12 card, for full specifications see www.measurementcomputing.com

located downstream behind the modules and produced the trigger "B". Triggers "A" and "B" were again put in the coincidence to produce a readout trigger. Another small scintillator roughly $\frac{1}{6}$ of the sensor size produced trigger "C" and if used in the coincidence with "A" and "B" allowed to select a fraction of the sensor area for dedicated studies.

4.3 Data analysis

4.3.1 Raw data: pedestals, noise and common mode shift

All the sensor strips are sequentially read out by the front-end electronics and the analogue information is transmitted through a 30 meters long cable to the ADC. The data sampled by the ADC (the *raw data*) is stored on disk. The analogue information which represents the charge read out from the detector strips, can be described as a sum of several independent components:

$$ADC(i,k)_{raw} = P(i) + CMS(j,k) + S(i,k) + N(i,k) \tag{4.1}$$

where $ADC(i,k)_{raw}$ is the signal read out from the strip number i in the event k; $P(i)$ is the *pedestal* of strip i; $CMS(j,k)$ is the *common mode shift* of the chip j in the event k; $S(i,k)$ is the physical signal due to the charge deposited by the beam particles and collected by the strip i in the event k; and $N(i,k)$ is the random (noise) signal collected by strip i in the same event.

Compensation for the signal distortion in the cable

When the analogue signal is transmitted to the ADC through a long cable, it undergoes some distortion due to the losses in the cable. The losses arise from resistance in the conductors and leakage through the dielectric. A step-like voltage change at the chip output from the level of i-th channel V_i to the level of the next channel V_{i+1} (see Fig. 4.2), arrives at the ADC input softened to a slow rise. The shape of the signal front is described by the function [22]:

$$V(t) = \begin{cases} V_i & t = t_i \\ V_i + (V_{i+1} - V_i) \cdot \mathrm{erfc}(\frac{1}{2\sqrt{t/\tau_0}}) & t_i < t < t_{i+1} \end{cases} \tag{4.2}$$

where

$$\tau_0 = \frac{(x\alpha)^2}{\pi f} \tag{4.3}$$

with x: length of the cable; α: attenuation constant; f: frequency at which α is evaluated. The parameter τ_0 is the time it takes to reach a middle between the voltage levels V_i and V_{i+1}. The complementary error function $\mathrm{erfc}(x)$ is defined as

$$\mathrm{erfc}(x) = 1 - \frac{2}{\sqrt{\pi}} \int_0^x \exp(-u^2)\mathrm{d}u.$$

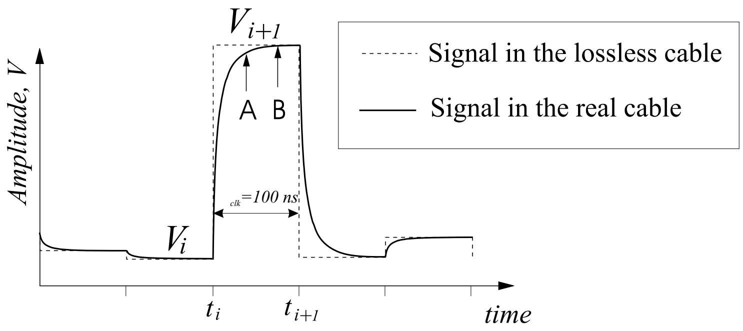

Figure 4.2: The analogue signal as it arrives at the ADC. If the sampling takes place at point A, then the sampled signal will include a fraction of the signal in the previous channel. Choosing the sampling point closer to the end of the readout clock cycle (near the point B) helps to solve the problem if the rise time τ_0 is much smaller than the readout clock period τ_{clk}.

For practical reasons the sampling point of the ADC is usually chosen to be at about $\frac{2}{3}$ of the readout clock cycle τ_{clk} shown as the point (B) on the Fig. 4.2. If $\tau_0 \ll \tau_{clk}$ then the ADC samples the correct voltage level V_{i+1}. If the sampling point is chosen too close to the pulse front (point A of Fig.4.2) then the sampled signal will include a fraction of the voltage of the previous channel, introducing thus an asymmetric left-to-right coupling in the readout channels.

In the present beam test the sampling point was adjusted to be close to $\frac{2}{3}\tau_{clk}$ but the condition $\tau_0 \ll \tau_{clk}$ was not completely fulfilled because of the large length x of the cable and hence large τ_0 (see eq. 4.3). Although when looking at the signal with an oscilloscope, one could see a reasonably flat top of the pulse, a small $\sim 5\%$ pickup of the signal from the previous channel was found during the offline analysis. Therefore this pickup had to be compensated by subtracting from the raw ADC signal a fraction f of the signal difference between the adjacent channels:

$$ADC(i,k) = ADC(i,k)_{raw} - k \cdot [ADC(i,k)_{raw} - ADC(i-1,k)_{raw}] \quad (4.4)$$

where $f = 0.048$, i is the strip number and k – the event number. Trimming the data in this way restores the original left-to-right symmetry of the signals and below only the trimmed data will be meant when speaking about the strip signals.

Simple Case: No Beam

First, let's consider for simplicity the case when no beam is present, i.e. $S(i,k) = 0$. The *pedestal* $P(i)$ is the expectation value of the (trimmed) analogue data from the strip i, it can be estimated as the mean signal value of the strip i taken over a significantly large number of events n:

$$P(i) = \frac{1}{n}\sum_{k=1}^{n} ADC(i,k) \tag{4.5}$$

The random deviation of the signal from the pedestal in every event is a sum of the of the common mode shift and the strip noise charge: $ADC(i,k) - P(i) = CMS(j,k) + N(i,k)$. By definition it has zero expectation value:

$$\frac{1}{n}\sum_{k=1}^{n}(CMS(j,k) + N(i,k)) = 0 \tag{4.6}$$

After subtracting the pedestals from the signal, the *common mode shift* for the chip j in the event k is determined as the average residue signal of the strips from this chip:

$$CMS(j,k) = \frac{1}{128}\sum_{i\in\text{ chip } j} ADC(i,k) - P(i) \tag{4.7}$$

Due to (4.5) it also has zero expectation value. The pure strip noise signal $N(i,k)$ is obtained by subtracting the pedestals and the common mode shift from the strip signal. The strip noise σ_i is determined as a standard deviation of $N(i,k)$:

$$\sigma_i^2 = \frac{1}{n}\sum_{k=1}^{n} N(i,k)^2 = \frac{1}{n}\sum_{k=1}^{n}(ADC(i,k) - P(i) - CMS(j,k))^2 \tag{4.8}$$

One may also consider a total noise - the sum of the common mode and the individual strip constituents:

$$\sigma_{i_{Tot}}^2 = \frac{1}{n}\sum_{k=1}^{n}(N(i,k) + CMS(j,k))^2 = \frac{1}{n}\sum_{k=1}^{n}(ADC(i,k) - P(i))^2 \tag{4.9}$$

This value has to be considered if it is not possible to estimate the common mode shift, for example if one uses zero suppression[2] of data.
The *common mode noise* of the chip j is the standard deviation of the common mode shift:

$$\sigma_{j,\,CMN}^2 = \frac{1}{n}\sum_{k=1}^{n}(CMS(j,k))^2 \tag{4.10}$$

The separation of the noise into the common mode (correlated) part and the strip (uncorrelated) part is caused by the distinction between the sources feeding these two components. The individual strip noise is caused by the electronic noise in the preamplifiers of the HAL25 chip which reads out the strips and/or

---

[2] **Zero suppression** - a method of compressing the data stream by keeping only the values higher than a certain threshold, discarding thus the data from strips containing no signals.

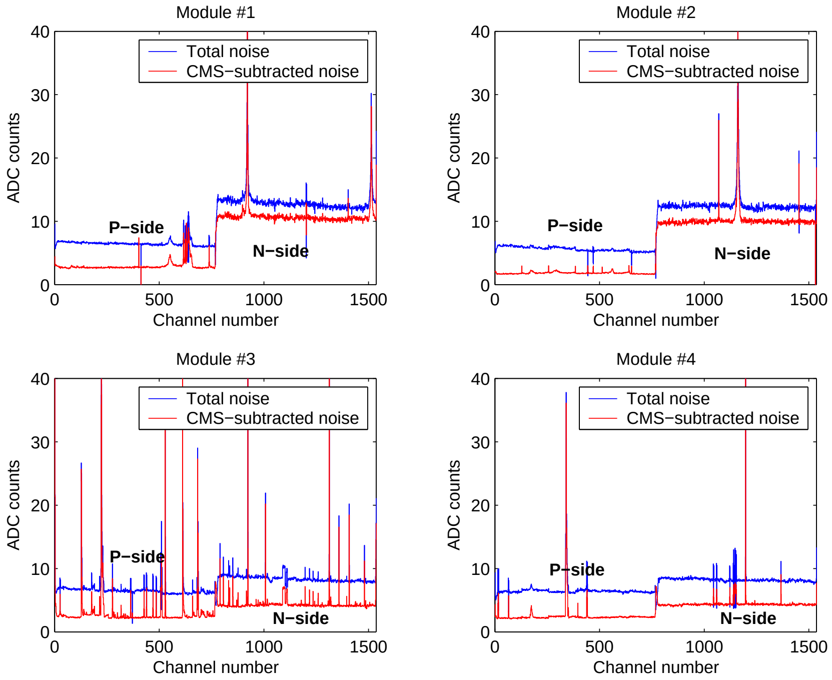

Figure 4.3: Noise of all four modules measured with no beam, with and without common mode subtraction. P-side channels are followed by N-side channels.

by the thermally generated charge that the strips collect from the silicon sensor. Among the sources that may in general contribute to the common mode noise one can name: the low-frequency electrostatic pickup from the outside world (the "antenna effect"), the noise of the bias voltage feeding the HAL25 chips and the noise of the sensor bias voltage. In our particular case the common mode noise had an amplitude comparable to the individual strip noise (see Fig.4.3) and thus it had to be treated carefully.

Several observations provide a hint on the sources of the common mode noise in the present setup. There was a slight correlation between the position of the chip on the hybrid and the common mode noise, as seen from Fig.4.4. The trend is that the chips connected "earlier" to the hybrid power supply lines see more common mode noise than the chips connected after them. The total difference in noise between F-chip and L-chip of the same hybrid is about 10%, what indicates that at least a part of the common mode noise is accounted for by the noise in the hybrid power supply lines.

A high positive correlation (≈ 0.96) between the common mode noise of the chips from the same hybrid was observed, together with the strong negative correlation (≈ -0.85) with the chips from the hybrid reading the other side of the sensor (see Fig.4.5). Also, some channels that are not connected to the

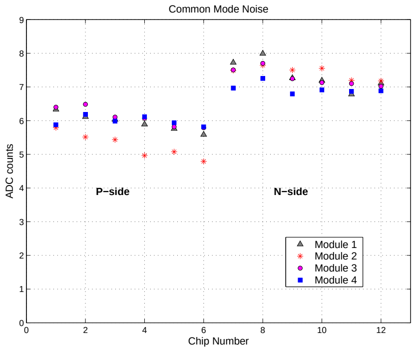

Figure 4.4: Chip common mode noise. There is a clear dependence on the chip location on the hybrid

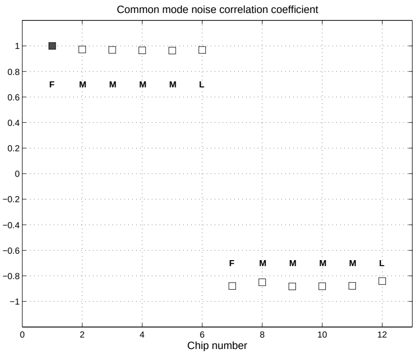

Figure 4.5: Correlation coefficient of the common mode noise of F-chip on P-side vs. other chips on the same module.

sensor strips (due to the bonding failure) show much less noise level practically without a common mode component. Such a behavior can be best explained by the noise of the sensor bias voltage.

Real Case: Beam "On" and Hit Suppression

Now, let's consider the case when the beam is present and $S(i,k) \neq 0$. Both equations (4.5) and (4.8) would give biased estimates of the noise and pedestals, if the summation is done over all the events including the events with a physical signal (i.e. *hit charge*) in the strip i (*fired strip*). The following procedure was applied to reject the fired strips.

First, the biased pedestals $P_B(i)$ for every strip were calculated according to (4.5) summing over the first 1000 events. Due to the low occupancy (usually one hit per event) the chance of having a hit in the particular strip is of the order 10^{-3} and with the mean deposited charge $\langle S \rangle \approx 200$ ADC counts (as will be seen from the Chap.4.3.5), the modification of the pedestal is roughly $200 \cdot 10^{-3} = 0.2$ ADC counts. The biased noise $\sigma_{i_{Tot\,B}}$ is calculated according to (4.9) using the biased pedestals $P_B(i)$ instead of the real $P(i)$. The biased noise $\sigma_{i_{Tot\,B}}$ can be estimated as $\sigma_{i_{Tot\,B}} \approx \sqrt{\sigma^2_{i_{Tot}} + 10^{-3} \cdot 200^2} \approx \sqrt{36+40} \approx 8.7$ ADC counts compared to the unbiased estimate of approximately 6 ADC counts.

Then the unbiased pedestals and noise were calculated using the same equations (4.5) and (4.8) but now skipping all the events where the deviation from the pedestals for the trip i exceeded $6\sigma_{i_{Tot\,B}}$ threshold

$$ADC(i,k) - P_B(i) \geq 6 \cdot \sigma_{i_{Tot\,B}} \tag{4.11}$$

For the common mode shift calculation, the summation in equation (4.7) excluded the channels where the deviation from the pedestals exceeded $3\sigma_{Tot}$

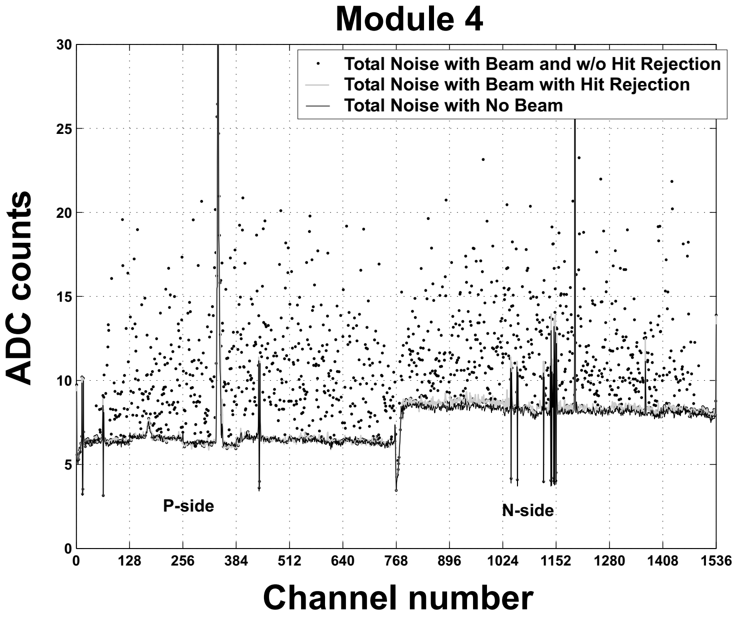

Figure 4.6: Comparison of the module 4 “Total noise” taken with beam “on” and “off”. The hit rejection algorithm efficiently restores the noise to it’s original level.

threshold in order to exclude the signals related to the particle hits. For the same reason the strips with the noise more than 40 ADC counts were also excluded.

The noise calculated with the hit suppression lies very closely to the noise measured with no beam, as the figure 4.6 demonstrates. However, one can not directly use the pedestals measured without the beam for the entire data analysis because the pedestals have a sizable drift and have to be continuously updated. Thus the pedestals measured with the first 1000 events of the particle run were taken as initial ones and were continuously updated after every event during the run using a “sliding window method”:

$$P(i,k) = \frac{N_{win}-1}{N_{win}}P(i,k-1) + \frac{1}{N_{win}}ADC(i,k) \tag{4.12}$$

where N_{win} is the “window width”. The update was again done only for the non-fired strips, where the collected charge was below $3\sigma_i$ threshold. The window width was chosen to be 200 events in order to trace the slow changes in the pedestals but at the same time give little statistical deviations.

4.3.2 Cluster Finding Algorithm

After subtracting the pedestals and common mode shift from the strip data, one obtains a sum of a noise charge and possibly a particle-induced charge collected by the strips. This charge $q(i,k) = S(i,k) + N(i,k)$ is then compared with a $3\sigma_i$ noise threshold in order to find the fired strips. A group of contiguous fired strips is combined into a *cluster*. If a particle passes through a disconnected strip, then the induced charge is collected by the strips next to it, leading to a cluster with an interruption inside. For this reason the disconnected strips, that collect no charge by themselves, are included in the cluster if they are in between two other fired strips. The cluster charge is determined as:

$$Q_{Cl} = \sum_i q(i,k) \tag{4.13}$$

where the summation is done over the strips included in the cluster. The cluster noise is measured as a quadratic sum of the noise of the cluster strips including the noise correlations between the readout channels due to the interstrip capacitance. The cluster noise reads:

$$N_{Cl} = \sqrt{\sum_{ij} \rho_{ij} \cdot \sigma_i \sigma_j} \tag{4.14}$$

The noise correlation factor ρ_{ij} between strips i and j depends on the details of design of the detector structure and is different for P and N sides of the sensor. A positive noise correlation would further increase the cluster noise, whereas a negative correlation leads to partial compensation of the noise charge and brings the cluster noise down. A theoretical treatment of this subject [20] based on the simplified detector model results in the negative noise correlations that help to keep the cluster noise close to a single-strip noise, but in practice both positive and negative correlations occur. The actual noise correlation values for the modules used in the beam test are shown on figure 4.7. One can notice a sizable (≈ 0.3) positive correlation between the adjacent strips on the N-side and different overall patterns for Canberra (1,2) and ITC (3,4) sensors. The noise correlation increases the two-strip cluster noise roughly by 5% on the P-side and by 10% on the N-side if compared to the case with no correlations.

The clusters with $(Q/N)_{Clust} > 5$ are kept for further analysis, the threshold assures that the chance of having a fake cluster (i.e due to a noise charge) is definitely less than 1% per sensor side per event.

4.3.3 Cluster Size

When a charged particle crosses the detector, it creates a column of electron and hole pairs along its trajectory. The electric field present inside the silicon bulk which is created by applying the bias voltage to the sensor, pulls apart the created electron and hole pairs. The motion of this charge induces a signal on one or more adjacent sensor strips. If the number of strips in the cluster is

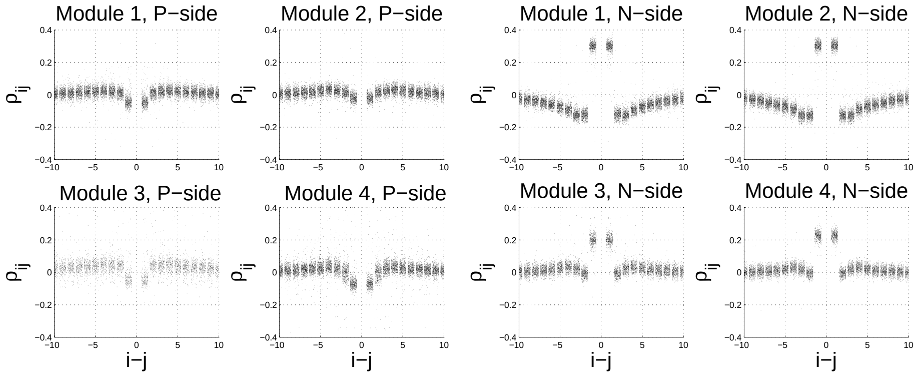

Figure 4.7: The noise correlation coefficients ρ_{ij} between the strips i and j on P and N sides plotted versus $i - j$. A random value in the range $[-0.4 \quad 0.4]$ is added to the abscissa of each point to prevent the points from overlapping.

more than one, then one can determine the particle impact point more precisely by measuring the relative charge collected by each of the fired strips and using some model of charge sharing between the strips. The number of fired strips depends on a number of factors, such as: the strip pitch, track inclination, carrier diffusion, capacitive coupling between the neighboring strips, channel noise. For tracks inclined in the plane perpendicular to the strip direction, the charge is spread over a few strips because the track crosses the volume "seen" by several trips. At normal incidence, which will only be considered here, the track crosses the volume from which the charge is collected by one or two strips at most. The spread of the charge in this case is mainly governed by the diffusion process, which in fact, makes fuzzy the borders of the volumes from which the individual strips collect the charge. The width of the charge cloud σ_{diff} as it arrives at the read-out plane, can be roughly estimated from the carrier mobility and the drift time:

$$\sigma_{\text{diff}} = \sqrt{2\frac{kT}{e}\mu t} \approx \sqrt{2\frac{kT}{e}\frac{L^2}{V_{\text{bias}}}} \approx 10\ \mu\text{m} \qquad (4.15)$$

where L is the sensor thickness (see also Fig.3.20a at p.49). This is an order of magnitude smaller than the strip pitch (95 μm). This means that if the track is crossing the detector normally to its surface and it is passing through the region far away from the border between two strips (i.e., it passes close to the centerline of the strip), then all the charge will be collected by one strip. The figure 4.8 demonstrates how the relative number of 1, 2 and $\geq$3-strip clusters depends on the position of the impact point with respect to the centerline of the strips. The strip centers are located at $u = 0$ and $u = 1$, so that the point $u = 0.5$ is located in between the strips. The impact point is predicted from a track reconstructed using the other 3 sensors in the telescope. The estimated error of the prediction of the impact point position is ≈ 0.1 pitch units for the

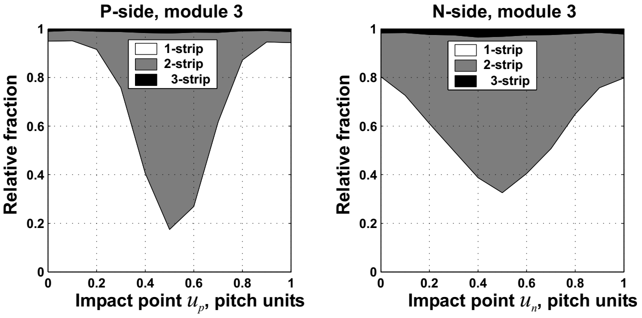

Figure 4.8: The stacked histogram of the relative number of clusters having 1, 2, 3 or more strips in the cluster, plotted versus the impact point. The impact point is predicted from the track reconstructed using the other 3 sensors of the telescope.

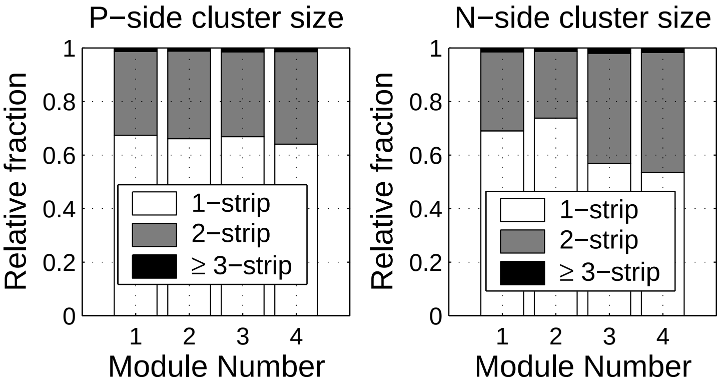

Figure 4.9: Cluster size histogram at normal incidence.

p-side and ≈ 0.2 pitch units on the n-side. This makes the dependence on the left picture (for the p-side) more pronounced compared to the right picture for the n-side. One can see that the probability of having a single-strip cluster is peaked at the centerline of the strip, and for the double-strip clusters – in between the strips. For this reason the spatial resolution one obtains using only the single-strip clusters should be smaller than the digital resolution of 27 μm one expects from a 95 μm strip pitch detector. The overall fractions of 1, 2 and $\geq$3-strip clusters for all four modules is shown on figure 4.9. A high strip noise seen on the n-side of modules 1 and 2 (see Fig.4.3) results in a larger percentage of single-strip clusters on the n-side of those modules. This happens because the high noise masks the charge collected due to carrier diffusion and capacitive coupling by the strips adjacent to the strip that collects most of the charge.

4.3.4 Gain Calibration

The strength of the particle-induced signal coming from each individual readout channel may vary from channel to channel because of slightly different gain of the electronic channels in the HAL25 chip or some signal loss in the bonds of the cable connecting the input of the chip to the sensor strips. It is therefore essential to have a gain calibration for each channel, in particular when studying the shape of the cluster charge distribution collected by the entire detector. One could use, for example, the most probable value of the strip charge as a measure of the strip gain, but the limited statistics ($\mathcal{O}(100)$ hits per strip) does not allow to make a reliable fit to the data. An ordinary mean value of the strip signal would not be an efficient estimator because it's sensitive to the outliers – a few events in the Landau tail that may significantly shift the mean value. As opposed to the mean, a median value of the strip charge is a robust estimate of an average strip signal. This value was used for the gain calibration. The signal selection was done as follows: for each strip only those signals were kept where the strip collected more than a 70% of the total cluster charge and provided that the cluster was the only one found on this sensor side in the event. This is done to exclude the signals appearing due to the charge sharing with a neighboring strips and to exclude the events with multiple hits or noise clusters. The distribution of the signals passing this criterion on the p-side of module 4 is shown in the figure 4.10. The vertical dashed line on this figure denotes the position of the median, it is slightly larger than the most probable value. The statistical error of the position of the median can be estimated using the interquartile range of the data. The interquartile range is the robust estimator of the dispersion of the data set, defined as the difference between two thresholds one of which cuts off the smallest 25% of the data and the other – the largest 25% of the data, so that the interval between these two thresholds holds the remaining 50% of the

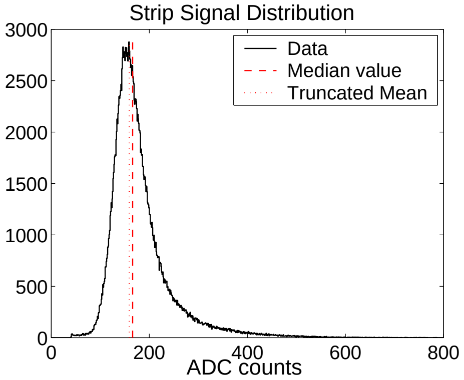

Figure 4.10: The histogram of the signal from the strips that collect more than 70% of the cluster charge in the events with one cluster per side. The median value and the truncated mean serve as robust estimates of the average signal.

data. For normally distributed data the interquartile range (i.q.r.) is related to the standard deviation σ as:

$$0.7413 \cdot (\text{i.q.r.}) = \sigma$$

The statistical uncertainty of the median value is then:

$$\sigma_{\text{stat}} = 0.7413 \cdot (\text{i.q.r.})/\sqrt{n} \tag{4.16}$$

where n is the size of the entire data set.

The obtained statistical uncertainty is of the order of 1% in the center of the sensors, where the beam density and the statistics were the highest (≈ 600 events per strip).

The plot of the median gain estimates for all the channels is shown in the figure 4.11. One can notice that there is a small but distinctive gain difference between the channels that belong to the neighboring chips. The overall dispersion of the strip gain for every sensor side is of the order of $3 \div 4\%$ and is several times larger than the statistical uncertainty of the gain determination. The gain calibration coefficients were calculated as the mean gain of the hybrid divided by the channel gain. Only the channels with statistics more than 100 entries were used to ensure the small statistical uncertainty, for the other channels the calibration factor of unity was assumed.

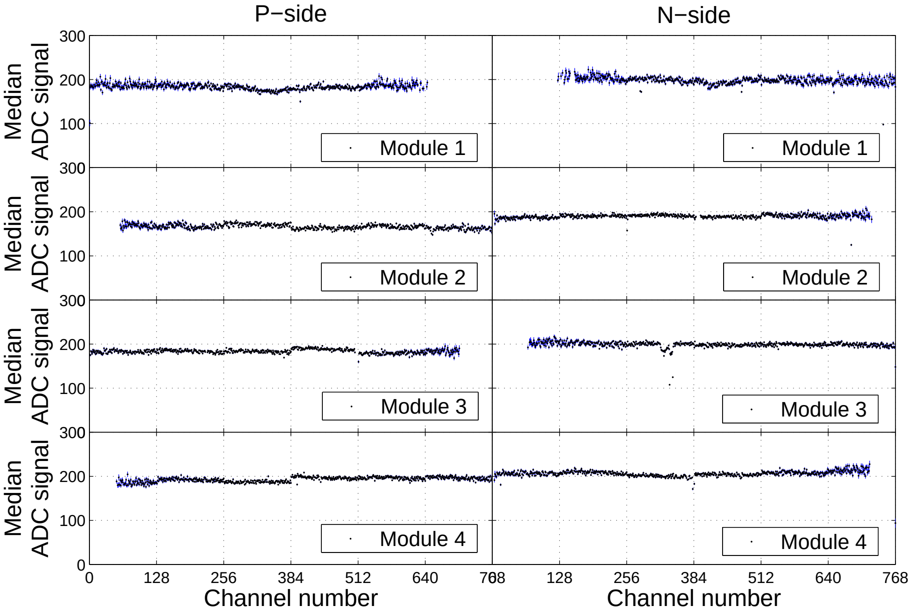

Figure 4.11: Median strip signal used as a gain estimate. Only the data for the channels with a significant statistics is shown.

4.3.5 Cluster Charge

Single-side Cluster Charge

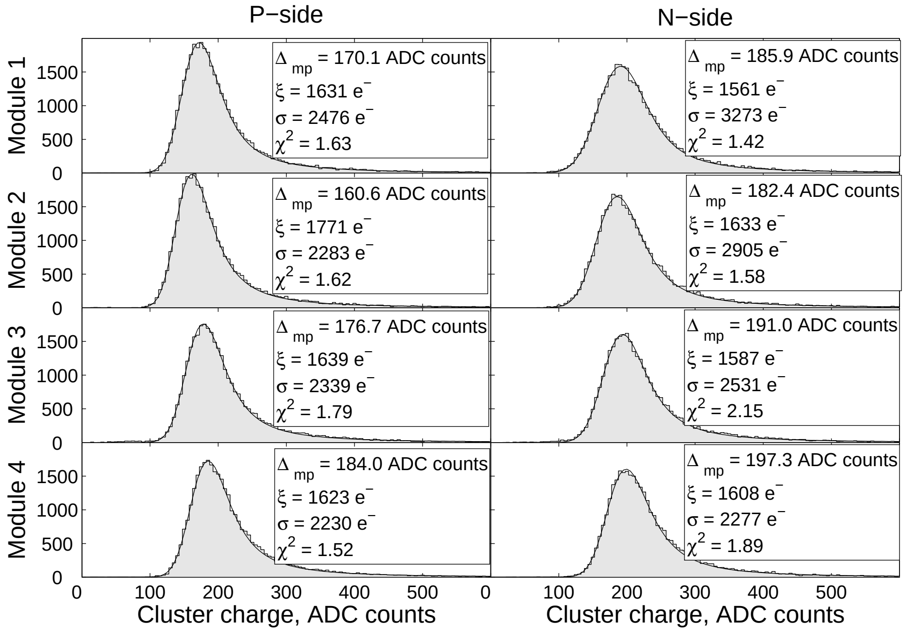

Figure 4.12: The distribution of the cluster charge fitted with a Landau function folded with a Gaussian function. The fit parameter Δ_{mp} is the most probable energy loss assumed to be equal to 84 keV or 23140 e^- and used for calibration of the ADC scale. The parameter ξ is a measure of FWHM of Landau distribution and σ is the width of the Gaussian function.

The histograms of the cluster charge Q_{Cl} collected by the p-side and the n-side of each of the four modules are shown in the figure 4.12. The histograms include only the clusters that originate from the particle hits i.e., clusters that have a corresponding cluster of the opposite polarity on the opposite sensor side. This is necessary to reject the noise clusters . Also those events were excluded where more than one hit per sensor was found. For convenience of visualization, the polarity of the n-side clusters is inverted in the figure.

The histograms are fitted with a Landau function [23] convoluted with a Gaussian function:

$$f(x, \Delta) = 1/\sqrt{2\pi\sigma^2} \int_{-\infty}^{+\infty} f_L(x, \Delta') \times \exp[-(\Delta - \Delta')^2/2\sigma^2] \mathrm{d}\Delta' \tag{4.17}$$

where Δ is the actual energy loss when a distance x is traversed, and $f_L(x, \Delta)$ is the Landau distribution function. The Landau function is given by:

$$f_L(x, \Delta) = (1/\xi)\phi(\lambda)$$

where the function $\phi(\lambda)$ is a universal function of a dimensionless variable λ:

$$\lambda = [\Delta - (\Delta_{\text{mp}} - \xi\lambda_0)]/\xi.$$

The parameter Δ_{mp} is the most probable energy loss in the traversed layer x, $\lambda_0 = -0.225$ is the value for which $\phi(\lambda)$ is a maximum. The parameter ξ is defined as:

$$\xi = (2\pi z^2 e^4/m_e c^2 \beta^2) N_A Z x \rho / A$$

where N_A is the Avogadro number, m_e and e are the electron mass and charge, respectively, z is the charge of the incident particle, Z, A, and ρ are the atomic number, atomic weight, and density of the material. The FWHM of the Landau distribution is given by 4.02ξ. For 300 μm silicon $\xi = 5.5 \pm 0.3$ keV [26] and assuming that it takes 3.63 eV to create an electron-hole pair in silicon [17], ξ can be expressed in electron units as $\xi = 1515 \pm 82\ e^-$.

The convolution with a Gaussian function with a fit parameter σ is introduced for two reasons. The first reason is the finite charge measurement resolution of the detector. This is due to the noise in readout electronics which adds a noise charge to the signal and also masks, due to the noise threshold, a fraction of the cluster charge when it is shared among several strips. The second reason is the broadening of the energy loss distribution for thin absorbers as compared to the original Landau distribution because of the resonance collisions with electrons from the inner shells (mostly from the K-shell) of Si atoms [24]. For silicon planes of 300 μm the shape of the energy loss distribution can be well approximated by the Landau function convoluted with a Gaussian function [25, 26]. The fit parameter σ^2 is then: $\sigma^2 = \sigma^2_{\text{noise}} + \sigma^2_K$ where σ_{noise} is due to the electronics noise and σ_K is due to the broadening of the energy loss distribution, $\sigma_K = 5.75 \pm 0.5$ keV or $1584 \pm 138\ e^-$ for 300 μm Si [25].

The fit curve was computed by numerical integration of the eq. (4.17). The Landau function $\phi(\lambda)$ was calculated using the adapted CERNLIB routine DENLAN. The three fit parameters Δ_{mp}, ξ and σ were treated independently during the fitting procedure. The calibration of the ADC scale was performed using a value of 84.0 keV [26] for the most probable energy loss Δ_{mp}, or expressing it in the number of created electron-hole pairs, $\Delta_{\text{mp}} = 23140\ e^-$. The values of the parameter ξ obtained from the fit (see text labels of the Fig. 4.12) are close to those found in the literature [26].

One can also obtain an estimate of the electronics noise contribution σ_{noise} to the fit parameter σ:

$$\sigma^2_{\text{noise}} = \sigma^2 - \sigma^2_K. \tag{4.18}$$

The estimates of σ_{noise} for all the four modules obtained using eq.(4.18) are listed in the table 4.1. This can be compared to the lower bound of the cluster charge measurement resolution calculated only using the strip noise information. If we assume that the measurement error of the cluster charge Q_i in the event i is given by the cluster noise $(N_{Cl})_i$ then the overall charge resolution is given by the r.m.s. cluster noise:

$$\sigma_Q^2 = \frac{1}{n}\sum_{i=1}^{n}(N_{Cl})_i^2 \tag{4.19}$$

where the summation is done over all the events included in the histogram. One can see that the lower bound underestimates σ_{noise} obtained from the fit by 2-3 times. The reason for such a big discrepancy is not entirely clear.

Table 4.1: The estimate of the electronics noise σ_{noise} obtained from the fit parameter σ, see eq(4.18), compared to the r.m.s. cluster noise $\langle N_{Cl}^2\rangle^{1/2}$.

Module number	Estimate of the electronics noise σ_{noise}, e^-		R.M.S. cluster noise $\langle N_{Cl}^2\rangle^{\frac{1}{2}}$	
	p-side	n-side	p-side	n-side
1	1195	2772	465	1606
2	1348	2486	477	1544
3	935	1602	399	713
4	1000	1290	364	683

Charge matching

A good matching between the cluster charge collected by p- and n-sides is essential for the hit reconstruction in the high-multiplicity environment. The figure 4.13 shows the correlation of the p-side cluster charge Q_p and the n-side cluster charge Q_n obtained in the single-particle events. The quality of the charge matching can be characterized by the r.m.s. of the difference between Q_p and Q_n:

$$\sigma_{\text{corr}}^2 = \frac{1}{n}\sum_{i=1}^{n}[(Q_p)_i - (Q_n)_i]^2 \tag{4.20}$$

These values are given in the figure 4.13. As in the case of the single-side charge resolution, the theoretical lower bound of σ_{corr} can be obtained from the detector strip noise data as:

$$(\sigma_{\text{corr}}^2)_{\text{th}} = \frac{1}{n}\sum_{i=1}^{n}[(N_{Cl,p})_i^2 + (N_{Cl,n})_i^2] \tag{4.21}$$

where N_{Cl} is the cluster noise and the summation is done over all the considered events. The noise estimates and the actual σ_{corr} are listed in the table 4.2. The actual σ_{corr} obtained from the data are 1.2-1.7 times bigger than the cluster noise estimates. This can be attributed to the occasional loss of a fraction of the cluster charge in the cases when the charge is shared between two strips. If the most of the charge goes to one strip, then the fraction of the signal collected by the neighboring strip is taken into account only if it exceeds S/N cut, which leads to an underestimation of the cluster charge in this case (unless all the signal really goes to one strip). Since this happens on p- and n-sides independently, it increases the spreading between p- and n-side charge.

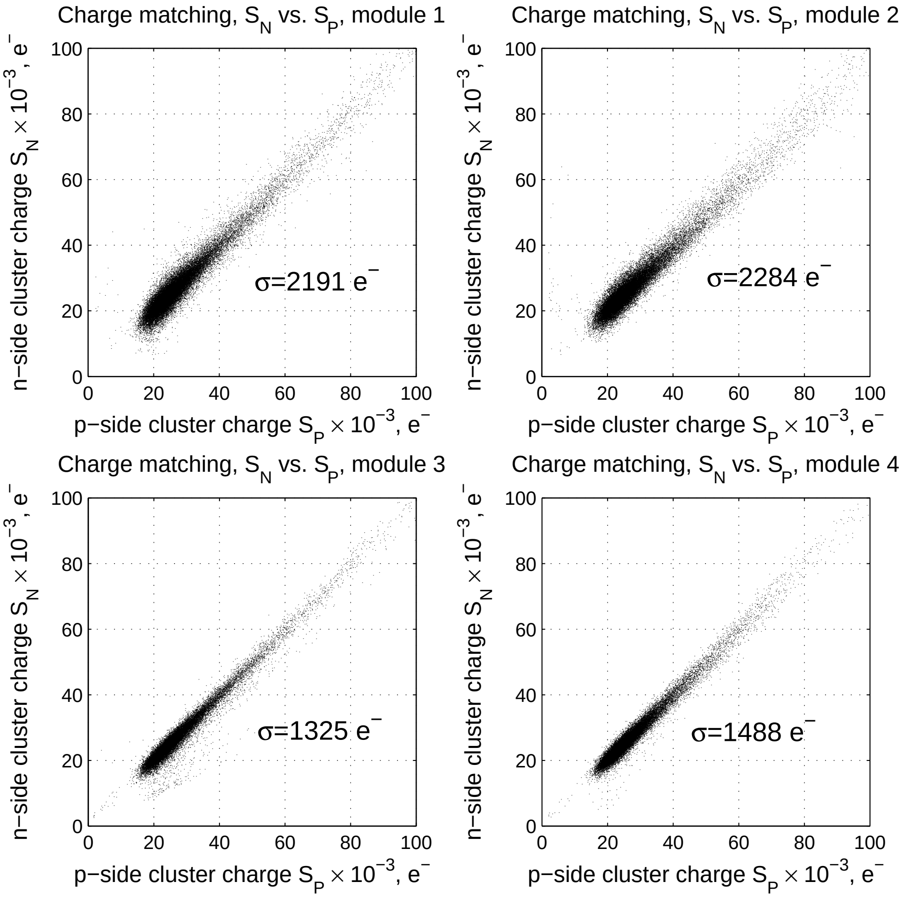

Figure 4.13: Correlation between the p- and n-side cluster charge.

Table 4.2: R.M.S. spread of $Q_p - Q_n$ cluster charge, compared to the estimate from the cluster noise N_{Cl}.

Module number	R.M.S. of $Q_p - Q_n, e^-$	
	Measured	Estimated
1	2092	1671
2	2119	1616
3	1214	817
4	1291	774

4.3.6 Signal-to-Noise ratio

The signal-to-noise ratio is defined as the most probable value of the ratio Q_{Cl}/N_{mean}, where Q_{Cl} is the cluster charge and N_{mean} is the mean noise of

Table 4.3: Median strip noise and the signal-to-noise ratio of the modules.

Module number	Median strip noise, e^-		S/N ratio	
	p-side	n-side	p-side	n-side
1	435	1487	57	18
2	435	1415	56	18
3	354	559	70	45
4	331	575	75	43

the cluster strips. This parameter is frequently used to characterize the gross performance of the detector or when comparing one detector to the other, since it's independent on the cluster size and details of the detector structure. The histogram of Q_{Cl}/N_{mean} for all four modules is shown on figure 4.14 and summarized in the table 4.3. A relatively low S/N ratio on the n-side of the modules 1 and 2 is due to roughly three times higher noise on the n-side of these modules compared to the n-side noise of the other two modules.

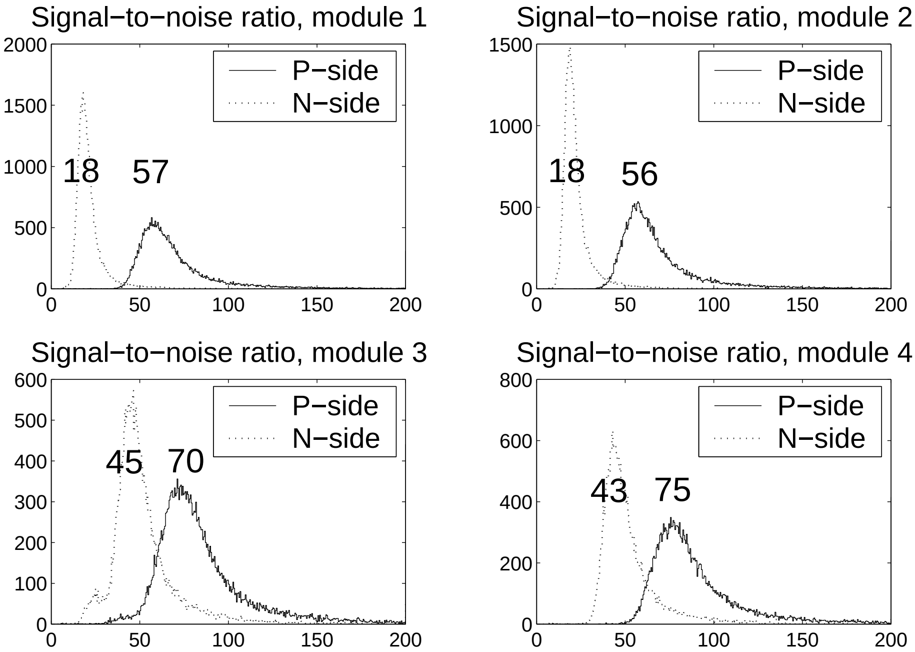

Figure 4.14: Histogram of the signal-to-noise ratio: the cluster charge Q_{Cl} divided by the mean strip noise N_{mean} of the strips in the cluster. The numbers on the plots show the most probable values of the ratios.

4.3.7 Hit Position Reconstruction

The reconstruction of the two-dimensional coordinates of the particle hit is performed using the information about the collected charge from both sensor sides. The first step of the reconstruction is to determine the position of the single-side hit clusters in the direction perpendicular to the strip orientation. The next step is to associate the hits found on both sensor sides into pairs in order to determine the cartesian hit coordinates. The reconstruction of the single-side hit position is always done with a measurement error which has a statistical and systematic components. The statistical component comes from the electronic noise and the fluctuation of the charge deposition profile. The systematic error is introduced by the hit position finding method itself. We will discuss several most commonly used position finding methods.

Digital Method

In this method the cluster coordinate is assigned to the coordinate of the center of the fired strip which collects the largest charge among the fired strips in the cluster. This method is de-facto the most frequently used for the current detectors because of the large number of clusters with only one fired strip, see figure 4.9. The theoretical spatial resolution this method can give is $\sigma = s/\sqrt{12}$, where s is a strip pitch. For $s = 95\ \mu m$, the expected resolution is $\sigma \approx 27\ \mu m$. However, the actual resolution obtained with this method, if it is applied to the single-strip clusters only, is somewhat smaller because the clusters are more likely to have only one strip if the particle traverses the detector close to the strip center (see figure 4.8). The residuals given by the digital method are shown in the figure 4.15 for the p-side of one of the modules. The residual (on the p-side) is the distance between the position r_p of the found cluster and the track impact point $r_{p\mathrm{x}}$ obtained by the interpolation of the track defined by the other tree sensors of the telescope. In the figure 4.15 the solid-line histogram displays the residuals that are obtained only with the single-strip clusters. The spikes on the histogram come from the aliasing of the predicted track position: the fitted track may have only discrete orientations (and thus, impact points) if it is fitted to the points that have discrete locations, this is the case if the particle creates only single-strip clusters in all the reference detectors. The dashed histogram shows the residuals distribution in the case if the position of *all* the found clusters (not only single-strip clusters) is determined by the digital method. In that case the distribution should be rectangular stretching from -0.5 to +0.5 in pitch units, smeared with the track interpolation precision. In order to compare the width of the distributions shown in the figure, we use the interquartile range as a robust measure of the dispersion. For the dashed histogram i.q.r.=0.50 pitch units, as it is expected in theory, and for the solid histogram, i.q.r.=0.35 pitch units, which is 30% smaller.

The digital method introduces a systematic position reconstruction error equal to the distance from the particle track to the closest strip. Therefore, further refinements are possible for the clusters that consist of more than one

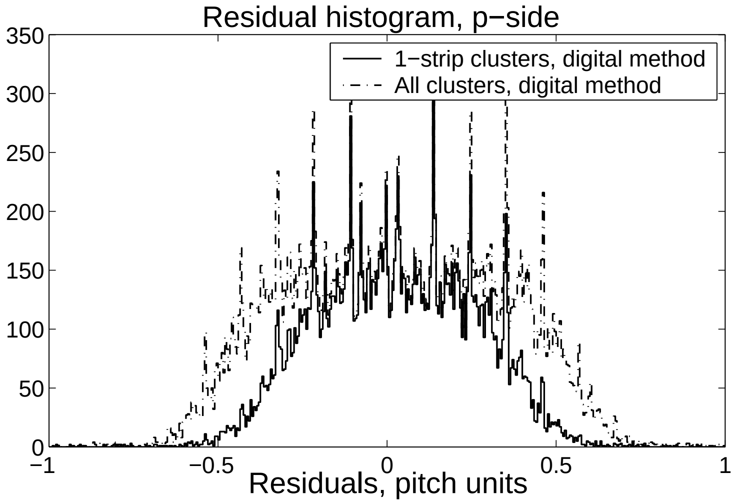

Figure 4.15: The residual distribution $r_p - r_{p\text{x}}$ given by the digital hit positioning method, when it is applied to all the found clusters or only to the single-strip clusters. The track impact points $r_{p\text{x}}$ are obtained with the tracks defined by the other 3 sensors in the telescope.

strip.

Center of Gravity (COG) method

This method allows to refine the cluster position if the cluster has two or more strips. The cluster position (in pitch units) is determined as a center of gravity of the fired strips weighted with the collected charge:

$$r^{\text{COG}} = \frac{\sum_i q(i,k) \cdot i}{\sum_i q(i,k)} \tag{4.22}$$

where i runs trough the indices of the strips included in the cluster. This method is robust and simple in the implementation.

The distribution of the hit residuals obtained with this method for the 2-strip clusters is shown in the figure 4.16. The interquartile range of this distribution is i.q.r.=0.44, which is an improvement compare to the digital method, which would give i.q.r.=0.82 if used only for the 2-strip clusters. Nevertheless the center of gravity positioning method still introduces a systematic error. This is demonstrated in the figure 4.17 which shows the dependence of the residuals on the track impact point. The systematic error is seen as a deviation of the average residual (solid line in the figure) from zero for a narrow range of the impact points. The systematic error is equal to zero exactly in between the strips because in that case both strips see an equal charge.

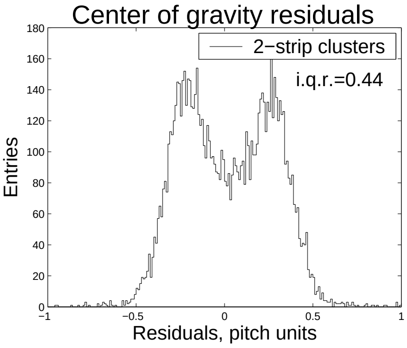

Figure 4.16: Histogram of the residuals $r_p^{\rm COG} - r_{p\rm x}$ obtained with a center-of-gravity method for 2-strip clusters on the p-side of module 2.

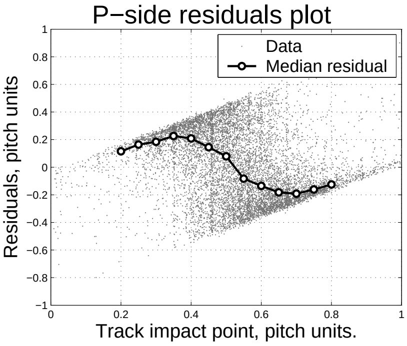

Figure 4.17: The residuals given by the COG cluster positioning method applied to 2-strip clusters, plotted versus the track impact point. The solid curve shows the median strip residual in the bins of the width 0.05 pitch units.

Linearized η method

In order to avoid the systematic error of position determination, one has to know how the charge is shared among the strips around the impact point and then use this dependence to predict the cluster position. For the 2-strip clusters which are the vast majority of the multi-strip clusters (see Fig. 4.9), the convenient way to describe the charge sharing is to use the charge sharing function η defined as:

$$\eta = \frac{Q_{\rm L}}{Q_{\rm L} + Q_{\rm R}} \tag{4.23}$$

where $Q_{\rm L}$ is the charge collected by the left strip and $Q_{\rm R}$ is collected by the right strip. The dependence of η on the extrapolated track impact point $r_{p\rm x}$ is shown in the figure 4.18. The solid line is the median track impact point $r_{p\rm x}$ in the bins of 0.1 η and shows the approximate dependence of η on $r_{p\rm x}$. One can see that the dependence $\eta = \eta(r_{p\rm x})$ is rather sharp and changes from $\eta = 1$ to $\eta = 0$ in a narrow range between $r_{p\rm x} = 0.4$ and $r_{p\rm x} = 0.6$. One can now use the interpolated curve to estimate the hit position with a better precision. For practical reasons, it is enough to approximate this curve with a straight line, shown in the figure as a dashed line. The distribution of the residuals obtained with the interpolated curve and the straight line fit are practically identical and the dispersions differ by less than 2%. The distribution of the residuals obtained with a center of gravity and the linearized η method are compared in the figure 4.19. The use of the linearized η method improves the interquartile range of the residuals distribution for 2-strip clusters from i.q.r.=0.44 given by the COG method to i.q.r.=0.14.

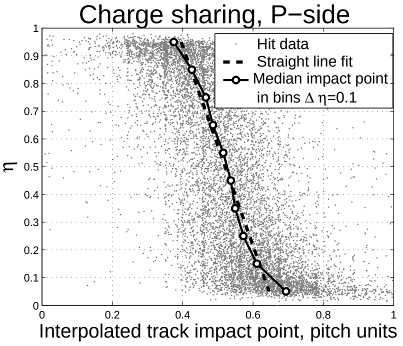

Figure 4.18: Charge sharing function η plotted vs. the impact point $r_{p\mathrm{x}}$ of the track defined by three other sensors.

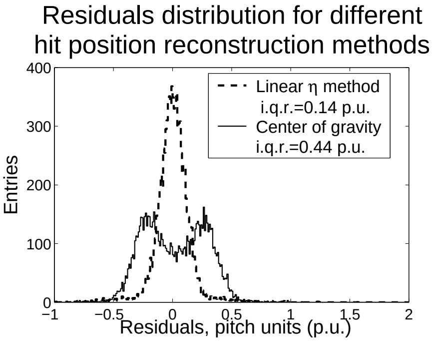

Figure 4.19: Residuals given by COG method and linear approximation of η method

The shape of the curve $\eta = \eta(r_{p\mathrm{x}})$ is defined by the initial spatial distribution and the diffusion of the electrons and holes created in the silicon bulk by the charged particle traversing the sensor. The initial distribution depends on the angle of incidence of the particle track, therefore before applying the η algorithm one has to know the track inclination and the η function for this inclination. In the present beam test the particle tracks we practically perpendicular to the detector surface, so that the η method could be applied straightaway, but in the ALICE experiment the magnetic field will bend the particle trajectories producing tracks with various inclination angles. Therefore the η method can only be applied to refine the impact points after the track has been preliminarily reconstructed using, for example, the center of gravity method. A comparison of various hit positioning methods for different angles of incidence is given in the reference [27].

Cartesian coordinates

The procedure of locating the cluster centers by either of the above described methods is done independently for both sensor sides. The next step is to determine the hit cartesian coordinates. If only one cluster per side is found, then the reconstruction of the hit position is trivial. Suppose r_p and r_n are the centers of mass of the clusters on p- and n-sides given by eq.(4.22) measured in the direction perpendicular to the strip direction. Then the hit cartesian coordinates (u, v) in the sensor frame of reference (see Fig. 4.20) are calculated according to the formula:

$$u = \frac{\tan\alpha_1}{\tan\alpha_1 + \tan\alpha_2}\left[s(n - 1 - r_n - r_p) + L_2\tan\alpha_2\right] + r_p s \qquad (4.24)$$

$$v = \frac{1}{\tan\alpha_1 + \tan\alpha_2}\left[s(n - 1 - r_p - r_n) + L_2\tan\alpha_2\right] \qquad (4.25)$$

where $s = 95\mu$m is the strip pitch, α_1=7.5 mrad, α_2=27.5 mrad – the strip tilt angles on p and n sides with respect to the sensor short edge, L_2=38 mm – the length of the sensor short edge, n=768 – the number of strips per side.

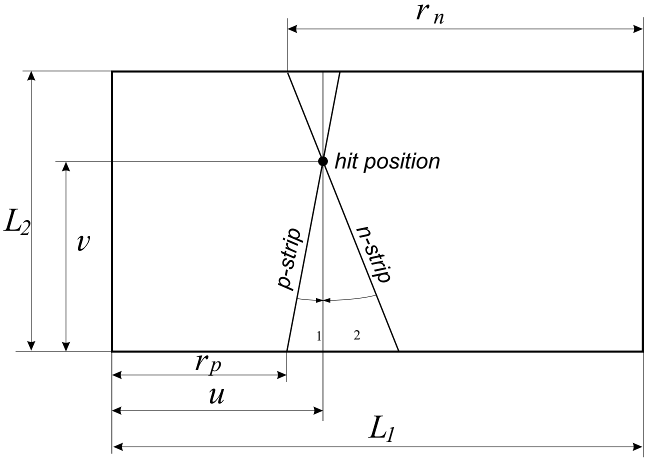

Figure 4.20: Translation of single-side hit coordinates (r_p, r_n) into cartesian coordinates (u, v) in the sensor frame .

If more than one particle hits the sensor at the same time (for example due to δ-electron production or nuclear reaction in the previous sensor of the telescope or due to the high intensity of the particle beam), then several clusters are detected on each side and the hit reconstruction is not so straightforward. Although the single-hit events were expected to dominate in the beamtest, a general reconstruction algorithm which could handle events with multiple ambiguous hits (see [8], p.193) was implemented. We will illustrate it's principle on a simple case when only two particles hit the sensor, and thus, two clusters per side are detected. First, consider the case when there is a large distance between the particles in the horizontal plane, see 4.21 a). Thanks to the special orientation of the strips which cross at low stereo angle, each strip "sees" only 15 strips on the opposite side. No ambiguity in associating the clusters on p- and n-sides into pairs will occur if the distance between the clusters at least on one of the sensor sides exceeds 15 pitch units (1425 μm). If two clusters on both sides are less than 15 strips away, then there can be two ways of combining them into pairs (Fig. 4.21 b)): either a true combination (1,2) or a ghost combination (3,4) can be selected. To solve this ambiguity one can use the information on the cluster charge and the fact that the charge deposition is a stochastic process, so that even the charge deposited by two similar particles of the same momentum is different. Since in double-sided strip detectors the cluster charge Q_P collected by the p-side and Q_N collected by the n-side are correlated, this correlation can be used to pick the true combination out of the two possible. For each of the four possible cluster pairs denoted as "1", "2", "3" and "4" in Fig. 4.21 b) one

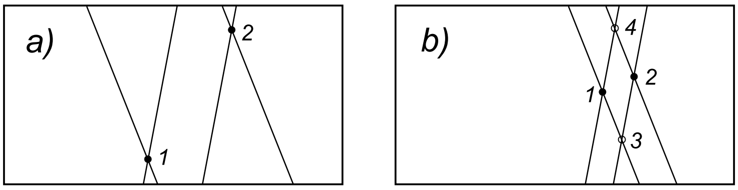

Figure 4.21: Two basic situations of hit locations: a) the distance between the clusters on one of the sides is larger than 15 strips, no ambiguity occurs; b) ambiguity occurs: either a true combination (1,2) of a ghost combination (3,4) can be selected. A situation when one of the ghost clusters is outside the sensor projection leads to no ambiguity.

constructs a χ^2_{pair} which is defined as:

$$\chi^2_{pair} = \frac{(Q_P - Q_N)^2}{\sigma^2_{corr}} \tag{4.26}$$

where σ_{corr} describes the quality of charge correlation and is defined as the r.m.s. of $Q_P - Q_N$ measured in single-particle events, (see section 4.3.5 for details). The value χ^2_{pair} is proportional to the distance on (Q_P, Q_N) plane from the point with coordinates $(Q_{P,i}, Q_{N,j})$ to the line of perfect match, see fig 4.22. For each combination of pairs (1,2) and (3,4) one constructs a χ^2_{comb}:

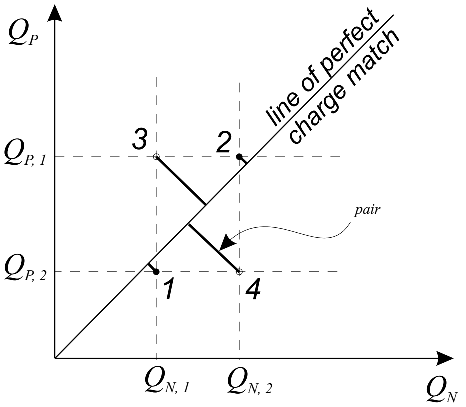

Figure 4.22: The choice between the true pair (1,2) and a ghost pair(3,4) is based on a charge matching quality factor χ^2_{comb}, proportional the sum of the distances between the pair of points (1,2) or (3,4) to the line of perfect charge match.

$$\chi^2_{comb,(1,2)} = \chi^2_{pair,1} + \chi^2_{pair,2} \tag{4.27}$$

$$\chi^2_{comb,(3,4)} = \chi^2_{pair,3} + \chi^2_{pair,4} \tag{4.28}$$

which is proportional to the sum of the distances to the line of perfect match. Among two combinations, one keeps the one with the smallest χ^2_{comb}, i.e., the combination which provides the best charge match between the clusters on the opposite sides.

4.3.8 Telescope Alignment

In order to benefit from the high intrinsic spatial resolution of the detectors, one has to know the exact location of the sensors of the telescope. The approximate position of the sensors is known to the precision of ≈ 1 mm from the design of the detector holders, and the small corrections that determine the actual position can be measured by studying particle track fit residuals. The algorithm of aligning the detectors by particle tracks described in [28] was used here. In this method the individual detectors are aligned using the straight particle tracks defined by the external reference. The outer two sensors play a role of the external reference in our case, and the alignment of the inner two sensors is performed with respect to the outer two.

Let's define the local (sensor) coordinate system (u, v, w) such that the u-axis is going along the precise coordinate (parallel to the long sensor edge), v-axis along the coarse coordinate (along the short edge) and w-axis normal to the sensor plane. The origin of the local coordinate system coincides with the geometrical center of the sensor. The global coordinates are denoted as (x, y, z). The transformation of the hit coordinates from the global to the local system goes as:

$$\mathbf{q} = \mathbf{R} \cdot (\mathbf{r} - \mathbf{r_0}) \tag{4.29}$$

where $\mathbf{r} = (x, y, z),\ \mathbf{q} = (u, v, w),\ \mathbf{R}$ is the rotation matrix and $\mathbf{r_0} = (x_0, y_0, z_0)$ is the position of the detector center in global coordinates. The actual position of the detector center $\mathbf{r_0}$ and the actual sensor orientation $\mathbf{R}$ differ from their design values $\mathbf{r_{0D}}$ and $\mathbf{R_D}$ by a small displacement $\Delta\mathbf{r}$ and orientation correction $\Delta\mathbf{R}$:

$$\mathbf{R} = \Delta\mathbf{R}\mathbf{R_D} \tag{4.30}$$

$$\mathbf{r_0} = \mathbf{r_{0D}} + \Delta\mathbf{r} \tag{4.31}$$

The correction matrix $\Delta\mathbf{R}$ is expressed as:

$$\Delta\mathbf{R} = \mathbf{R}_\gamma \mathbf{R}_\beta \mathbf{R}_\alpha \tag{4.32}$$

where $\mathbf{R}_\alpha$,$\mathbf{R}_\beta$ and $\mathbf{R}_\gamma$ are the small rotations by $\Delta\alpha,\ \Delta\beta,\ \Delta\gamma$ around the u-axis, the (new) v-axis and the (new) w-axis, respectively. The position correction $\Delta\mathbf{r}$ transforms to the local system as:

$$\Delta\mathbf{q} = \Delta\mathbf{R}\mathbf{R_D}\Delta\mathbf{r} \tag{4.33}$$

with $\Delta\mathbf{q} = (\Delta u, \Delta v, \Delta w)$. Using (4.29-4.33) one finds the corrected transformation from global to local system as:

$$\mathbf{q}^{corr} = \Delta\mathbf{R}\mathbf{R_D}(\mathbf{r} - \mathbf{r}_0) - \Delta\mathbf{q}. \tag{4.34}$$

The alignment procedure has to determine the corrective rotation $\Delta\mathbf{R}$ and translation $\Delta\mathbf{r}$ or $\Delta\mathbf{q}$ by minimizing the respective χ^2 using a large number of tracks.

Let's denote the measured hit point in local coordinates as $\mathbf{q}_m = (u_m, v_m, 0)$. The corresponding trajectory impact point for this module is $\mathbf{q}_x^{corr} = (u_x, v_x, 0)$, where the trajectory is defined by the external reference (the two outer modules). The residual is represented as a 2-vector:

$$\varepsilon = \begin{pmatrix} \varepsilon_u \\ \varepsilon_v \end{pmatrix} = \begin{pmatrix} u_x - u_m \\ v_x - v_m \end{pmatrix} \tag{4.35}$$

The χ^2 function that should be minimized for a given module is given by:

$$\chi^2 = \sum_j \varepsilon_j^T \mathbf{V}_j^{-1} \varepsilon_j \tag{4.36}$$

where the summation is done over all the tracks j. The 2×2 matrix $\mathbf{V}_j$ is a covariance matrix of the measurements (u_m, v_m) associated with the track j. The χ^2 function given by (4.36) depends on the alignment parameters $\Delta\mathbf{R}$ and $\Delta\mathbf{r}$ or $\Delta\mathbf{q}$ via u_x and v_x. We have to find such a set of the alignment parameters that minimize this χ^2. One can see from the eq.(4.34-4.36) that the dependence of χ^2 on $\Delta\mathbf{q}$ is already linear, and for small correction angles the matrix $\Delta\mathbf{R}$ can be linearized as:

$$\Delta\mathbf{R} = \begin{pmatrix} 1 & \Delta\gamma & \Delta\beta \\ -\Delta\gamma & 1 & \Delta\alpha \\ -\Delta\beta & -\Delta\alpha & 1 \end{pmatrix} \tag{4.37}$$

If we denote the alignment parameters as $\mathbf{p} = (\Delta u, \Delta v, \Delta w, \Delta\alpha, \Delta\beta, \Delta\gamma)$ then using the linear dependence of χ^2 on $\mathbf{p}$ we can find the vector $\mathbf{p}_{min}$ that minimizes χ^2 using the general χ^2 solution:

$$\mathbf{p}_{min} = \left[\sum_j \mathbf{J}_j^T \mathbf{V}_j^{-1} \mathbf{J}_j \right]^{-1} \left[\sum_j \mathbf{J}_j^T \mathbf{V}_j^{-1} \varepsilon_j \right] \tag{4.38}$$

where $\mathbf{J}_j$ is a Jacobian matrix of $\varepsilon_j(\mathbf{p})$:

$$\mathbf{J}_j = \nabla_{\mathbf{p}} \varepsilon_j(\mathbf{p}). \tag{4.39}$$

In the general case of two measurements (u_m, v_m) and six alignment parameters, the Jacobian $\mathbf{J}_j$ is a 2×6 matrix. We will however limit ourselves only to 3 alignment parameters per sensor: the lateral displacements Δu and Δv in the sensor plane and the rotation $\Delta\gamma$ around the axis w normal to the sensor plane and parallel to the beam axis Z. In the geometry of our experiment with the beam of a small angular divergence falling practically normally to the sensor planes, the sensitivity to the misalignment in the beam direction and to the small tilts around u- and v-axes is very small, yielding a tolerance on these parameters worse than the hardware tolerance given by the sensor holders. In

Table 4.4: Alignment parameters determined for the inner modules 2 and 3.

Module	Δu, (μm)	Δv, (μm)	$\Delta\gamma$,(mrad)
2	-50.70 ± 0.18	1276 ± 9	2.54 ± 0.21
3	267.05 ± 0.17	-61.6 ± 7.7	-2.99 ± 0.19

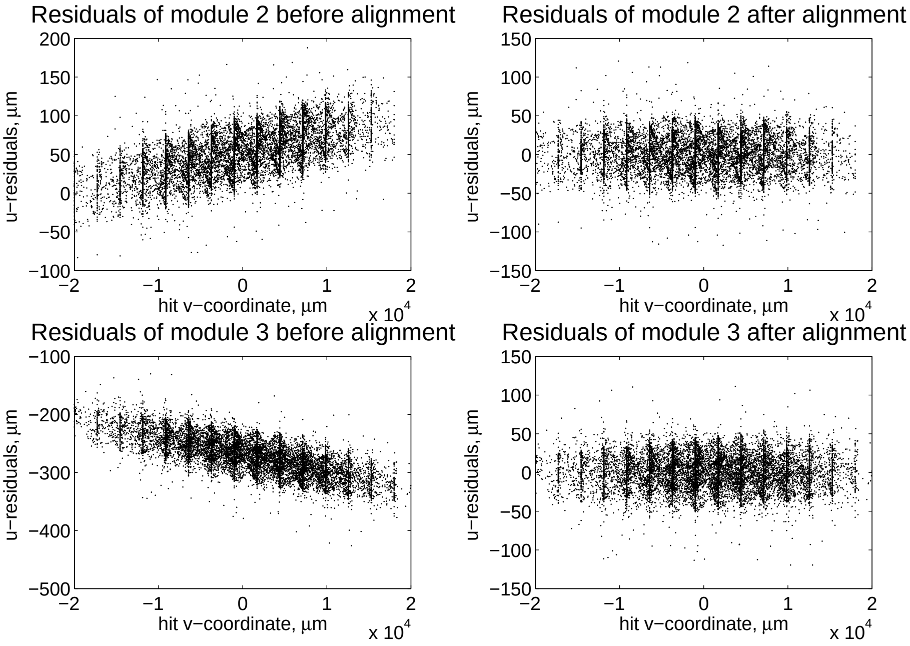

Figure 4.23: u-residuals of modules 2 and 3 plotted versus the v-coordinates before and after the alignment.

other words, the misalignment in those directions has a little effect on the residual distributions. Therefore the vector $\mathbf{p}$ was limited to $\mathbf{p} = (\Delta u, \Delta v, \Delta\gamma)$ and the elements of the 2×3 matrix $\mathbf{J}$ for a given track are:

$$\mathbf{J}^T = \begin{pmatrix} -1 & 0 \\ 0 & -1 \\ v_x & -u_x \end{pmatrix} \tag{4.40}$$

The alignment parameters for the inner two modules were estimated according to the eq.(4.35-4.40) using 14000 tracks. The obtained parameters are listed in the table 4.4, the achieved precision on the lateral sensor displacements Δu and Δv was two orders of magnitude better than the sensor intrinsic resolution (see the next section for the details of the resolution determination).

The effect of the proper module alignment is illustrated in the figure 4.23. Before the alignment parameters were found, the u-residuals were centered not around zero and were also dependent of the v-coordinate of the hit. This lead to an offset and broadening of the distribution of u-residuals. After alignment the dependence on v-coordinate vanishes, the residuals are centered around zero, as expected from the detectors where the residuals originate purely from the measurement errors.

4.3.9 Spatial Resolution

The sensor intrinsic position resolution can be estimated by fitting a track to the reconstructed hits and investigating the residuals. There exist several methods of how to obtain it from the distributions of the residuals [29]. In the first method, a straight track is fitted to the reference sensors and then extrapolated to the studied sensor. Since the studied sensor is not included in the fit, the dispersion of the fit residuals σ_r^2 is just a sum of the squared sensor intrinsic spatial resolution σ_{intr}^2 and squared track fit error σ_f^2, hence:

$$\sigma_{intr}^2 = \sigma_r^2 - \sigma_f^2 \tag{4.41}$$

In the other method the studied sensor is included in the fit, and then one has to include the correlation term which leads to:

$$\sigma_{intr}^2 = \sigma_r^2 + \sigma_f^2 \tag{4.42}$$

In both cases one needs to know the fit error σ_f which is defined by the geometrical arrangement of the modules along the beam axis and by the intrinsic resolutions of the modules σ_{intr} – the values we are looking for and which are not known beforehand. One has to make an initial assumption on the resolutions and then solve the problem iteratively.

We will make an attempt to use another method here. Let's consider a least squares straight line fit to all four modules and try to establish a connection between the observed dispersion of the fit residuals and the sensor measurement errors. The weights of all the points of the fit are kept equal to avoid the recursiveness of the problem. We follow the matrix formalism of the least squares method described for example in [30]. Let's denote $\mathbf{z} = (z_1, \ldots, z_n)^T$ as the coordinates of the n sensor planes along the beam axis Z; $\mathbf{x_m} = (x_{\mathbf{m},1}, \ldots, x_{\mathbf{m},n})^T$ and $\mathbf{y_m} = (y_{\mathbf{m},1}, \ldots, y_{\mathbf{m},n})^T$ as the hit coordinates measured by the sensors in the particular event and projected on the plane XZ and YZ (see Fig.4.1on page 60). Both projections are treated independently, so it is sufficient to describe the method for one of the projections, for example on XZ plane. The measurement errors $\boldsymbol{\epsilon} = (\epsilon_1, \ldots, \epsilon_n)^T$ are defined as the difference between the measured hit coordinates $\mathbf{x_m}$ and the particle track impact points $\mathbf{x_t}$:

$$\mathbf{x_m} = \mathbf{x_t} + \boldsymbol{\epsilon} \tag{4.43}$$

Considering the particle track as a straight line we can rewrite eq. (4.43) in the following form:

$$\mathbf{x_m} = \mathbf{Z} \cdot \boldsymbol{\beta} + \boldsymbol{\epsilon}, \tag{4.44}$$

where $\mathbf{Z}$ is a design matrix and $\boldsymbol{\beta}$ is a vector of coefficients :

$$\mathbf{Z} = \begin{bmatrix} 1 & z_1 \\ 1 & z_2 \\ \vdots & \vdots \\ 1 & z_n \end{bmatrix}; \qquad \boldsymbol{\beta} = \begin{bmatrix} \beta_0 \\ \beta_1 \end{bmatrix}$$

Values β_0 and β_1 are the track intercept and slope respectively. The effect of multiple scattering in the sensor material makes the real particle trajectory slightly kinked, so that the parameters β_0 and β_1 serve only as a straight track approximation to the real particle trajectory. With this approximation the effect of multiple scattering will contribute to the measurement errors. The scattering angle distribution has a gaussian core which contain 98% of all the events, and long non-gaussian tails extending far outside several standard deviations. For pions with momentum of 7 GeV/c and a spacing between the sensors of 3 cm the r.m.s. deviation of the particle track in the next sensor plane due to multiple scattering in the previous sensor plane is about 2.5 μm, which is a small number compared to the expected resolution of ≈ 18 μm in the x-direction if the numbers are added in quadrature, and totally negligible compared with the resolution of 800 μm in the y-direction. However, the non-gaussian tails of the distribution can not be neglected in our case. Events with large scattering angle were excluded from the analysis, as will be explained later in this section.

The fitted track impact points $\mathbf{x_f} = (x_{\mathbf{f},1}, \ldots, x_{\mathbf{f},n})^T$ are determined as:

$$\mathbf{x_f} = \mathbf{H} \cdot \mathbf{x_m} \tag{4.45}$$

where

$$\mathbf{H} = \mathbf{Z}(\mathbf{Z}^T\mathbf{Z})^{-1}\mathbf{Z}^T. \tag{4.46}$$

The fit residuals $\mathbf{r} = \mathbf{x_m} - \mathbf{x_f}$ are given by:

$$\mathbf{r} = (\mathbf{I} - \mathbf{H}) \cdot \mathbf{x_m}. \tag{4.47}$$

where $\mathbf{I}$ is an $n \times n$ unitary matrix. Plugging eq.(4.44) into eq.(4.47) and noting that

$$(\mathbf{I} - \mathbf{H}) \cdot \mathbf{Z} = 0 \tag{4.48}$$

one obtains the relationship between the fit residuals and the measurement errors:

$$\mathbf{r} = (\mathbf{I} - \mathbf{H}) \cdot \boldsymbol{\epsilon}. \tag{4.49}$$

The matrix $(\mathbf{I} - \mathbf{H})$ depends only on the position of the modules along Z axis and does not depend on the data. The rank of this matrix is $n - 2$ since there are only $n-2$ independent residuals. Assuming that there is no correlation between the measurement errors:

$$\mathrm{cov}(\epsilon_i, \epsilon_j) = 0,\ i \neq j, \tag{4.50}$$

one can make a step from $\boldsymbol{r}$ and $\boldsymbol{\epsilon}$ to their r.m.s values and obtain the linear relationship between the dispersions of the fit residuals $\langle r_i^2\rangle$ and the squared sensor intrinsic resolutions $\sigma_{intr}^2 \equiv \langle \epsilon_i^2\rangle$:

$$\langle \mathbf{r}^2\rangle = \mathbf{B}\cdot\langle \boldsymbol{\epsilon}^2\rangle, \tag{4.51}$$

where matrix $\mathbf{B}$ is obtained by squaring the elements of $(\mathbf{I}-\mathbf{H})$:

$$B_{ij} = (\delta_{ij} - H_{ij})^2. \tag{4.52}$$

The matrix $\mathbf{B}$ also depends only on the position of the modules along Z axis. If the matrix $\mathbf{B}$ is nonsingular, then the system of linear equations (4.51) can be solved, and one obtains, without any iterations, the vector of squared intrinsic resolutions $\langle \boldsymbol{\epsilon}^2\rangle$ using the inverse of the matrix $\mathbf{B}$:

$$\langle \boldsymbol{\epsilon}^2\rangle = \mathbf{B}^{-1}\langle \mathbf{r}^2\rangle. \tag{4.53}$$

It is easy to show[3] that the matrix $\mathbf{B}$ is nonsingular only if $n \geqslant 5$, which means that $n = 5$ is the *minimal* number of sensors in the telescope, with which the resolution of each of them can be unambiguously determined using eq. (4.53).

In our case $n = 4$ and rank($\mathbf{B}$) = 3, therefore $\mathbf{B}^{-1}$ does not exist and there is no unique solution to the equation (4.51) which becomes underdetermined. Instead, if the vector $\langle \mathbf{r}^2\rangle$ belongs to the rangespace of the matrix $\mathbf{B}$, which is the case when the eq. (4.50) holds, there exists a family of solutions each of which satisfies the equation (4.51). The family of solutions can be described as:

$$\langle \boldsymbol{\epsilon}^2\rangle = \langle \boldsymbol{\epsilon_0}^2\rangle + \alpha\cdot\mathbf{V_0} \tag{4.54}$$

where $\langle \boldsymbol{\epsilon_0}^2\rangle$ is the particular solution, $\mathbf{V_0}$ – the null-space of the matrix $\mathbf{B}$ (the eigenvector that corresponds to the zero eigenvalue) and α is a free parameter. If no other information is available on the sensor resolutions or their ratios, then there is no preference in choosing a particular parameter α[4]. But if, as is often the case, all the sensors in the telescope are similar, then a reasonable choice would be to pick a solution which gives the closest values for all the sensors. In the general case, to find such a solution one has to find a point on a line in a 4-D space represented by the equation (4.54), which is the closest to the skew line given by the equation:

$$\mathbf{s} = \mathbf{n}\cdot\tau,\ \text{ where the vector } \mathbf{n} = (1,1,1,1),\ \text{ and } \tau \text{ is a free parameter.} \tag{4.55}$$

In case of a symmetric arrangement of the modules around the middle plane of the telescope (like in our setup), this is equivalent to minimizing the norm of the vector $\langle \boldsymbol{\epsilon}^2\rangle$. This solution can be obtained by multiplying the vector $\langle \mathbf{r}^2\rangle$ by a matrix $\mathbf{B}^I$ pseudoinverse to $\mathbf{B}$:

$$\langle \boldsymbol{\epsilon}^2\rangle_{min} = \mathbf{B}^I\cdot\langle \mathbf{r}^2\rangle. \tag{4.56}$$

---

[3] Using the fact that the rank of the matrix $\mathbf{I}-\mathbf{H}$ is $n-2$

[4] Of course, α can only be chosen such that the squared resolutions $\langle \boldsymbol{\epsilon}^2\rangle$ remain positive.

The vector $\langle \boldsymbol{\epsilon}^2 \rangle_{min}$ also belongs to the family of solutions given by the eq. (4.54) but has the smallest norm $\|\langle \boldsymbol{\epsilon}^2 \rangle\|$.

The introduction of multiple scattering creates certain correlations between the measurement errors in different sensors and as a result eq. (4.51) holds only approximately. For $n \geqslant 5$ the solution of this equation always exists, but for $n = 4$ it can be solved only in the least-squares sense, which means finding a solution $\langle \boldsymbol{\epsilon}^2 \rangle$ that minimizes the norm $\|\mathbf{B} \cdot \langle \boldsymbol{\epsilon}^2 \rangle - \langle \mathbf{r}^2 \rangle\|$, or in other words, best explains the observed dispersions of fit residuals. Such a solution is again given by the eq. (4.56) and it was used in the current data analysis.

For the spatial resolution measurements we kept the events with only one hit in each sensor. The unweighted least squares fit with straight tracks to the four hit points was done independently for x and y coordinates. The unweighted fit minimizes the sum of squared residuals for each track:

$$s_x^2 = \sum_{i=1}^{4} (x_{\mathbf{m},i} - x_{\mathbf{f},i})^2 \tag{4.57}$$

$$s_y^2 = \sum_{i=1}^{4} (y_{\mathbf{m},i} - y_{\mathbf{f},i})^2 \tag{4.58}$$

The variances of the fit residual distributions, which are used for the calculation of the spatial resolutions, are sensitive to the shape of the tails of the distributions. If a particle gets scattered by a significant angle in one of the two inner sensors (the scattering in the outer two plays no role because the directions of the incoming and outgoing particles are not measured), then the straight line fit to a real kinked track would result in large residuals in all four sensors, hence in larger values of s_x and s_y. A cut on s_x and s_y may thus effectively remove these events from the analysis and suppress the influence of the multiple scattering by large angles on the final results. The distribution of s_x is shown on figure 4.24. The effect of different s_x^{cut} on the spatial resolution calculated according to eq. (4.56) is demonstrated on figure 4.25. The cut values s_x^{cut} and s_y^{cut} are chosen such that they remove the non-gaussian tails of the residual distributions (especially prominent for x-residuals where the spatial resolution is high) but practically do not affect the core (see the pulls distribution in Fig. 4.27). The chosen value s_x^{cut} discards $\approx 2.5\%$ of the events.

The spatial resolution results are shown on the Fig.4.26 for center-of-gravity hit reconstruction method. In order to compare the above described method with the more commonly used iterative method, the results of the latter are also shown on the same plot. One can see that for the position resolution along the coarse coordinate y, both methods produce practically identical results, although the matrix inversion method does it in one step. The results for the fine coordinate x are also rather close albeit not identical because of the measurement error correlations caused by multiple scattering. In the absence of multiple scattering both methods would give the same answer. Both methods result in an average spatial resolution of ≈ 17 μm in x-direction and ≈ 800 μm in y-direction. The errorbars shown on the picture represent the statistical errors,

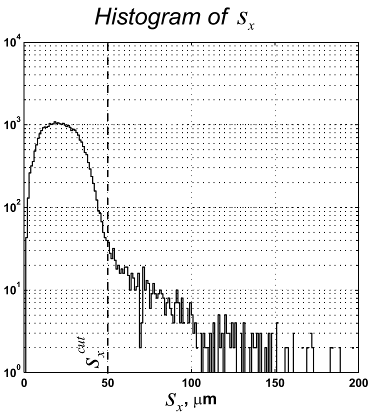

Figure 4.24: The distribution of s_x. The cut on s_x rejects the tracks with large kinks due to multiple scattering. With s_x^{cut}=50μm, 2.5 % of events are rejected.

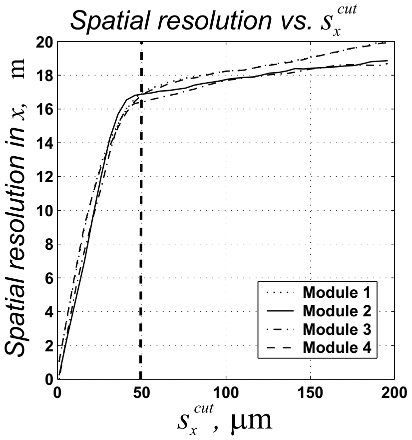

Figure 4.25: The effect of s_x^{cut} on the spatial resolution measurement.

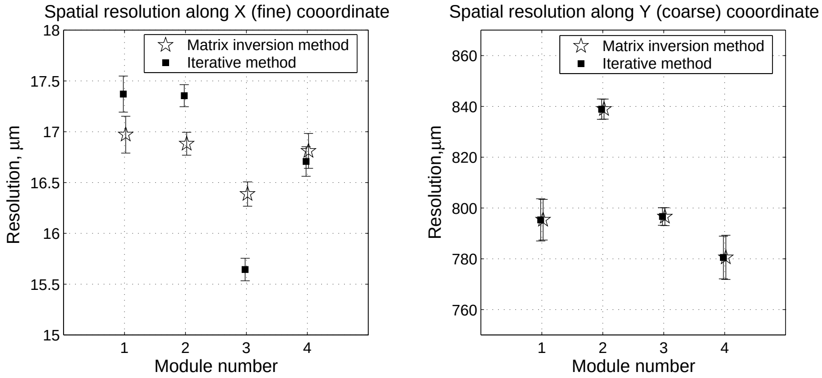

Figure 4.26: The sensor intrinsic position resolution. The results from both the iterative method and the matrix inversion methods are shown.

the systematical uncertainty is estimated to be of the order ≈ 1 μm for x-coordinate and ≈ 30 μm for y-coordinate due to the uncertainty of s_x^{cut} and s_y^{cut} values and the neglected correlation in the measurement errors.

The fit pull distributions can be used to cross-check the correctness of the obtained result. For a particular module the pull functions $p_{\mathbf{x}}$ and $p_{\mathbf{y}}$ are determined as the weighted fit residuals normalized to their standard deviations

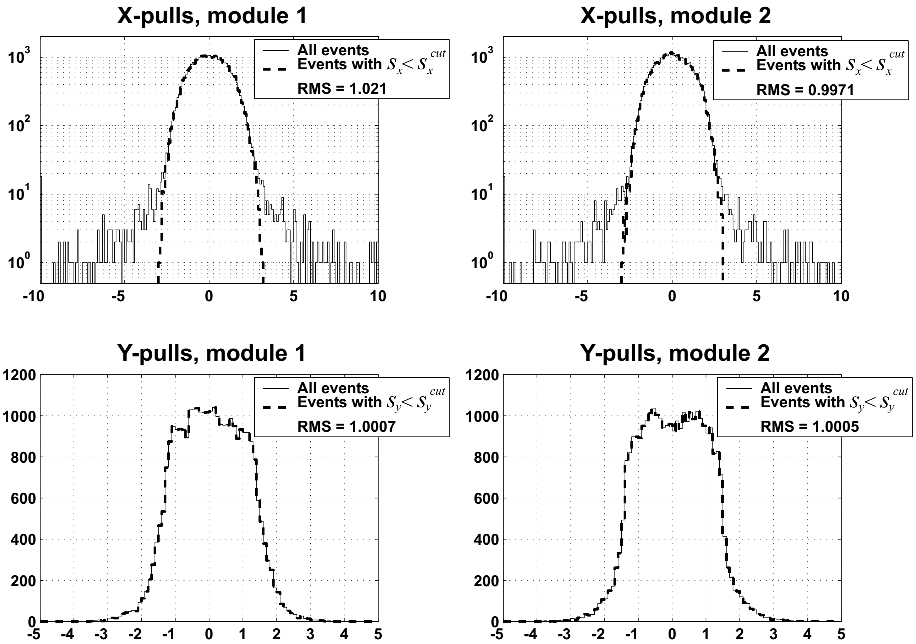

Figure 4.27: p_x and p_y pulls for the first two modules.

estimated from the sensors spatial resolutions:

$$p_{\mathbf{x}} = \frac{x_{\mathbf{m}} - x_{\mathbf{f}}}{\sqrt{\sigma_{intr}^2 - \sigma_f^2}} \tag{4.59}$$

The fit errors σ_f are obtained from least squares fit formalism using error propagation of the errors on slope and intercept. The figure 4.27 demonstrates the fit pull distributions for the modules 1 and 2 obtained using the fit weights equal to the inverse of the sensor spatial resolutions. The standard deviations are close to unity, as expected from the equation (4.59).

4.3.10 Efficiency

The module efficiency is defined as a chance of detecting a charged particle if it passes through the sensor sensitive area. Let's denote the i-th module as a "test module" and all others as "reference modules". The efficiency ε_i of the module i in the telescope can be measured as a ratio of the number of events where all four modules detected a hit over a number of events where either only the reference modules or all four modules detected a hit:

$$\varepsilon_i \simeq \frac{N_{all}}{N_{ref} + N_{all}} \tag{4.60}$$

Table 4.5: Module efficiency

Module	P-side efficiency, %	N-side efficiency, %	Total efficiency ε, %
1	99.76 ± 0.03	99.17 ± 0.05	98.97 ± 0.09
2	99.81 ± 0.02	99.34 ± 0.05	98.34 ± 0.07
3	99.16 ± 0.05	99.61 ± 0.04	98.84 ± 0.09
4	99.71 ± 0.03	99.89 ± 0.02	99.57 ± 0.06

or in other words $1 - \varepsilon_i$ is a chance that the i-th module misses a particle hit. In order to determine ε_i, the tracks of the single-track events found using only the three reference modules were inter- or extrapolated to the test module. In order to make sure that the particle track really passed through the test sensor sensitive area, we kept only those events where the projected impact point lied at least 5 mm away from the sensor edge in y-direction and 200 μm in x-direction. The region around the projected impact point was searched for the hits and the hit was accepted if it was found closer than 300 μm in x-direction and 7500 μm in y-direction from the extrapolated impact point. These cut values were selected after studying the distribution of the residuals and were chosen such to include also the events were the particle was deflected off the trajectory due to multiple scattering or δ-ray production. The chance of finding a noise cluster inside this region is negligible since the probability of having a noise cluster per sensor side is less than 1%. The results of the efficiency calculation with statistical errors are shown in the table 4.5. On average, only about 1% of the particles were not detected.

It's illustrative to plot the expected location of the missing hits in the test module using the tracks reconstructed from the reference modules. It was found that the missing hits are not randomly scattered across the sensor area but are concentrated along the noisy or dead strips of the module (see Fig. 4.28). The disconnected strips seem not to cause a particle loss as long as these strips are not clustered together. The particle loss is thus a direct consequence of the module production defects. The efficiency of the module areas with nominal strip noise and absence of bonding defects is consistent with 100%.

4.4 Conclusion

In this chapter I have presented results from the tests, with 7 GeV/c pion beam, of four double-sided silicon strip detectors of the ALICE SSD design.

It was demonstrated that the module design provides an excellent signal to noise ratios in the range 40-75. The higher noise level found on the n-side of Canberra sensors results in a lower signal to noise ratio but does not have an impact on the detection efficiency. The higher noise level is a result of a large interstrip capacitance [31], which was reduced for the sensors of the serial production.

The good performance of the sensors and the front-end electronics results

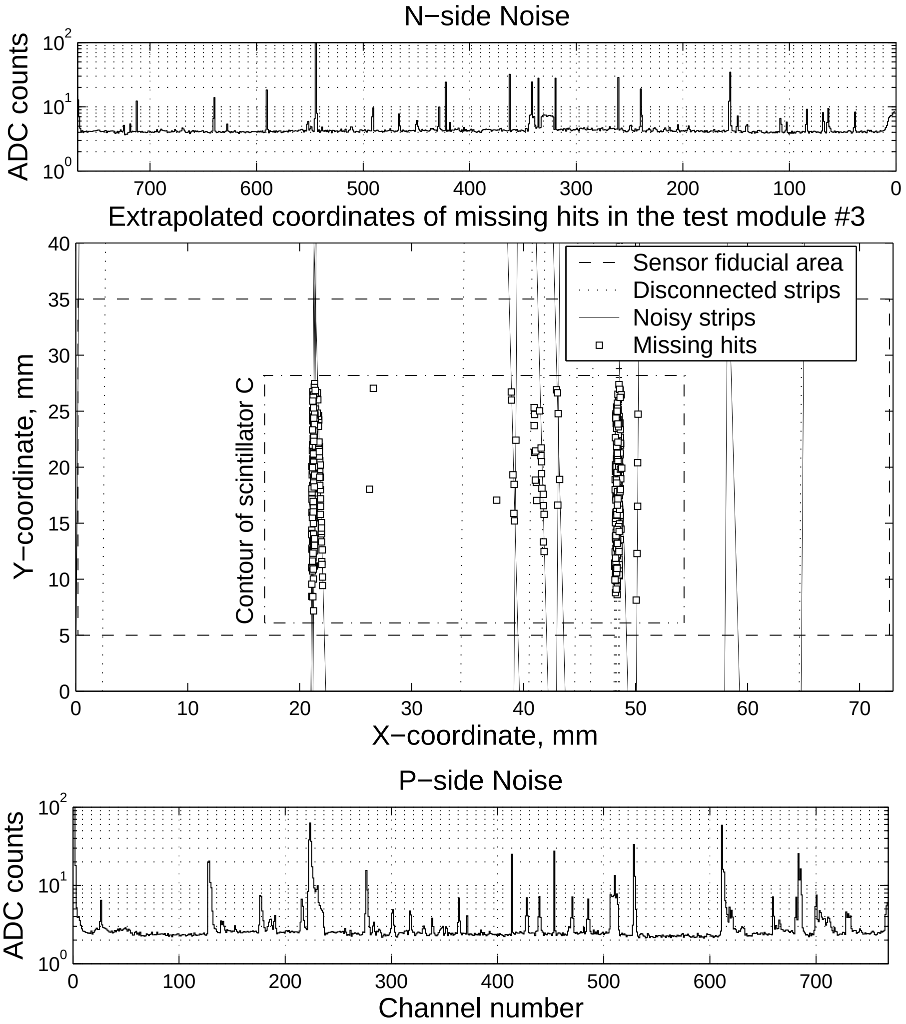

Figure 4.28: Location of the missing hits on the module 3. The trigger scintillator C selects only the middle part of the sensor. The missing hits are located along the noisy strips or disconnected strips clustered together.

in a high detection efficiency for minimum ionizing particles, typically 99.5% per sensor side or 98.9% for both in coincidence. It was demonstrated that the particle loss is a result of the production defects. Since these modules were the first modules of the final design, when not all the assembly operations were very well under control, they naturally have a worse quality than the modules produced during the mass-production stage. We therefore expect that the mass-production modules that end up in the SSD layers of the ITS will show a better efficiency due to a smaller number of defects and a severe quality control of all the components and the complete modules.

A fast method for determination of the spatial resolution was developed. It was shown that a measurement with four unknown detectors, without a reference telescope, can still be analyzed assuming that the four detectors have similar spatial resolution. The four ALICE SSD modules were shown to provide a resolution of 17 μm in the x-direction and 800 μm in the y-direction. Since the clustering algorithm used here exploits the information provided by the charge sharing between neighboring strips, these resolutions are better than the digital resolution expected for the 95 μm strip pitch, which would already be sufficient for the ALICE experiment.

Summary

The ALICE experiment at CERN will study heavy ion collisions at a center-of-mass energy 5.5 TeV per nucleon pair. Particle tracking at radii $r < 45$ cm is done by the Inner Tracking System (ITS), which consist of six cylindrical layers of silicon detectors. The outer two layers of the ITS use double-sided silicon strip detectors. This thesis focuses on testing of these detectors and performance studies of the detector module prototypes at the beam test.

Silicon strip detector layers will require about 20 thousand HAL25 front-end readout chips and about 3.5 thousand hybrids each containing 6 HAL25 chips. During the assembly procedure, chips are bonded on a patterned TAB aluminium microcables which connect to all the chip input and output pads, and then the chips are assembled on the hybrids. Bonding failures at the chip or hybrid level may either render the component non-functional or deteriorate its the performance such that it can not be used for the module production. After each bonding operation, the component testing is done to reject the non-functional or poorly performing chips and hybrids. The LabVIEW-controlled test station for this operation has been built at Utrecht University and was successfully used for mass production acceptance tests of chips and hybrids at three production labs. The functionality of the chip registers, bonding quality and analogue functionality of the chips and hybrids are addressed in the test. The test routines were optimized to minimize the testing time to make sure that testing is not a bottleneck of the mass production.

For testing of complete modules the laser scanning station with 1060 nm diode laser has been assembled at Utrecht University. The testing method relies of the fact that a response of the detector module to a short collimated laser beam pulse resembles a response to a minimum ionizing particle. A small beam spot size ($\sim$7 μm) allows to deposit the charge in a narrow region and measure the response of individual detector channels. First several module prototypes have been studied with this setup, the strip gain and charge sharing function have been measured, the later is compared with the model predictions. It was also shown that for a laser beam of a high monochromaticity, interference in the sensor bulk significantly modulates the deposited charge and introduces a systematic error of the gain measurement. Signatures of disconnected strips and pin-holes defects have been observed, the response of the disconnected strips to the laser beam has been correlated with the noise measurements.

Beam test of four prototype modules have been carried out at PS accelerator

at CERN using 7 GeV/c pions. It was demonstrated that the modules provide an excellent signal-to-noise ratio, in the range 40-75. The estimated spatial resolution for the normally incident tracks is about 17 μm using the center-of-gravity cluster reconstruction method. A non-iterative method for spatial resolution determination was developed, it was shown that in order to determine the resolution of each individual detector in the telescope, the telescope should consist of at least 5 detectors.

The detectors showed a high detection efficiency, in the range 98.3%-99.6%. It was shown that particle loss occurs mostly in the defected regions near the noisy strips or strips with a very low gain. The efficiency of the sensor area with nominal characteristics is consistent with 100%.

Samenvatting

Het ALICE experiment bij CERN gaat botsingen tussen zware ionen bestuderen bij een zwaartepunts-energie van 5.5 TeV per kerndeeltje. De reconstructie van deeltjes-sporen binnen een straal van 45 cm, wordt uitgevoerd door het Inner Tracking System (ITS), bestaande uit zes cylindrische lagen van silicium detectoren. De buitenste twee lagen van het ITS gebruiken hiervoor dubbelzijdige silicium strip detectoren. Dit proefschrift richt zich met name op het testen van deze detectoren enerzijds en de studie van de prestatie van prototype detector-modules in een testbundel anderzijds.

De verschillende lagen met silicium strips hebben ongeveer 21000 zogenaamde HAL25 front-end readout chips nodig om uitgelezen te worden en ongeveer 3600 hybrides waarop de HAL25 chips bevestigd worden. Gedurende de assemblage worden alle contactpunten van de chips door middel van een wrijflas (TAB) aan een patroon van aluminium microkabels verbonden. Vervolgens word de chip op een zogenaamde hybride gemonteerd. In iedere stap van deze procedure kunnen verbindingsfouten er toe leiden dat het onderdeel ongeschikt wordt voor verwerking in een module. Daarom wordt na iedere handeling het specifieke onderdeel getest en uitgesloten van verder gebruik wanneer de prestatie ervan niet afdoende blijkt. Hiervoor is een, met LabVIEW software gestuurde, proef-opstelling aan de Universiteit Utrecht ontwikkeld die vervolgens met succes gebruikt is voor de massa productie van chips en hybrides bij alle drie de produktie laboratoria. De proef bestond onder andere uit het testen van de chip registers, de kwaliteit van de diverse verbindingen en de analoge parameters van zowel chips als hybrides. De procedure werd geoptimalizeerd om te voorkomen dat het testen een struikelblok zou vormen bij de massa produktie.

Voor het testen van volledige modules, is bij de Universiteit Utrecht een proef-opstelling met een 1060 nm diode laser gebouwd. De gebruikte methode berust erop dat een zeer korte, gecollimeerde puls van de laser bundel een soortgelijke-reactie van de detector teweeg brengt als een minimaal ionizerend deeltje (MIP). Het kleine oppervlak van de laser bundel bij het focale punt ($\sim 7\ \mu$m) maakt het mogelijk om de lading in een klein volume te deponeren en hierdoor de respons te meten van de individuele detector segmenten. Aanvankelijk zijn een aantal prototype modules bestudeerd met deze opstelling, de gain van de strips en de functie die de verdeling van de lading tussen de strips beschrijft, zijn beide gemeten en de verdelingsfunctie is vergeleken met de voorspellingen van een model. Vervolgens werd aangetoond dat, voor een laser bundel van zeer hoge monochromaticiteit, er interferentie in de bulk van de sensor ontstaat die de gedeponeerde lading zodanig moduleert dat een significante systematische fout onstaat bij de bepaling van de gain. Aanwijzingen voor losse strips en 'pinhole' effecten zijn waargenomen en de bundel-respons van deze niet-verbonden strips konden gecorreleerd worden met metingen van elektronische ruis.

De bundeltest van vier prototype modules is uitgevoerd met behulp van de PS versneller bij CERN, gebruik makend van 7 GeV/c pionen. Daar werd aangetoond dat de verhouding tussen signaal en ruis voor deze modules zeer goed is, namelijk binnen het interval 40-75. Het ruimtelijk oplossend vermogen voor loodrecht invallende sporen is ongeveer 17 μm wanneer de zwaartepunts methode voor cluster reconstructie werd gebruikt. Een niet-iteratieve techniek voor ruimtelijk oplossend vermogen was ontwikkeld. Het is aangetoond dat de telescoop uit tenminste 5 detectoren moet bestaan, teneinde het oplossend vermogen te kunnen bepalen van iedere individuele detector in de telescoop. De detector vertoonde een hoge detectie efficiëntie, in de orde van 98.3%-99.6%. Wanneer een deeltjes-spoor niet gereconstrueerd kon worden, dan was dat meestal in gebieden waar de strips onderhevig waren aan ruis dan wel een zeer lage gain hebben. De efficientie van het detector oppervlak onder nominale condities is consistent met 100%.

Acknowledgement

First of all my sincerest thanks go to my supervisor Gert-Jan Nooren for his careful guidance and support during my studies, for the shared experience and for the numerous enlightening discussions on various topics, related to physics and not. It was a pleasure to work with a person with such an inexhaustible optimism like yours, and to whom I could speak "the same language". Furthermore, I'm deeply thankful to my promotor René Kamermans for creating a comfortable working environment and for systematically yet delicately directing me towards the successful completion of my thesis. Your paternalistic attitude helped me to hold up in the stressful writing phase. I would also like to thank to Paul Kuijer for many valuable comments and advises I received from him. I'm also thankful to Kees Oskamp, Arie de Haas and Ton van den Brink. I could always count on your helping hand in building and troubleshooting the setups I was working with. Martijn, thank you for helping me with Dutch. My cordial thanks to Gennady Zinovjev, without your efforts I would not have started with this project.

In the early days of my stay in the Netherlands, when the new environment and the language barrier cut most of my social links, it was my greatest luck to meet Valeria and Bailoz. You became my best friends and I will never forget your hospitality, warm company, help and support in difficult situations. Theo, Nadya, Masha end Sergei, this is also relevant to you. I will really miss you all.

For the great parties and fun we had together I'm really grateful to Julia, Lilyana, Yi-Lo, Roman, Roberto, and Eugene, the latter one also deserves separate thanks for his cooking tips.

I'd like to thank Rene Barthel for helping me to discover kitesurfing, through the prism of which the windy Netherlands looked in a totally different light. My very special thanks to Wojtek and Niels for showing me excellent mtb-tracks all around the country. Biking with you was really bringing me back to life and helped me to endure this four years' PhD marathon.

Bibliography

[1] ALICE Physics Performance Report Vol I, CERN/LHCC 2005-030

[2] ALICE Technical Proposal, CERN/LHCC 95-71 LHCC/P3 1995

[3] T.J.Brodbeck *et.al.*, "Simulation of charge collection and sharing in microstrip detectors", Nucl.Instr. and Meth. **A**395 (1997) 29-34

[4] J.Kemmer, G.Lutz et al., "New structures for position sensitive semiconductor detectors", Nucl. Instr. and Meth. **A**273 (1988) 588-598

[5] C.Hu-Guo *et al.*, "The HAL25 Front-End Chip for ALICE Silicon Strip Detectors", proceedings of 7th Workshop on Electronics for LHC Experiments, Stockholm, Sweden, September 2001.

[6] A.P.deHaas *et al.*, "Aluminium Microcable Technology for ALICE Silicon Strip Detector: A Status Report", proceedings of 8th Workshop on Electronics for LHC Experiment, Colmar, France, October 2002 2003-049 (2003)

[7] R.Kluit *et al.*, "Realisation of ladder EndCap electronics for the ALICE ITS SSD. Proceedings of 10th workshop on electronics for LHC and future experiments. Boston, USA, September 2004.

[8] "ALICE Inner Tracking System Technical Design Report", CERN/LHCC 99-12.

[9] IC51-3244-1333 Clamshell socket by
Yamaichi Electronics, for specifications see:
http://www.yamaichi.de/tb/quad_flat_pack/pdf/ic51-tab.pdf

[10] H.Bleeker, P. van den Eijnden, F. de Jong, "Boundary Scan Test – A Practical Approach". Kluwer Academic Publishers, 1993.

[11] www.measurementcomputing.com

[12] S.Shaheen *et al.*, "Characterization and quality control of silicon microstrip detectors with an infrared diode laser system". Nucl. Instr. Meth. **A 352** (1995) 573-578.

[13] S.Sze, “Physics of semiconductor devices”, 1981

[14] W.Wagner *et al.*, “Characterization of Silicon Microstrip Detectors Using an Infrared Laser System”, Nucl. Instr. Meth. **A 423**(1999) 303-319.

[15] E.Belau *et.al* “Charge Collection in Silicon Strip Detectors”, Nucl. Instr. Meth. **214**(1983) 253-260.

[16] Particle Data Group, “Particle Detectors”, Phys. Rev. **D54**, 145 (1996).

[17] G.Lutz. “Semiconductor Radiation Detectors. Device Physics”. Springer 1999.

[18] N.van der Kolk, “Calibration of silicon strip detector module test setup”, student report UU(SAP)03-1.

[19] M.Born, E.Wolf, “Principles of Optics”, Pergamon press 1959.

[20] G.Lutz, “Correlated noise in silicon strip detector readout” Nucl. Inst. Meth. **A**309 (1991) 545.

[21] CERN/LHCC 95-71, ALICE Technical Proposal

[22] W.R.Leo, ”Techniques for Nuclear and Particle Physics Experiments”, Springer-Verlag, 1987.

[23] L.Landau, “On the energy loss of fast particles by ionization”. J. Physics USSR Vol. VIII, 4 (1944)

[24] J.F.Bak et.al.,“Large Departures from Landau Distributions for High-Energy Particle Travesing Thin Si and Ge Tragets”, Nuclear Physics B288 (1987) 681-716.

[25] S.Hancock et.al., “Energy-loss Distributions for Single Particles and Several Particle in Thin Silicon Absorber”, Nucl. Instr. & Meth., B1 (1984) 16-22

[26] S.Hancock et.al., “Energy loss and energy straggling of protons and pions in the momentum range 0.7 to 115 GeV/c”, Phys. Rev., A28, 1983.

[27] R.Turchetta, “Spatial resolution of silicon microstrip detectors”, Nucl. Instr. & Meth., **A** 335(1993)44-58.

[28] V.Karimäki, A.Heikkinen, T.Lampén, T.Lindén, “Sensor Alignment by Tracks”, *CHEP03*, La Jolla California; arXiv:physics/0306034.

[29] V.Karimäki et al., Nucl. Instr. and Meth. **A**453 (2000) 536.

[30] Draper, N.R and H. Smith, Applied Regression Analysis, 3rd Ed., John Wiley & Sons, New York, 1998.

[31] I.Rachevskaia et al., Nucl Instr and Meth. **A**530 (2004) 59.